UNIVERSITÀ DEGLI STUDI DI BOLOGNA

FACOLTÀ DI INGEGNERIA

Corso di Dottorato in
ING-IND/13: MECCANICA APPLICATA ALLE MACCHINE
Ciclo XX

Fault detection in rotating machines by vibration signal processing techniques

Tesi di dottorato di:
Gianluca D'Elia

Coordinatore:
Chiar.mo Prof. Vincenzo Parenti Castelli

Tutore:
Chiar.mo Prof. Giorgio Dalpiaz

Anno Accademico 2007-2008

Contents

List of Figures

List of Tables

Nomenclature

$a_n(t)$	Amplitude modulation function
$b_n(t)$	Phase modulation function
f_m	Gear meshing frequency [Hz]
f_r	Gear frequency rotation [Hz]
$\mathcal{F}\{\}$	Fourier Transform
$\mathcal{F}^{-1}\{\}$	Inverse Fourier Transform
$g(t)$	Time window
$n_s(t)$	Random noise of a signal
s	Scale parameter
$x_d(t)$	Deterministic part of a signal
z	Number of gear teeth
$x(t)$	Signal
$x_{nd}(t)$	Non-deterministic part of a signal
τ	Time lag
$\psi_s(t)$	Mother Wavelet

Chapter 1

Introduction

Science is not belief, but the will to find out

Anonymous

1.1 Background

Machines with moving parts give rise to vibrations and consequently noise. The setting up and the status of each machine yield to a peculiar vibration signature. Therefore, a change in the vibration signature, due to a change in the machine state, can be used to detect incipient defects before they become critical. This is the goal of condition monitoring, in which the informations obtained from a machine signature are used in order to detect faults at an early stage. In general the basic condition monitoring process is subdivided in to three main steps: firstly a relevant physical quantity is measured, then the collected data are processed and machine state features are extracted, finally the extracted state features are compared to reference values. Moreover, beyond detection, condition monitoring methods can also be used in order to diagnose the type and the evolution of certain defects.

As a matter of fact signals acquired from machines often contain contributions from several different components as well as noise. Therefore, the major challenge of condition monitoring is to point out the signal content that is related to the state of the monitored component.

The study on incipient failure detection of gearboxes started over two decades ago, whilst other rotating machine applications, i.e. IC engines are more recent, because

of the complexity of the involved process.

There are a large number of signal processing techniques that can be used in order to extract interesting information from a measured vibration signal. In the following the basics of these techniques are outlined.

1.1.1 Time domain

Simple statistical parameters evaluated over the measured time domain signal, can give some interesting information about potential defects. For example the peak and root mean square values are referred to the overall vibration level. This statistical parameters are simple to implement, however they are rather insensitive tools for defect detection. A useful technique in many defect detection is the synchronous signal averaging technique (SSAT) [1], the result of the SSAT is the signal average, which is the ensemble average of the angle domain signal, synchronously sampled with respect to the rotation of one particular shaft. In the resulting averaged signal (SA), the random noise as well as non-synchronous components are attenuated. The main advantage of the SSAT is the possibility to extract from a complex gearbox vibration signal, a more simple signal related to the gear of interest. However this technique has a pivotal drawback that is related to the complexity of the measurement equipment. As a matter of fact an additional sensor are required in order to measure the rotational shaft speed.

In addition, the SA can be bandpass filtered at the dominant meshing harmonic, and the application of the Hilbert transform provides both amplitude and phase modulation functions [2]. This technique is called the narrow-band demodulation technique.

1.1.2 Frequency domain

Potential defects can be analyzed by the frequency domain spectrum of the vibration signal. In order to calculate the frequency spectrum of a sampled time signal, the Fast Fourier Transform algorithm can be used as a numerically efficient method [3]. It is important to notice that all digital Fourier transform methods assume stationary

signals, peridic in the time window.

1.1.3 Time-frequency domain

As previously mentioned spectral methods such as Fourier transform assume stationary signals. However, localized defects generally introduce non-stationary signal components [4], which cannot be properly described by ordinary spectral methods. This drawback can be overcome by the use of the short-time Fourier transform (STFT) that is a Fourier transform applied to many short time windows. However, narrow time windows mean poor frequency resolution. This trade-off between time and frequency resolution is the main disadvantage of the STFT, which can be solved by the use of other time-frequecy techniques such as Wigner-Ville distribution (WVD) and Continuous wavelt transform (CWT). The WVD provides better time-frequency resolutions compared to the STFT, but produces severe interference terms.

1.1.4 Cyclostationary approach

It is well known that many conventional statistical signal processing methods treat random signals as if they were statistically stationary. Nevertheless, in some cases even multiple periodicities are involved. This typically requires that the random signal is modeled as cyclostationary, i.e. the statistical parameters vary in time with single or multiple periodicities. It can be shown that most rotating machine signals can be treated as cyclostationary [5–10].

1.2 Research objectives

This study seeks to detect rotating machine defects using a range of techniques including synchronous time averaging, Hilbert transform-based demodulation, continuous wavelet transform, Wigner-Ville distribution and spectral correlation density function.

The detection and the diagnostic capability of these techniques are discussed and compared on the basis of experimental results concerning gear tooth faults, i.e. fa-

tigue crack at the tooth root and tooth spalls of different sizes, as well as assembly faults in diesel engine. Moreover, the sensitivity to fault severity is assessed by the application of these signal processing techniques to gear tooth faults of different sizes.

1.3 Overview of the thesis

Chapter 2 introduces the essential signal processing theoretical background. First of all it highlights two time-frequency techniques, i.e. Continuous Wavelet Transform (CWT) and Wigner-Ville Distribution (WVD), which overcome the well known problem of fixed time-frequency resolution in the Short Time Fourier Tranform. Moreover the cross-term trouble of the WVD is explained, showing a new technique based on the Fourier-Bessel series expansion proposed by Pachori and Sircar [11], which allows cross-term cut off. Finally, the property of cyclostationary signals are described and both probabilistic and non-probabilistic approaches are explained.

Chapter 3 concerns the diagnosis of IC engine assembly faults. Two types of faults are considered, inverted piston and rod only pre-loaded. Firstly ,the experimental apparatus concerning the vibration tests is explained, highlighting the pro and contra of the could test compared to the genuine hot test. After that the vibration signal model for these type of faults is introduced. Finally the acceleration signals acquired from the engine block during a cold test cycle at the end of the assembly line are analyzed, as suggested by Antoni in [6].

Chapter 4 seeks the analysis and diagnosis of gear faults. Two different types of faults are take into account. The first one is a fatigue crack at the tooth root and the other one are tooth spalls of different sizes. The vibration signal model of these type of faults are analyzed explaining the differences between the two mathematical model. The above-mentioned techniques, i.e. continuous wavelet transform, Wigner-Ville distribution as well as techniques based on a cyclostationary signal model are applied to the vibration signal data in order to study the effectiveness and diagnostic capabilities of each signal processing technique.

Chapter 2

Non-stationary signal processing

Mathematical Analysis is as extensive as nature herself

Joseph Fourier

This chapter concerns on an essential signal processing theoretical background. De facto this is an expected step in order to understand all the considerations about the experimental results in the following chapters.

There are a large number of signal processing techniques that can be used to extract interesting information concerning defects from a measured vibration signal. Therefore, the major challenge of condition monitoring is to find the most suitable for each specific task. As a matter of fact, the type of signal to be analyzed has an influence on the type of analysis to be carried out, and also on the choice of analysis parameters. That is why it is a pivotal step to examine the various types of signal that are encountered in practice.

Rigorously, random signals are described mathematically by using the theory of probability, random variables, and stochastic processes, which are not the aim of this work, but a complete stochastic signal analysis can be found in [12].

Figure 2.1 depicts the classical division into different signal types, which actually is the division into stationary and non-stationary signals. For practical purposes it is sufficient to interpret stationary functions as being those whose average properties do not vary with time and are thus independent of the particular sample record used to determine them. While the term “non-stationary” cover all signals which do not

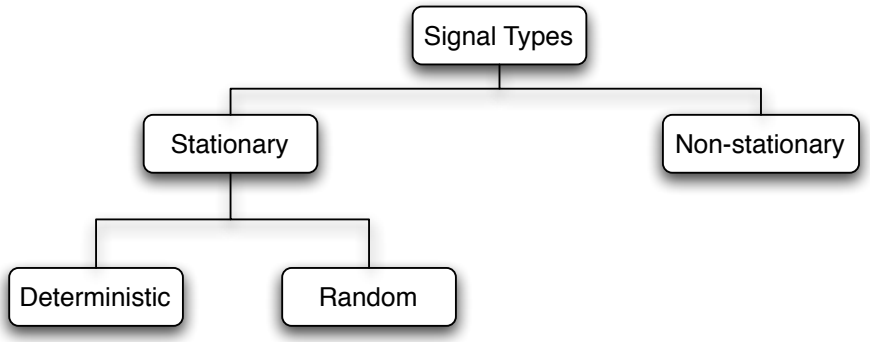

Figure 2.1: Signal schematic classification

satisfy the requirements for stationary ones.

Several signal processing techniques are applied to stationary signals in both time and frequency domain for diagnostic purpose of rotating machines, such as time-synchronous average (TSA), power spectral density (PSD) amplitude and phase demodulations and cepstrum analysis.

However, a more recent trend has been toward representation in the time–frequency analysis, such as wavelet transform and Wigner-Ville Distribution. Moreover an emerging interest has been reported on modeling rotating machine signals as cyclostationary, which embodies a particular class of non-stationary stochastic processes. Therefore, in this work attention is focused on time-frequency techniques and on the cyclostationary approach. Subsequently, the main theoretical background on time-frequency analysis is reported in section 2.1, highlighting the two time-frequency techniques, i.e. Continuous Wavelet Transform (CWT) and Wigner-Ville Distribution (WVD), which overcome the well known problem of fixed time-frequency resolution of the Short Time Fourier Tranform. Moreover the cross-term trouble of the WVD is explained in section 2.1.2, showing a new technique based on the Fourier-Bessel series expansion proposed by Pachori and Sircar [11], which allows cross-term cut off. Finally, the property of cyclostationary signals are described in section 2.2, in which both probabilistic and non-probabilistic approaches are explained.

2.1 Non-stationary signal analysis

The aim of this section is the description of the theoretical background concerning the continuos wavelet transform (CWT) and Wigner-Ville Distribution (WVD). These techniques play a pivotal role in the analysis of non-stationarry signals, because they provide an alternative to the classical Short-Time Fourier Transform. A detailed theories on wavelet transform and Wigner-Ville distribution can be found in [4, 13–18].

2.1.1 From Short-Time Fourier Transform to Continuos Wavelet Transform

Time–frequency analysis offers an alternative method to signal analysis by presenting information simultaneously in the time domain and in the frequency one.

For stationary signals, the genuine approach is the well-known Fourier transform:

$$X(f) = \int_{-\infty}^{+\infty} x(t) e^{-2j\pi ft} dt \tag{2.1}$$

As long as we are satisfied with linear time-invariant operators, the Fourier transform provides simple answers to most questions. Its richness makes it suitable for a wide range of applications such as signal transmissions or stationary signal processing. However, if we are interested in transient phenomena the Fourier transform becomes a cumbersome tool. De facto, as one can see from equation (2.1), the Fourier coefficients $X(f)$ are obtained by inner products of $x(t)$ with sinusoidal waves $e^{2j\pi ft}$ with infinite duration in time. Therefore, the global information makes it difficult to analyze any local property of $x(t)$, because any abrupt change in the time signal is spread out over the entire frequency axis. As a consequence, the Fourier Transform cannot be adapted to non-stationary signals.

In order to overcame this difficulty, a “local frequency” parameter is introduced in the Fourier Transform, so that the “local” Fourier Transform looks at the signal through a window over which the signal is approximately stationary.

The Fourier Transfrom was first adapted by Gabor [19] to define a two-dimensional time-frequency representation. Let $x(t)$ a signal which is stationary when looked through a limited extent window $g(t)$, which is centered at a certain time location τ, then the Sort-Time Fourier Transform is defined as follows:

$$STFT(\tau, f) = \int_{-\infty}^{+\infty} x(t) g^*(t-\tau) e^{-j2\pi ft} dt \tag{2.2}$$

where $*$ denotes the complex conjugate.

Even if many properties of the Fourier Transform carry over to the STFT, the signal analysis strongly depends on the choice of the window $g(t)$. In other words, the STFT may be seen as modulated filter bank. De facto, for a given frequency f, the STFT filters the signal at each time instant with a bandpass filter having as impulse response the window function modulated to that frequency [14]. From this dual interpretation of the STFT, some considerations about time and frequency transform resolutions can be granted. De facto, both time and frequency resolutions are linked to the energy of the window $g(t)$, therefore their product is lower bounded by the uncertainty principle, or Heisenberg inequality, which states that:

$$\Delta t \Delta f \geq \frac{1}{4\pi} \tag{2.3}$$

So, relolution in time and frequency cannot be arbitrarily small and once a window has been chosen, the time-frequency resolution is fixed over the entire time-frequency plane, since the same window is used at all frequencies, Figure 2.2 (a).

In order to overcame the resolution limitation of the STFT, one can think at a filter back in which the time resolution increases with the central frequency of the analysis filter [14]. Therefore, the frequency resolution (Δf) is imposed to be proportional to f:

$$\frac{\Delta f}{f} = c \tag{2.4}$$

where c is a constant. In other words, the frequency response of the analysis filter

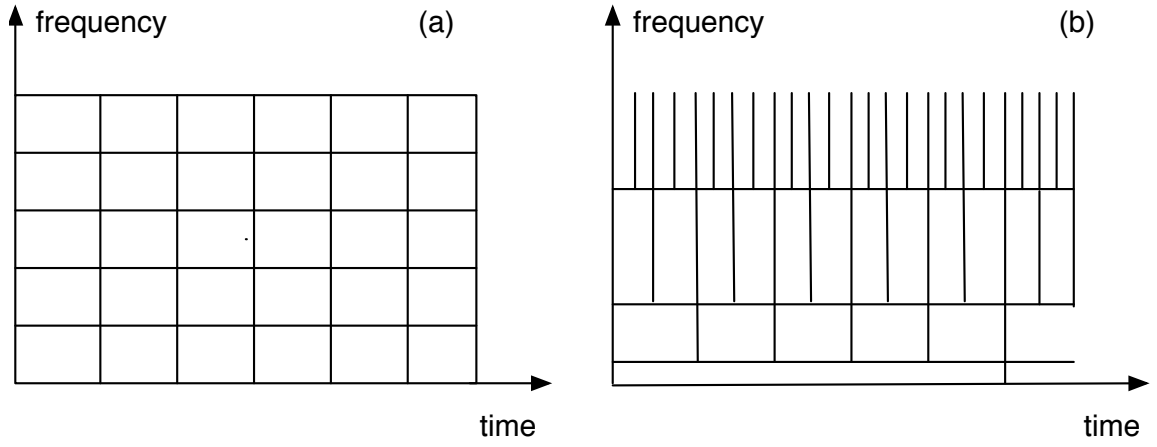

Figure 2.2: Time-frequency resolution of: (a) Short-Time-Fourier-Transform (STFT) and (b) Wavelet Transform (WT)

is regularly spaced in a logarithmic scale. This way, Heisenberg inequality is still satisfied, but the time resolution becomes arbitrarily good at high frequencies, and the frequency resolution becomes arbitrarily good at low frequency as well, Figure 2.2 (*b*).

The above idea of multiresolution analysis is followed by the CWT, therefore the continuous wavelet transform is a signal processing technique which overcomes the resolution limitation of the STFT and is defined as follows [13]:

$$CWT(s,\tau) = \int_{-\infty}^{+\infty} x(t)\psi_s^*\Big(\frac{t-\tau}{s}\Big)dt \tag{2.5}$$

where s and τ are the scale factor and the translation parameter respectively, whilst $\psi_s(t)$ is called the mother wavelet:

$$\psi_s(t) = \frac{1}{\sqrt{s}}\psi\Big(\frac{t}{s}\Big) \tag{2.6}$$

The term $1/\sqrt{s}$ of the right-end side of equation (2.6) is used for energy normalization. Some considerations about the time-frequency resolution of the CWT can be obtained by analyzing the Fourier transform of the mother wavelet $\psi(t)$:

$$\mathcal{F}\left\{\frac{1}{\sqrt{s}}\psi\Big(\frac{t}{s}\Big)\right\} = \Psi(sf) \tag{2.7}$$

Therefore, if $\psi(t)$ has a "bandwidth" Δf with a central frequency f_0, $\psi(st)$ has a "bandwidth" $\Delta f/s$ with a central frequency f_0/s.

Otherwise, by comparing the STFT (equation (2.2)) with the CWT (equation (2.5)) it is important to note that the local frequency defined in (2.2) is linked to the one defined in (2.5). This is the reason why the terminology "scale" is often preferred to "frequency". However, the link between scale and frequency is straightforward, de facto as the scale increases the wavelet becomes spread out in time and so only long-time behavior of the signal is taken into account. On the contrary as the scale decreases the wavelet becomes shrinked in time and only short-time behavior of the signal is taken into account. In other words, large scales mean global views, while very small scales mean detailed views. Figure 2.3 plots a mother wavelet for two different values of the scale parameter s.

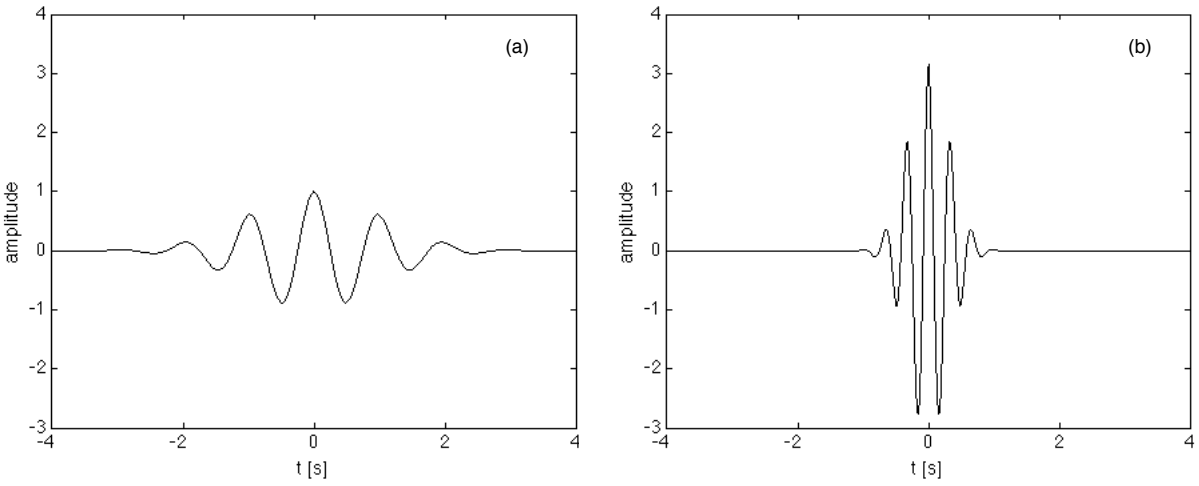

Figure 2.3: Mother Wavelet with (a) large scale and (b) small scale

There are a number of basis functions that can be used as the mother wavelet for Wavelet Transformation [13]. Since the mother wavelet produces all wavelet functions used in the transformation through translation and scaling, it determines the characteristics of the resulting Wavelet Transform. Therefore, the details of the particular application should be taken into account and the appropriate mother wavelet should be chosen in order to use the Wavelet Transform effectively.

In this work two types of mother wavelets are taken into account, Morlet and Im-

pulse mother wavelet. A remarkable feature of the Morlet wavelet is that its Fourier spectrum is Gaussian, whilst the Impulse one is taken into account in this work due to its capability for the analysis of impulse in vibration signals [20].

Morlet and Impulse mother wavelet are defined as follows:

$$\psi(t)_{morlet} = e^{-t^2/2}\cos(2\pi f_0 t) \tag{2.8a}$$

$$\psi(t)_{impulse} = \sqrt{2\pi}e^{2\pi j f_0 t - |2\pi t|} \tag{2.8b}$$

where f_0 is the central frequency of the mother wavelets. In this work f_0 is equal to 0.8125 *Hz* for Morlet mother wavelet and 20 *Hz* for Impulse one.

CWT Numerical implementation

In order to solve the CWT integral of equation (2.5), the formulation proposed by Wang and McFadden [21] is used. Because of the selected wavelets of equations (2.8a) and (2.8b) satisfy the relation $\psi(-t) = \psi^*(t)$, by using the convolution theorem, equation (2.5) can be written as:

$$CWT(s,\tau) = \frac{1}{\sqrt{a}}\mathcal{F}^{-1}\big\{X(f)\Psi^*(f/s)\big\} \tag{2.9}$$

Therefore, the CWT can be evaluated by taking the advantage of the FFT algorithm, and can be straightforwardly implemented in Matlab code.

In the following, an illustrate example is given in order to show the effectiveness of the two different mother wavelets (equations (2.8a) (2.8b)) considered in this work. The simulated signal used in the example is:

$$x(t) = 4e^{-t_{imp}/0.025}\sin(2\pi f_{imp} t_{imp}) + \sum_{i=1}^{2}\sin(2\pi f_i t) + n(t) \tag{2.10}$$

where $n(t)$ indicate a uniformly distributed random noise of mean 1 and:

$$t_{imp} = \begin{cases} t & 0 \le t/t_0 < 1 \\ t - Nt_0 & N \le t/t_0 < N+1 \end{cases}$$

and N is a positive integer.

When t changes from 0 to 1 *s*, $t_0 = 0.125$ *s*, $f_{imp} = 400$ Hz and $f_i = i \times 100$ *Hz*, the time waveform of the signal is shown in Figure 2.4. The continuous wavelet transforms

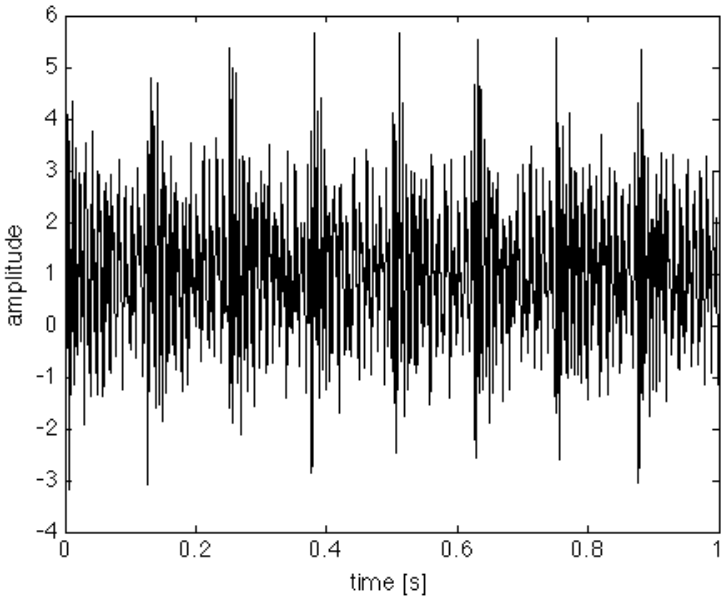

Figure 2.4: Simulated signal: two sinusoidal components and impulse responses

of the simulated signal are plotted in Figure 2.5 (*a*) and (*b*) in the case of Morlet and Impuse mother wavelet respectively. According to equation (2.10), the simulated signal contains three frequency components, i.e. 100 *Hz*, 200 *Hz* and 400 *Hz*. As Figure 2.5 (*a*) shows, only the component at 100 Hz is clearly visible in the CWT map, whilst the component at 200 *Hz* is well localized in time but is spread out in frequency. In particular the impulsive component are not well depicted with Morlet wavelet. On the contrary, the Impulse wavelet (Figure 2.5 (*b*)) is able to detects continuos frequency components as well as transient components. In fact it is possible to notice that, in the case of Impulse mother wavelet, the time-frequency signal features become more explicit in the CWT map.

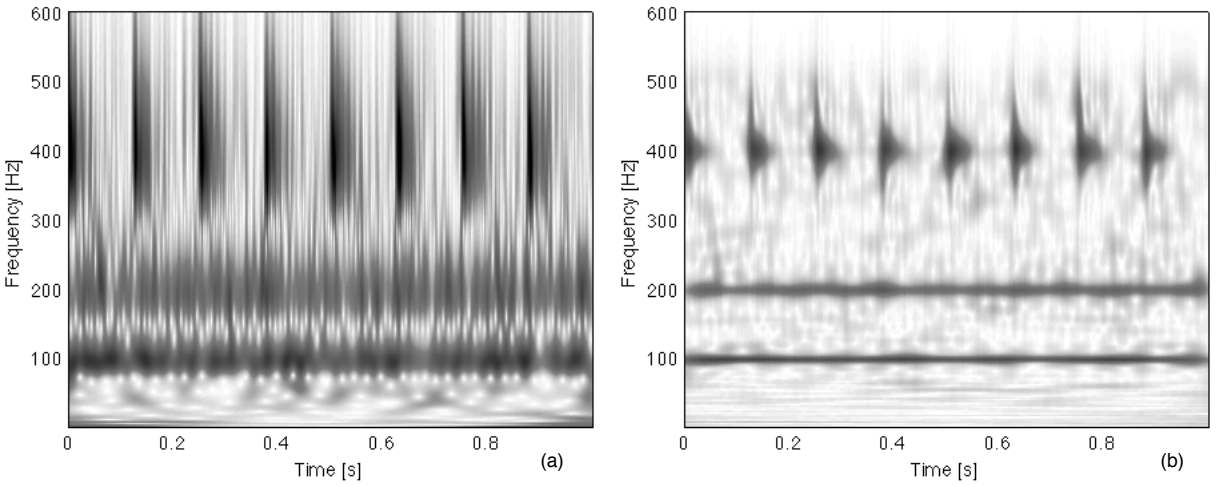

Figure 2.5: CWT of the simulated signal $x(t)$: (a) Morlet and (b) Impulse mother wavelet

2.1.2 Wigner-Ville Distribution

Another time-frequcny characterization of a signal that overcomes the STFT drawback is the Wigner distribution. The genuine formulation was introduced by Wigner in 1932 in the quantum mechanics field. In the 1948 Ville proposed its use in signal analysis when he defined the analytical signal.

Let $x(t)$ be a continuous signal, the Wigner distribution (WD) of the signal $x(t)$ is defined as [15]:

$$W_x(t,\omega) = \int_{-\infty}^{+\infty} x\Big(t+\frac{\tau}{2}\Big)x^*\Big(t-\frac{\tau}{2}\Big)e^{-j\omega\tau}d\tau \tag{2.11}$$

It is important to note that a similar expression exists for the spectra too:

$$W_X(\omega,t) = \frac{1}{2\pi}\int_{-\infty}^{+\infty} X\Big(\omega+\frac{\xi}{2}\Big)X^*\Big(\omega-\frac{\xi}{2}\Big)e^{j\xi t}d\xi \tag{2.12}$$

Therefore, a symmetry between time and frequency definitions exists:

$$W_X(\omega,t) = W_x(t,\omega) \tag{2.13}$$

Equation (2.13) is an important relation, because it means that the Wigner distribution of a spectrum can be determined by the Wigner distribution of the related time signal by switching time and frequency variables.

The WD has a number of useful properties, which have been extensively studied in [15]. Subsequently are reported only the fundamental ones.

Property 1:

For any signal $x(t)$ we have:

$$W_x(t,\omega) = W_x^*(t,\omega) \tag{2.14}$$

and so the WD is a real function.

Property 2:

The spectral density is equal to the projection of the WD on the frequency axis, whilst the instantaneous signal power is equal to the projection on the time axis:

$$\int_{-\infty}^{+\infty} W_x(t,\omega)dt = \quad |X(\omega)|^2 \tag{2.15a}$$

$$\int_{-\infty}^{+\infty} W_x(t,\omega)df = \quad |x(t)|^2 \tag{2.15b}$$

As previously said, Ville suggests the use of the analytic signal in the assessment of the WD. As matter of fact that, real signals have symmetric spectra. Hence only one half of the spectrum contains important signal informations, whilst the other half increases the redundancy of the Wigner distribution. These redundancies can be removed by the use of the analytic signal.

Consider the case where $x(t)$ is an analytic signal, therefore its imaginary part $x_I(t)$

is equal to the Hilbert transform of its real part $x_R(t)$:

$$x_I(t) = \frac{1}{\pi} \int_{-\infty}^{+\infty} \frac{x_R(\tau)}{t-\tau} d\tau \tag{2.16}$$

The Wigner distribution of the analytic signal is termed the Wigner-Ville distribution (WVD).

The WVD is a powerful tool for the time-frequency analysis of vibration signals. Unfortunately, one of the pivotal problem concerning the WVD is its nonlinear behavior, arising from the product of the time-shifted analytical signal with its complex conjugate. These interferences that can make the interpretation of the WVD difficult, can be removed by smoothing procedures or signal decomposition via perfect reconstruction filter bank [22–25].

De facto, the WVD of a signal which is composed by M components is given by:

$$W_x(t,\omega) = \underbrace{\sum_{i=1}^{M} W_{x_i}(t,\omega)}_{auto-components} + \underbrace{\sum_{k=1}^{M-1} \sum_{l=k+1}^{M} 2\Re[W_{x_k x_l}(t,\omega)]}_{cross-components} \tag{2.17}$$

thus, the WVD of a composite signal has M auto-components and a cross term for every pair of auto-components. This is a pivotal drawback of the WVD, in fact the time vibration signal which derive from a mechanical system, such as a gear systems, contains the meshing frequency as well as additional harmonics. Therefore, some "ghost" components at frequencies that are not related to the number of gear teeth can arise, increasing the difficulties in the detections of possible tooth fault.

In the last year Pachori [11] proposed a new technique based on the Fourier-Bessel (FB) expansion. This method combines the FB expansion and the WVD in order to obtain a time-frequency representation without introducing cross terms. This method is advantageous over the technique based on the filter bank approach [24, 25], because it does not need any prior information about the signal frequency-band.

Fourier-Bessel expansion

Let $x(t)$ be a continuous-time signal considered over an arbitrary interval $(0, a)$, the Fourer-Bessel series expansion is given by [26]:

$$x(t) = \sum_{l=1}^{L} C_l J_0\left(\frac{\lambda_l}{a}t\right) \tag{2.18}$$

where $J_0(\cdot)$ are the first kind zero-order Bessel function, which are the solution of the Bessel's differential equation. Where the FB coefficients C_l are computed via the following equation:

$$C_l = \frac{2\int_0^a tx(t)J_0(\frac{\lambda_l}{a}t)dt}{a^2[J_1(\lambda_l)]^2} \tag{2.19}$$

where $J_1(\cdot)$ is the first kind first order Bessel function, λ_l are the ascending positive roots of equation $J_0(t) = 0$ and the integral in the numerator of the right-end side of equation (2.19) is the well-known finite Hankel transform [27]. It is possible to notice that, as opposite to the sinusoidal basis of the Fourier series, the Bessel functions decay within the signal range. Figure 2.6 plots the two Bessel functions of the first kind. The bandwidth of the reconstructed signal can be obtained from the Fourier transform of the Bessel function. As explained by Arfken in [27], the l^{th} term approximate bandwidth of the right-end side of equation (2.18) is $\omega \cong \lambda_l/a$. Thus, if L terms are taken into account in the reconstruction of the signal $x(t)$, a maximum bandwidth of $\omega_{max} \cong \lambda_L/a$ can be obtained.

For multi-component signal, i.e. a signal $x(t)$ that is the sum of M $x_i(t)$ terms, each component can be expansed in FB series via equation (2.18), so a multi-component signal can be written as:

$$x(t) = \sum_{i=1}^{M}\sum_{l=1}^{L} C_{li} J_0\left(\frac{\lambda_l}{a}t\right) \tag{2.20}$$

Thus, by interchanging the summations, the FB series coefficients of a multi-

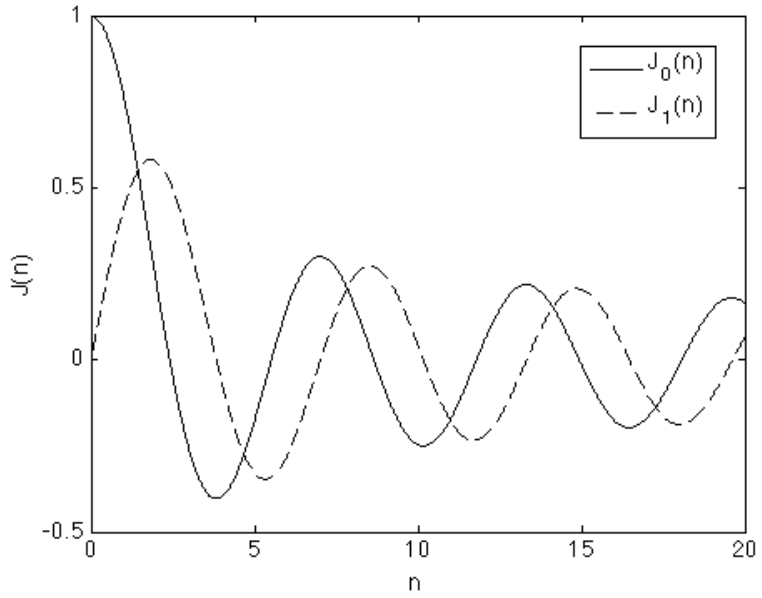

Figure 2.6: Bessel function of the first kind of zero order $J_0(n)$ and first order $J_1(n)$

component signal can be obtained as:

$$C_l = \sum_{i=1}^{M} C_{li} \tag{2.21}$$

If each term of the composite signal is well separated in the frequency domain, then the signal components will be associated with various distinct clusters of nonoverlapping FB coefficients. Therefore each component of the signal can be separately reconstructed by identifying and separating the corresponding FB coefficients.

Figure 2.7 (*b*) plots the FB coefficients for a simple signal, i.e. a signal which is the sum of two sinusoids of frequency 10 and 20 *Hz* (Figure 2.7 (*a*)). It is possible to see from Figure 2.7 (*b*) two abrupt changes in the C_l signature at 20^{th} and 40^{th} coefficient respectively, which represent the two single components of which the signal is composed. Therefore the two signal components (Figure 2.8) can be recovered by choosing a proper C_l coefficient band, which overlaps the desired component and substituting it into equation (2.18). As previously said the FB series expansion can be suitable in order to perform WVD of multi-component signal. The basic parallel description of the procedure is shown in Figure 2.9; it consists of tree time-sequenced stages: sig-

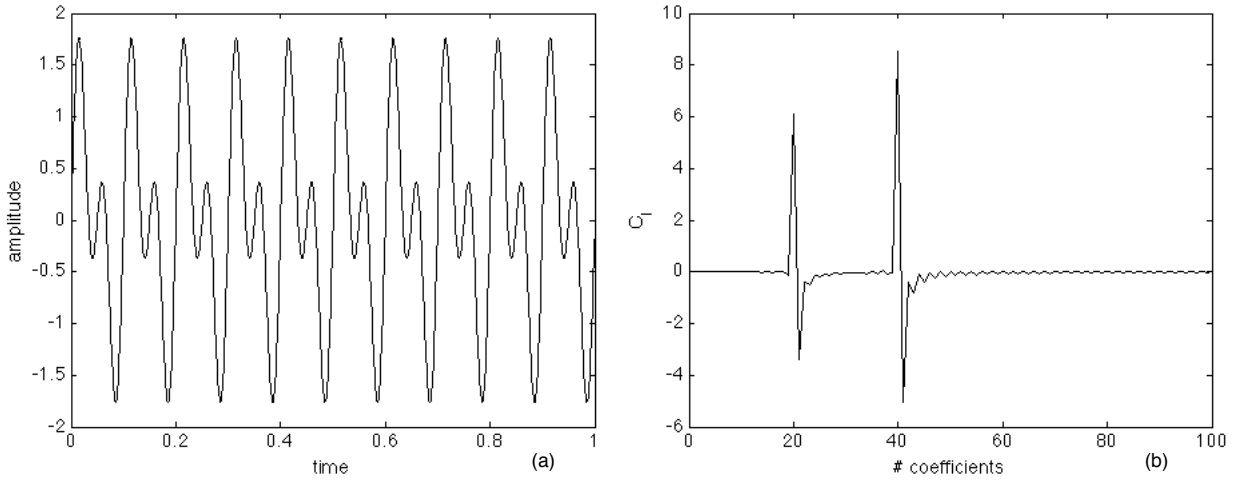

Figure 2.7: Time signal (a) and its FB series coefficients (b)

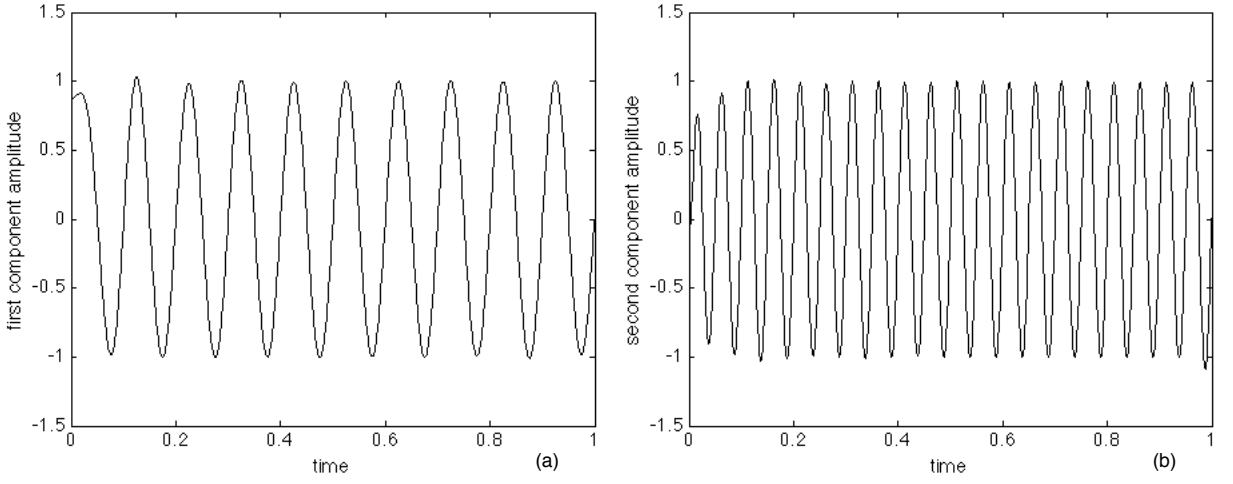

Figure 2.8: Reconstructed signal components: (a) first component at 10 *Hz*, (b) second component at 20 *Hz*

nal component separations via FB series expansion, evaluation of the WVD for each mono-component signal and summation of these distributions in order to obtain the WVD of the composite signal.

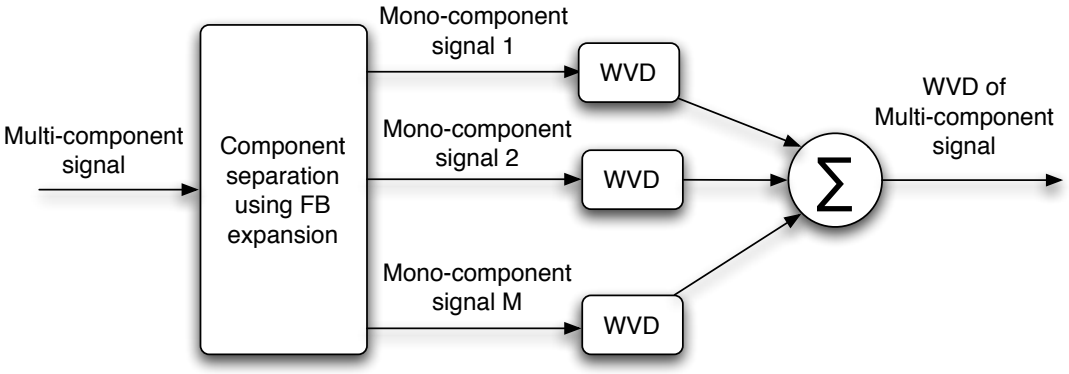

Figure 2.9: Block diagram for the WVD of multicomponent signal via FB expansion

WVD numerical implementation

Let $x(n\Delta t)$ the sampled version of the continuous signal $x(t)$, with sampling interval Δt and observation period $N\Delta t$. The discrete Wigner-Ville distribution of $x(n\Delta t)$ is given by [28]:

$$WVD(n,m) = \frac{1}{2N}\sum_{k=0}^{N-1} x(k\Delta t)x^*((n-k)\Delta t)e^{-j\frac{\pi m(2k-n)}{N}} \tag{2.22}$$

In order to take the advantages of the FFT algorithm, equation (2.22) can be separated into even and odd time samples by replacing n with $2n$ and $2n+1$ respectively. The even time sample series is therefore given by:

$$WVD(2n,m) = \frac{1}{2N}\sum_{k=0}^{N-1} x((n+k)\Delta t)x^*((n-k)\Delta t)e^{-j\frac{2\pi mk}{N}} \tag{2.23}$$

while the odd time samples:

$$WVD(2n+1,m) = \frac{1}{2N}e^{j\frac{\pi m}{N}}\sum_{k=0}^{N-1} x((n+k)\Delta t)x^*((n-k+1)\Delta t)e^{-j\frac{2\pi mk}{N}} \tag{2.24}$$

As an example, the WVD of the simulated signal of equation (2.10) is computed,

and the results are plotted in Figure 2.10 (*a*). As plotted, several cross-terms arise which make the interpretation of the WVD difficult. In fact, only the horizontal lines at 100 and 200 *Hz* belong to the simulated signal. Moreover, it is possible identify the presence of a series of impulses, even if, once again interferences occur and the impulse signal components lie hidden in a cross-terms series. Therefore, in order to remove the interferences due to the non linear behavior of the WV distribution, the simulated signal is decomposed in its main components via FB series expansion. The procedure shown in Figure 2.9 is applied to the simulated signal of equation (2.10) and the results are plotted in Figure 2.10 (*b*). As plotted, interferences are extremely

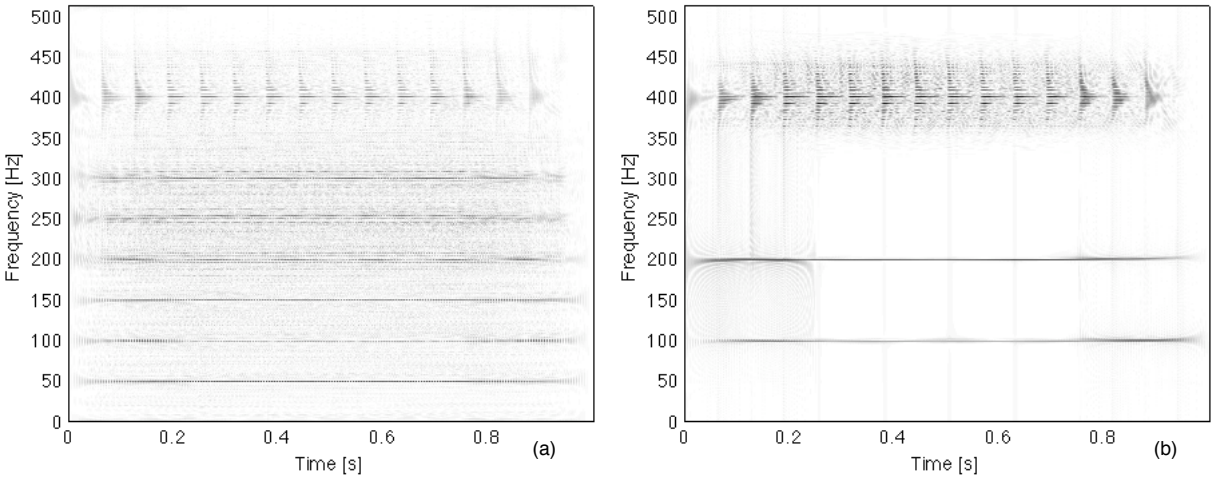

Figure 2.10: (a) WVD of the simulated signal of equation (2.10) and (b) WVD of the reconstructed signal via FB expansion

reduced. The two sinusoidal components are well represented by the two horizontal lines at 100 and 200 *Hz*. Unfortunately, interferences occurring at 400 *Hz*, and the genuine impulse signal components are not detectable. This interferences can not be removed due to the unfeasible choice of a proper C_l coefficient band. De facto, as Figure 2.11 shows, the two sinusoidal terms yield the two components at 200^{th} and 400^{th} coefficient number. Therefore, these terms can be separated form the original signal and recovered back, by using equation (2.18). On the contrary, the impulsive signal components yield to the cluster centered at the 800^{th} coefficient number and composed of several neighboring components. These component cannot be separated

and so, the reconstructed signal contains all the impulsive content of the original signal, as depicted in Figure 2.12.

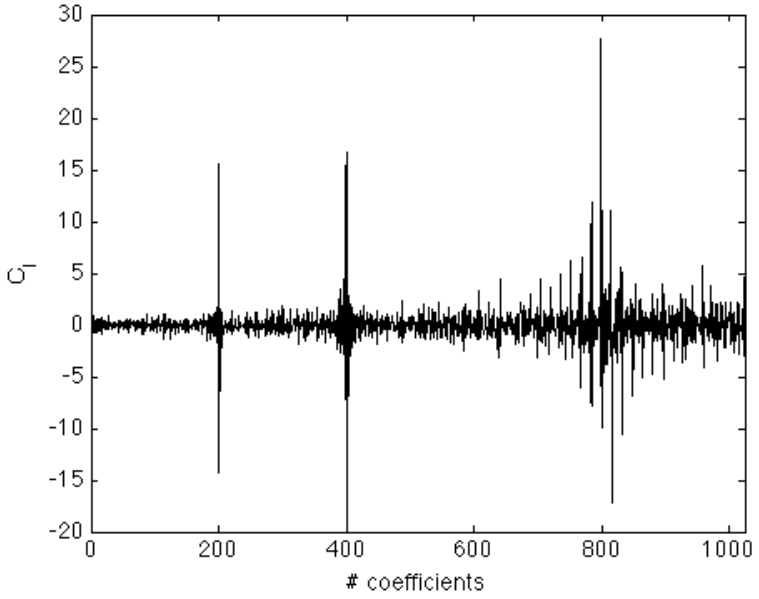

Figure 2.11: Fourier Bessel series coefficient of the simulated signal of equation 2.10

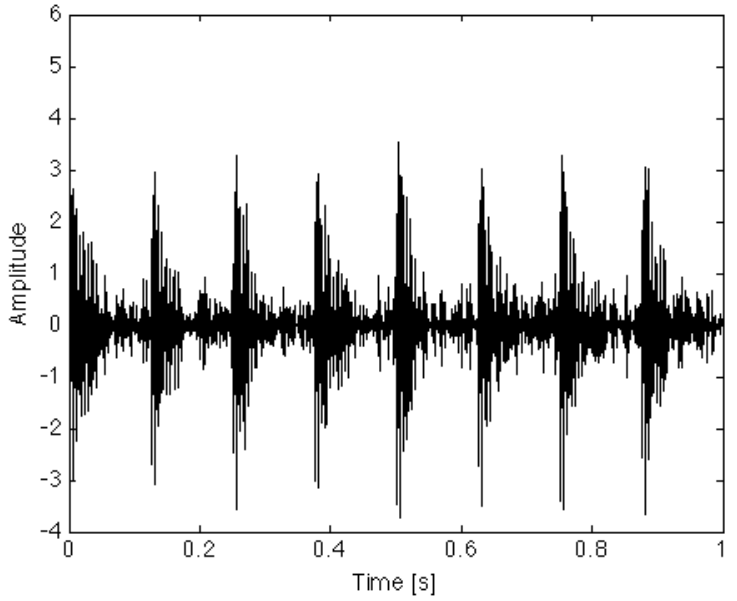

Figure 2.12: Impulsive components reconstructed via FB series expansion of the simulated signal

2.2 Cyclostationarity

This section describes the property of cyclostationarity of signals, in comparison to stationarity, in both time and frequency domain. A detailed theory of cyclostationary process can be found in [29–35].

Cyclostationary process are specific non-stationary process characterised by the periodical variation of the statistical moments. Therefore, in order to understand the property of cyclostationary signals it is first necessary to describe the stationary one.

2.2.1 Stationary process

Manolakis et al. [12] define a random process $x(t)$ to be stationary in a strict sense (SS) if the statistical parameters determined for $x(t)$ do not depend upon the choice of time origin. This definition in general concerns the stationarity property of order N. In this work, only the first and second order stationarity properties of a random series are taken into account, because they are strictly related to the cyclostationarity property of real mechanical signals.

First order stationarity

Mathematically, a random process $x(t)$ is said to be stationary to the first order if:

$$f_x(x(t)) = f_x(x(t+\tau)) \tag{2.25}$$

where $f_x()$ defines the probability density function and t and τ are arbitrary time instants. In other words, equation (2.25) states that the probability density function of the first order random stationary process is invariant in time. Since for random stationary process the shape of the probability density function does not change as a function of time, the expected value is a constant function of time too, and is given by:

$$\mathrm{E}\{x(t)\} = \mu_x \tag{2.26}$$

where $\mathrm{E}\{\}$ denotes the *expected value* or *expectation*. This means an average over an infinite set of occurrences of $x(t)$, where this infinite set is called *ensemble*. Therefore, first order stationarity implies that the mean value is time invariant.

Second order stationarity

A random process $x(t)$ is defined as second order stationary if its autocorrelation function $\mathrm{R}_x(t,\tau)$ satisfies the following relation:

$$\mathrm{R}_x(\tau) = \mathrm{E}\{x(t)x^*(t-\tau)\} \tag{2.27}$$

which states that, the autocorrelation function of the second order stationary random process $x(t)$ is not a function of t, but only of the delay τ.

A wide sense stationary (WSS) process is both first order stationary and second order stationary and therefore it is one in which the mean value and the autocorrelation are invariant in time.

2.2.2 Cyclostationary process

Cyclocstationary process is subsequently described both in a probabilistic and non-probabilistic manner. The probabilistic approach is based on ensemble averages, whilst the non-probabilistic one is based on time averages. Both developments are given because for theoretical work the probabilistic method is easier to manipulate, whilst for experimental signal processing, the time averaging method is more useful.

A probabilistic approach

First order cyclostationary process

A random process $x(t)$ is said to be first order cyclostationary with period T if the following equation is true:

$$f_x(x(t)) = f_x(x(t+nT)) \tag{2.28}$$

where n is an arbitrary integer. Equation (2.28) implies that the expected value of a first order cyclostationary process is a periodic function of time, which is:

$$\mathrm{E}\{x(t)\} = \mathrm{E}\{x(t+nT)\} \tag{2.29}$$

Therefore, a first order cyclostationary random process has a mean value which is periodic with period T as the opposite to the first order stationary process which has a mean value invariant in time.

Second order cyclostationary process

A random process $x(t)$ is said to be second order cyclostationary if:

$$\mathrm{R}_x(t,\tau) = \mathrm{E}\{x(t+nT)x^*(t+nT-\tau)\} = \mathrm{R}_x(t+T,\tau) \tag{2.30}$$

Therefore, for a second order cyclostationary process the autocorrelation function is periodic with period T, which is the period of the stocastic process $x(t)$.

A wide sense cyclostationary (WSCS) process satisfied both equations (2.29) and (2.30). It is important to notice that for a cyclostationary process the autocorrelation function $\mathrm{R}_x(t,\tau)$ is expressed as a function of two variables, τ is the "parametric time", which is the lag between the two signals, and t is the "real time", which is the time origin of the autocorrelation calculation.

It must be pointed out that the expectation plays a pivotal role, in the case of a probabilistic approach of cyclostationary process. In fact, the properties of the autocorrelation based on the probabilistic definition are of course dependent on how the ensemble is defined. An ensemble is a set of an infinite number of instances of the process under consideration, but it is important to be aware of the similarities and differences between these instances. De facto, whether the instances can be taken synchronous or not; this determines if the process is stationary or cyclostaionary. In order to reveal the cyclostationarity of a process the autocorrelation has to be evaluated over synchronized process instances. In any case, it is important to notice that, the synchronization of a signal with no inherent periodicity (such as a white noise)

would not result in a periodic autocorrelation function. The periodicity of the autocorrelation is not a result of the synchronization of the process instances, but it is necessary in order to reveal a particular signal's cyclostationarity.

As the autocorrelation function of equation (2.30) is periodic in t with period T, it can be expanded in Fourier series:

$$\mathrm{R}_x(t,\tau) = \sum_{\alpha} \mathrm{R}_x^{\alpha}(\tau) e^{j2\pi\alpha t} \tag{2.31}$$

where α is called the cyclic frequency and is equal to $1/T$. The summation can be over all values of α, although the coefficient R_x^{α} will be zero unless α is equal to a period of the autocorrelation function. If $\mathrm{R}_x(t,\tau)$ is not periodic, then all coefficient of the summation will be zero except for R_x^0.

The quantities R_x^{α} are called cyclic autocorrelation functions, and are defined as the Fourier coefficient of $\mathrm{R}_x(t,\tau)$, such as:

$$\begin{aligned} \mathrm{R}_x^{\alpha}(\tau) &= \mathrm{E}\{\mathrm{R}_x(t,\tau) e^{-j2\pi\alpha t}\} \\ &= \mathrm{E}\Big\{x\Big(t+\frac{\tau}{2}\Big)x^*\Big(t-\frac{\tau}{2}\Big)e^{-j2\pi\alpha t}\Big\} \end{aligned} \tag{2.32}$$

Notice that $x(t-\tau/2)e^{j2\pi\alpha t}$ is simply the signal $x(t-\tau/2)$ shifted in frequency by α. This means that, for a cyclostationary signal with a cyclic frequency α exists a non-zero correlation between $x(t)$ and a shifted version of $x(t)$ by α. This is know as spectral correlation and is the frequency domain manifestation of cyclostationarity.

A non-probabilistic approach

As previously said the non-probabilistic approach is based on time average. In order to analyze cyclostationary signal Gardner [34] proposes the following definition:

$$\mathrm{R}_x(t,\tau) = \lim_{N\to\infty} \sum_{n=-N}^{N} x\Big(t+nT+\frac{\tau}{2}\Big)x^*\Big(t+nT-\frac{\tau}{2}\Big) \tag{2.33}$$

where n is an integer and T is the period. Equation (2.33) is the well known limit periodic autocorrelation. As one can see, this is a synchronized average, in which the

averaging is performed over the same signal shifted by an integer number of periods, where this shifting is done an infinite number of times. As long as the data are uncorrelated, this is equivalent to an infinite number of different realisations of the signal, which is the conventional ensemble average.

Because of the autocorrelation function of equation (2.33) is periodic, it can be expanded into a Fourier series. The coefficients of this decomposition are the cyclic autocorrelation functions, given by:

$$\mathrm{R}_x^{\alpha}(\tau) = \lim_{T\to\infty} \int_{-T/2}^{T/2} x\Big(t+\frac{\tau}{2}\Big)x^*\Big(t-\frac{\tau}{2}\Big)e^{-j2\pi\alpha t}dt \tag{2.34}$$

where α is called the cyclic frequency.

A useful tool for displaying the cyclostationary properties of a signal is the spectral correlation density (SCD). This function is defined as the Fourier transform of the cyclic autocorrelation function, and is given by:

$$S_x^{\alpha}(f) = \int_{-\infty}^{+\infty} R_x^{\alpha}(\tau)e^{-j2\pi f\tau}d\tau \tag{2.35}$$

This function depends of two frequencies: the spectral frequency f and the cyclic frequency α. When $\alpha = 0$ the SCD is equal to the power spectral density of the signal $x(t)$, whilst at other values of α the SCD is the cross-spectral density of the signal $x(t)$ and its shifted version by frequency α.

It is important to notice that, as shown in equation (2.11), the Fourier transform of the autocorrelation function leads to the Wigner distribution. Therefore the SCD can be obtained from the Fourier series expansion of the WD, as depicted in Figure 2.13, which shows the relationships among the autocorrelation function, cyclic autocorrelation function, spectral correlation density function and the Wigner distribution.

As a first measure of the existence of cyclostationary components in a signal, the degree of cyclostationarity (DCS) function of the signal can be used, defined for con-

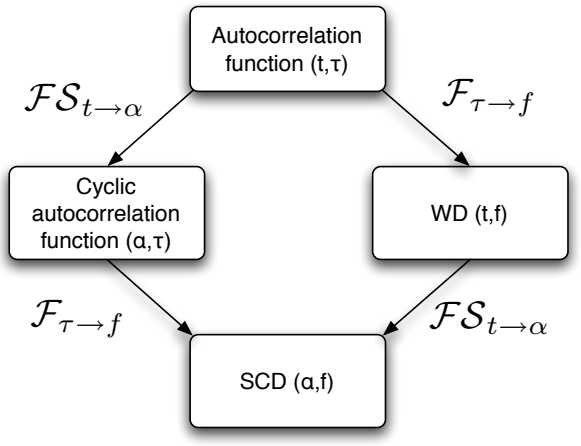

Figure 2.13: Relationships among: Autocorrelation function, Cyclic Autocorrelation function, Cyclic Spectral Density function and Wigner distribution ($\mathcal{F}$ denotes the Fourier transform, whilst $\mathcal{FS}$ denotes the Fourier series expansion)

tinuous signals as follows [5]:

$$DCS^{\alpha} = \frac{\int_{-\infty}^{+\infty} |\mathrm{R}_x^{\alpha}(\tau)|^2 d\tau}{\int_{-\infty}^{+\infty} |\mathrm{R}_x^{0}(\tau)|^2 d\tau} \tag{2.36}$$

The DCS function presents a non-dimensional quantity, which is a measure of the degree of cyclostationarity of a certain frequency α.

Numerical implementation

The cyclic spectral analysis algorithms generally are subdivided into two classes, averaging in frequency (frequency smoothing) or in time (time smoothing). Time smoothing algorithms are considered to be computationally more efficient for general cyclic spectral analysis, while frequency smoothing algorithms can be computationally superior to the time smoothing ones in certain restricted cases, such as estimation of the cyclic spectrum for small time-frquency resolution product. Computationally efficient algorithms for the SCD estimation can be found in [36–38], while non-parametric cyclic spectral estimators are explained by Antoni in [39]. The frequency smoothing algorithms are FFT based time smoothing algorithms, which are obtained via modification of the kernel transform. A particular computationally efficient FFT based algorithm is the strip spectral correlation algorithm (SSCA), which

is subsequently described.

All time smoothing algorithms, including SSCA are based on the time smoothed cyclic cross periodogram [29]

$$S_x^{\alpha}(n,f)_T = \frac{1}{T}\Big\langle X_{T_0}\Big(n, f+\frac{\alpha}{2}\Big)X_{T_0}^{*}\Big(n, f-\frac{\alpha}{2}\Big)\Big\rangle_T \tag{2.37}$$

where $\langle\cdot\rangle$ is the usually time-averaging operation:

$$\langle\cdot\rangle = \lim_{T\leftarrow\infty}\int_{-T/2}^{T/2}\cdot\ dt \tag{2.38}$$

The physical interpretation of equation (2.37) is the correlation of spectral components of $x(t)$ over time span of T seconds.

As Robert said in [36]: "the spectral component $X_{T_0}\Big(n, f+\frac{\alpha}{2}\Big)$, also colled complex demodulates, is the complex envelope of narrow-band, bandpass component of a signal".

The mathematical formulation of the complex demodulate is the following:

$$X_{T_0}(n,f) = \sum_{r=-N'/2}^{N/2} a(r)x(n-r)e^{-j2\pi f(n-r)f_s} \tag{2.39}$$

where $a(r)$ is a data tapering window of duration $T_0 = N'f_s$, with f_s being the sampling period. The value of N' is determined according to the desired frequency resolution (Δf) used in the algorithm, and is given by:

$$N' = \frac{fs}{\Delta f} \tag{2.40}$$

The Fourier transform of $a(r)$ plays the role of spectral window. The spectral window shape is of pivotal importance during data analysis. De facto, data occurring away form the central lobe of the spectral window are attenuated with respect to the data occurring at the aperture window center. In this work an Hamming window is used for the input bandpass filters.

Firstly, the complex demodulates are computed at each instant, after that they are correlated by time averaging their conjugate product over a time interval T as follow:

$$S_x^{\alpha_0}(n, f_0)_T = \sum_{r=1}^{N} X_{T_0}(r, f_1) X_{T_0}^*(r, f_2) g(n-r) \tag{2.41}$$

where $g(n)$ is a data tapering window of width $T = Nf_s$. The resulting output sequence is the spectral cross correlation estimate at point (f_0, α_0). The complex demodulate frequencies f_1 and f_2 are related to the spectrum frequency f_0 and the cyclic frequency α_0 of the estimated point, by the following relations:

$$f_0 = \frac{f_1 + f_2}{2} \qquad \alpha_0 = f_1 - f_2 \tag{2.42}$$

Figure 2.14 shows a basic implementation of the discrete time smoothed cyclic cross periodogram, where the symbol $*$ stands for complex conjugation. The SCD eval-

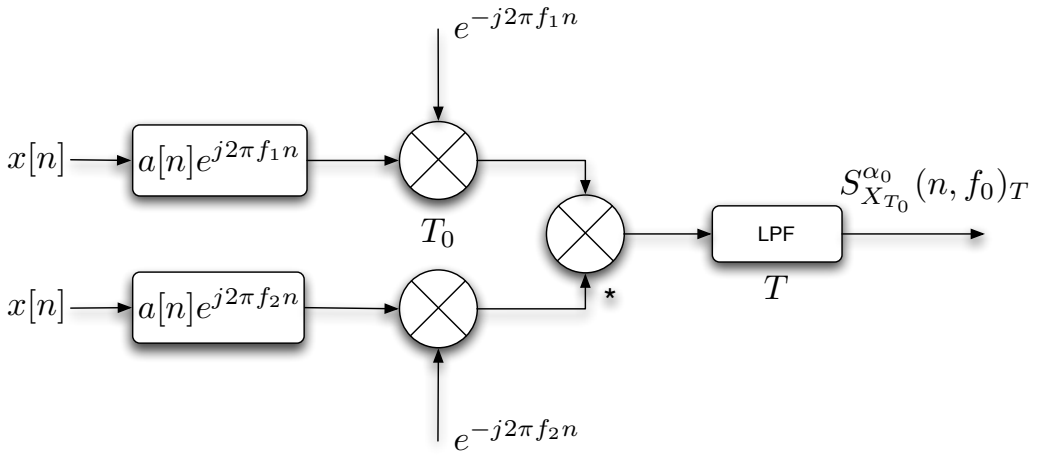

Figure 2.14: Flow chart of the time smoothed cyclic cross periodogram

uation using the time smoothed cyclic cross periodogram becomes extremely time-consuming. In fact equation (2.41) converges to cyclic cross spectrum as T goes to infinity, therefore it is necessary to keep the sample numbers N as large as possible. Since N increases the number of complex multiplications rapidly grows as well as the computationa effort.

The SSCA overcomes the limitations of the time smoothed cyclic cross periodogram.

The mathematically formulation of the SSCA is the follow [38]:

$$S_x^{f_k+q\Delta\alpha}\Big(n, \frac{f_k}{2} - q\frac{\Delta\alpha}{2}\Big)_T = \sum_{r=1}^{N} X_{T_0}(r, f_k)x^*(r)g(n-r)e^{\frac{-j2\pi qr}{N}} \tag{2.43}$$

where $f_k = kf_s/N'$ with $-N'/2 \leqslant f_k \leqslant N'/2 - 1$.

The complex demodulated sequence is directly multiplied by the signal complex conjugate. Then, the resultant signal is smoothed in time by means of a N-point FFT, where N is the total number of data samples. As a result, the estimated points of the SSCA lies along frequency skewed family of lines at $\alpha = 2f_k - 2f$, as showed if Figure 2.15 in case of $N' = 8$. As a consequence in order to obtain a proper representation of the SCD a reordering operation is needed. The SSCA flow chart is depicted in Figure 2.16.

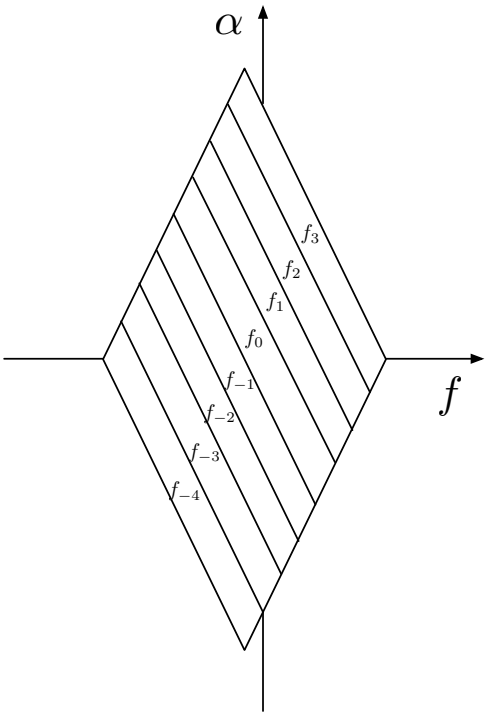

Figure 2.15: Bi-frequency plane for the strip spectral correlation algorithm for $N' = 8$

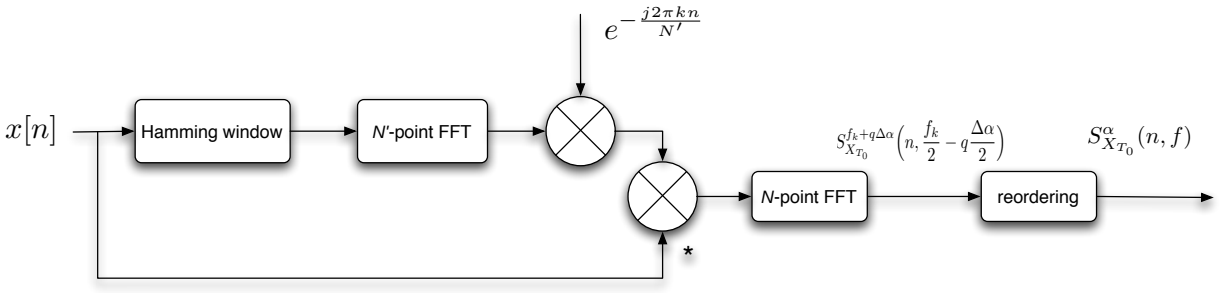

Figure 2.16: Flow chart of the strip spectrum correlation algorithm

The SSCA is an high computational efficiency algorithm only in restricted cases, e.g. for estimating the cyclic spectrum for a few values of cycle frequency or estimating the cyclic spectrum for small time-frequency resolution product. Therefore, is subsequently investigated the uses of the WVD for the evaluation of the SCD spectrum.

The following amplitude modulated signal is now takes into account:

$$y(t) = X_n[1 + A_m cos(2\pi f_r t)]sin(2\pi f_m t) + n(t) \tag{2.44}$$

where $n(t)$ is a normally distributed random noise of zero mean. Data are depicted in the following table.

Table 2.1: Matlab code data

X_m	1
A_m	0.3
f_r [*Hz*]	5
f_m [*Hz*]	20

The SCD is now evaluated via the Fourier series expansion of the WVD. The signal of equation 2.44 is synchronously sampled over a period $T = 1/f_r$ with 1024 point per revolutution. If the signal noise is zeroed, the SCD amplitude is shown in Figure 2.17 (a), for a frequency band of 10-30 *Hz* and for a cycle frequency band of 0-10 *Hz*. Figure 2.17 (b) plots the SCD of the noisy signal in which no average are performed. Therefore, in order to reduce the noisy component in the SCD spectrum, synchronous averages have to be performed.

Figure 2.18 shows the SCD amplitude of the signal in equation 2.44 with two different number of averages. It is possible to notice that increasing the number of averages from 10 (2.18 (a)) to 40 (2.18 (b)) the amplitudes of the SCD components decrease.

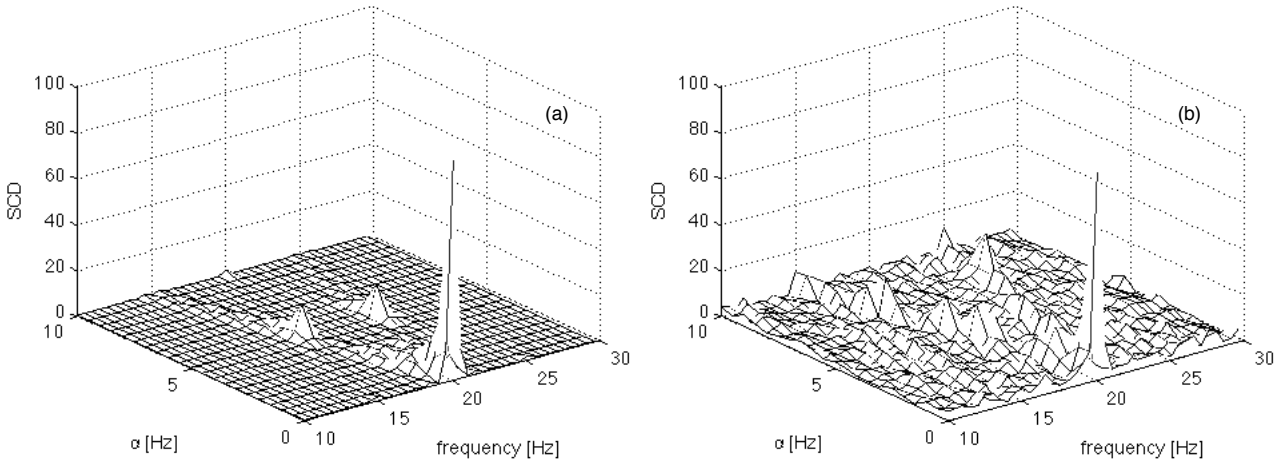

Figure 2.17: SCD of the simulated signal of equation 2.44 with: (a) $n(t)$ equal to zero and (b) $n(t)$ equal to a normally distributed random noise of zero mean

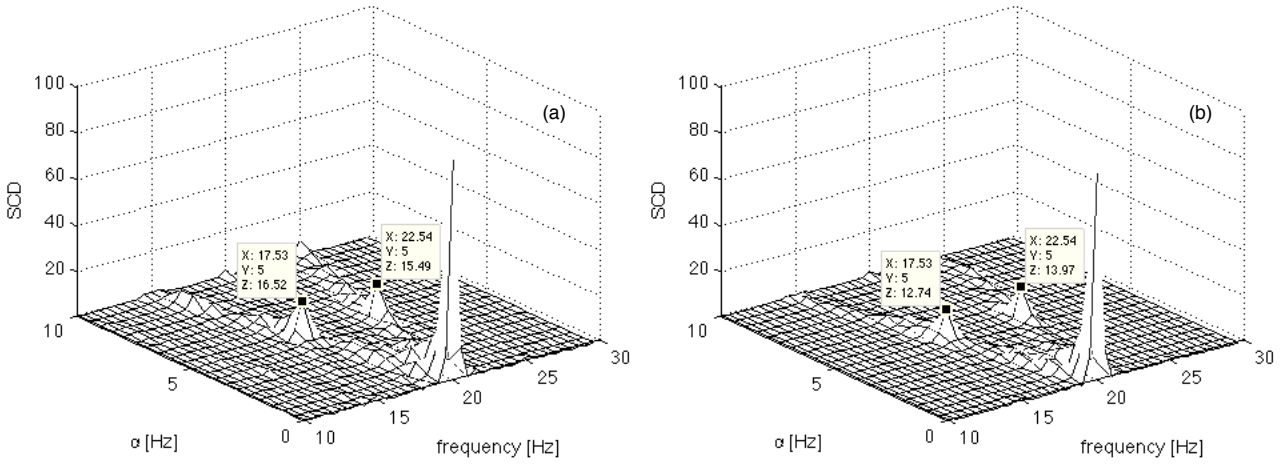

Figure 2.18: SCD of the simulated signal of equation 2.44: (a) 10 synchronous average are performed on the time signal and (b) 40 synchronous average are performed on the time signal

Chapter 3

IC engine assembly fault diagnostics

Life is too short to spend writing do loops

Moler, 1993

This chapter concerns the diagnosis of IC engine assembly faults. The pivotal causes of these type of faults are irregular activities during the engine assembling operations. These irregular activities can be detected by means of a "could test". Nowadays, companies have introduced this test at the end of the assembly lines in stead of a time consuming "hot test" (e.g. a test on which the engine is fairing). Undeniably, these two tests are different, indeed hot test aims to verify the engine performance, whilst the cold test aims to verify the anomalies by means of torque, pressure and vibration measurements.

At present, the hot test technology only indicates to the manufacturer which engines are not good for customers, but does not give any more information regarding the causes of the fault producing the malfunction. Furthermore, for could test the amount of time and costs are less than for the hot one. As a matter of fact that hot test give auxiliary costs for oil and fuel consumption, bench's maintenance and, in addition, a complete hot test procedure takes more than ten minutes instead of three of the could one. Further detail about the could test can be found in [40].

In this study two types of assembly faults are considered, that are subsequently described. The acceleration signals were acquired from the engine block during a cold test cycle at the end of the assembly line in sound and faulty conditions. Ad-

vanced signal processing techniques are applied on the acceleration signal, in order to highlight the techniques sensitivity for these types of defects. The IC engine signals are analyzed as suggested by Antoni et al. in [6]. The flow chart of the condition monitoring procedures for the considered faults is shown in Figure 3.1. Firstly the

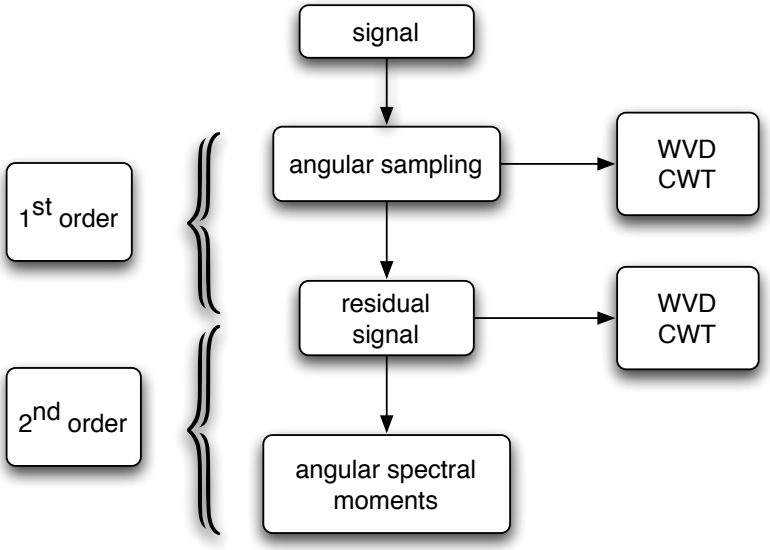

Figure 3.1: Condition monitoring procedure flow chart

signal is synchronously sampled and the time-synchronous average is computed over two crankshaft rotations. All the subsequently first level techniques are evaluated over the time-synchronous averaged signal. The Wigner-Ville distribution (WVD) is compared with the continuous wavelet transform in order to highlight the differences of these techniques in vibration based condition monitoring. Subsequently the residual signal is evaluated by subtracting, from the synchronized signal, the time-synchronous average. In fact the periodicities due to the normal engine operating conditions are zeroed in the residual signal, which can therefore points out the power linked to the fault. Both WVD and CWT are applied on the residual signal, moreover, this signal is analyzed by means of the WV spectrum and the mean instantaneous power, as suggested by Antoni at al.in [6].

3.1 Experimental apparatus and fault descriptions

Tests are carried out on a VM Motori turbocharged 2.8 L diesel engine, 4-cylinder 4-stroke with four-valve-per-cylinder (Figure 3.2).

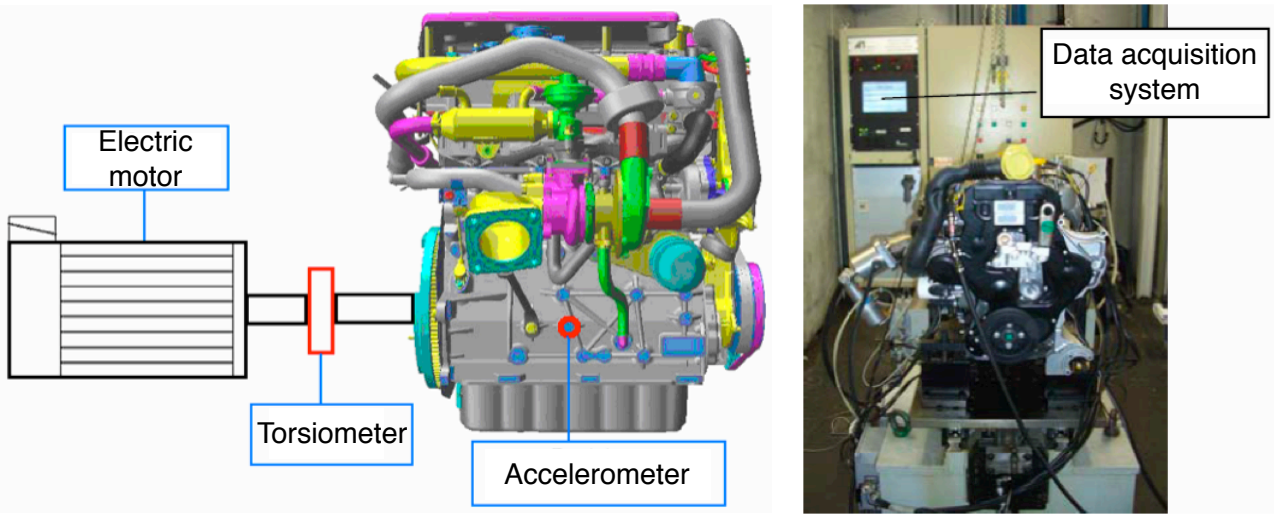

Figure 3.2: Could test bench: 2.8 l VM engine and acquisition system

During tests the engine is driven by an electric motor and it is maintained in a non-firing state. The vibration signal is acquired by means of a piezoelectric general purpose accelerometer mounted nearby bearing support of the crankshaft (Figure 3.2). The vibration signal is acquired at a constant engine operational speed of 1000 *rpm*, with a sample frequency of 14 *KHz* to an extent of 2 *s*.

An experimental campaign is performed over engines in sound and faulty conditions. In more detail, eight engines in faulty conditions are considered, in which different assembly faults were artificially introduced one by one in the engines. Additional details about this test campanign and assembly faults can be found in [40, 41]. In this study only two faulty engines are take in to account, which are listed and described below:

- ✗ *Inverted piston* (Figure 3.3 (a)): the piston is mounted rotated in such a way that there is a non correct positioning of the valve sites. As a matter of fact that the intake valve site area is larger than the exhaust valve site one, so due to the not correspondence between the valve plates and the proper

valve sites, during the engine cycle the intake valves hit the exhaust valve sites.

✗ *Road tight with a pre-load of only 3 kgm and not with the correct* (Figure 3.3 (b)): the correct tight load of the road screws is of 9 *kgm*, this non-whell screws tight causes an irregular rotation of the rod that affect the stroke of the piston, causing incorrect engine operation and hits.

Figure 3.3: Mechanical devices involved in faulty conditions: (a) inverted piston, (b) rod pre-loaded

First of all, ten sound engines are tested, in order to obtain statistical parameters. These values are used to achieve an upper threshold value (such as mean and RMS values), distinguishing the faulty conditions from the sound one in a "*pass/fail*" decision procedure (see [40]). The sound RMS and peak vibration values are listed in Tables 3.1 and 3.2 respectively.

Table 3.1: IC engines: healthy RMS values

Engine number	RMS value [g]
7331	0.1280
7332	0.0920
7333	0.0979
7356	0.0841
7357	0.0915
7358	0.1178
7421	0.1164
7422	0.1683
7423	0.1020
7518	0.1190
Mean + 3 Sigma	0.1853

Table 3.2: IC engines: peak values

Engine number	peak value [g]
7331	0.694400
7332	0.563000
7333	0.504100
7356	0.449428
7357	0.338000
7358	0.869460
7421	0.549720
7422	1.062900
7423	0.527040
7518	0.361510
Mean + 3 Sigma	1.2715

3.2 IC Engine assembly faults: vibration signal model

This section concerns on the mathematical vibration signal model for IC engine assembly faults. The model presented in this work was proposed by Antoni et al. in [6], which concerns on a stochastic vibration signal model. In general the vibration signal ($x(t)$) acquired from an IC engine can be expressed in the form [6]:

$$x(t) = x_d(t) + x_{nd}(t) + n_s(t) \tag{3.1}$$

where $x_d(t)$ and $x_{nd}(t)$ are respectively the deterministic and non-deterministic part of the signal. The non-deterministic part takes into account the random fluctuations around $x_d(t)$. An additional terms is also considered $n_s(t)$, which accounts for some background noise. Let T the non-rarandom period of the engine cycle. Then $x_d(t)$ is first order cyclostationary:

$$\mathrm{E}\{x_d(t)\} = x_d(t+T) \tag{3.2}$$

and, without loss of generality, $x_{nd}(t)$ is set to be second order cyclostationary:

$$\mathrm{R}_{x_{nd}x_{nd}}(t,\tau) = \mathrm{R}_{x_{nd}x_{nd}}(t+T,\tau) \tag{3.3}$$

whilst $n_s(t)$, as previously said is stationary. As a matter of fact that, in order to single out the cyclostationary content of the signal $x_{nd}(t)$, it is necessary to impose that $x_{nd}(t)$ and $n_s(t)$ are uncorrelated processes.

As explained by Antoni et al. in [6], the vibration signature of an IC engine is composed by a series of evanescent oscillations due to impact forces associated at the main events, which occur during the engine operation. As a matter of fact that, during the engine operation, impact forces arises at the openings and closures of valves, fuel injections (in diesel engines) and rapid rising of gas pressure during the combustion. Figure 3.4 shows the complete event diagram for a 4-stroke 4-cylinder diesel engine, in which the arrow amplitudes are roughly proportional to the impact force magnitudes. Therefore, in this work, the deterministic part of the expected

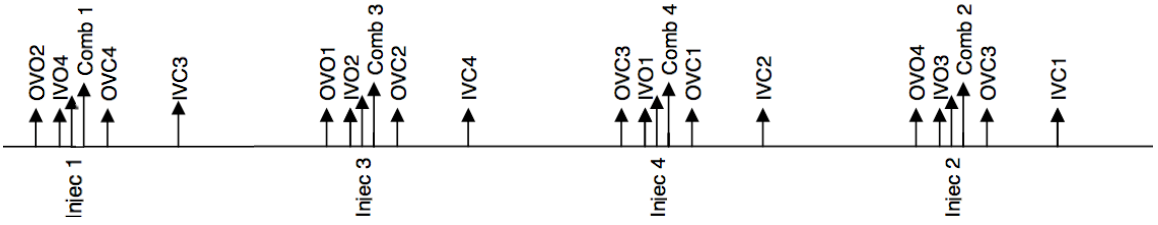

Figure 3.4: Engine event diagram: occurrences of combustion, fuel injection, input valve opening (IVO) and closure (IVC) and output valve opening (OVO) and closure (OVC)

vibration signal is set equal to a series of impulse response function, such as:

$$x_d(t) = e^{-\theta_{imp}/0.001} X_d cos(2\pi f \theta_{imp}) \tag{3.4}$$

where θ_{imp} defines the beginning of an engine event. Each term of the left-end side of equation 3.4 is the evanescent oscillation that occurs in the vibration signal. The cyclostationary signal counterpart is modeled as a cyclic impulse modulated noise. Figure 3.5 depicts the vibration signal model considering only engine pressurizations, whilst Figure 3.6 plots the two parts in which the vibration signal model is composed. In particular Figure 3.6 (*a*) shows the stationary part of the vibration signal model concerning only the pressurization of the four cylinders, while Figure 3.6 (*b*) plots the cyclostationary one plus stationary random noise.

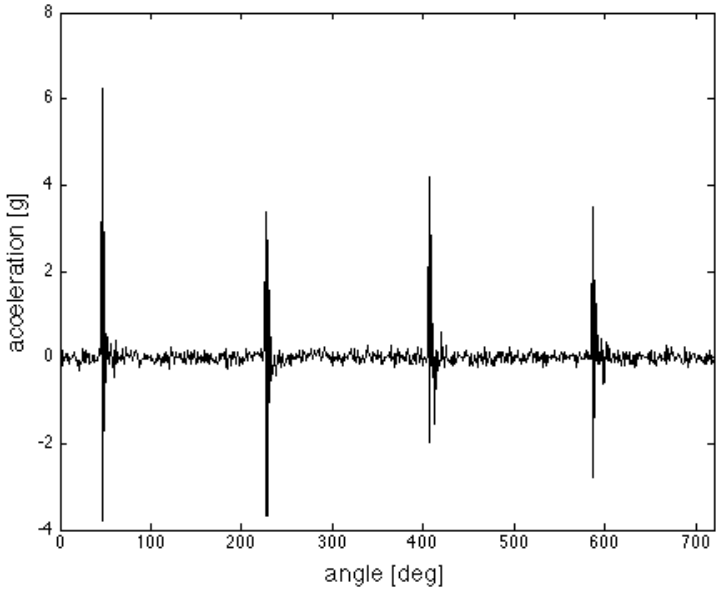

Figure 3.5: IC engine vibration signal model considering only engine pressurizations

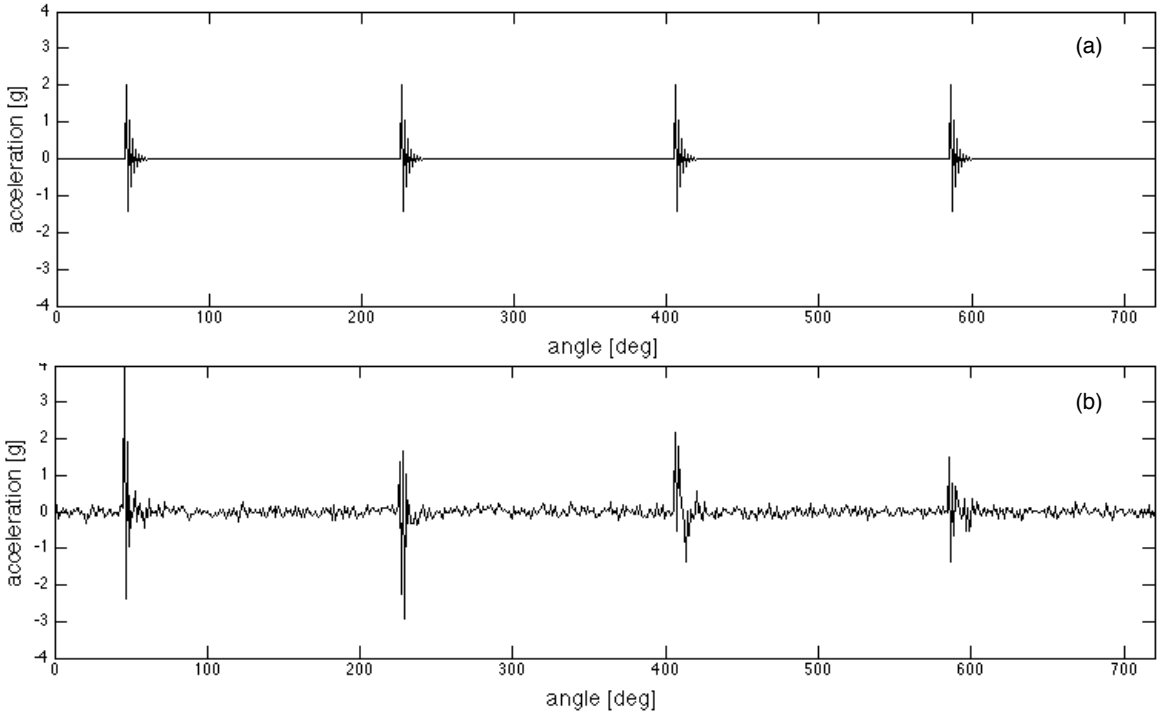

Figure 3.6: IC engine vibration signal model considering only engine pressurizations: (a) stationary part, (b) cyclostationary part

3.3 Inverted piston: data analysis

Figure 3.7 plots the vibration time signal acquired form the engine block. In this case one of the four engine pistons is assembled inverted. This time signal presents marked acceleration peaks, mainly arisen form the healthy cylinder. Firstly this sig-

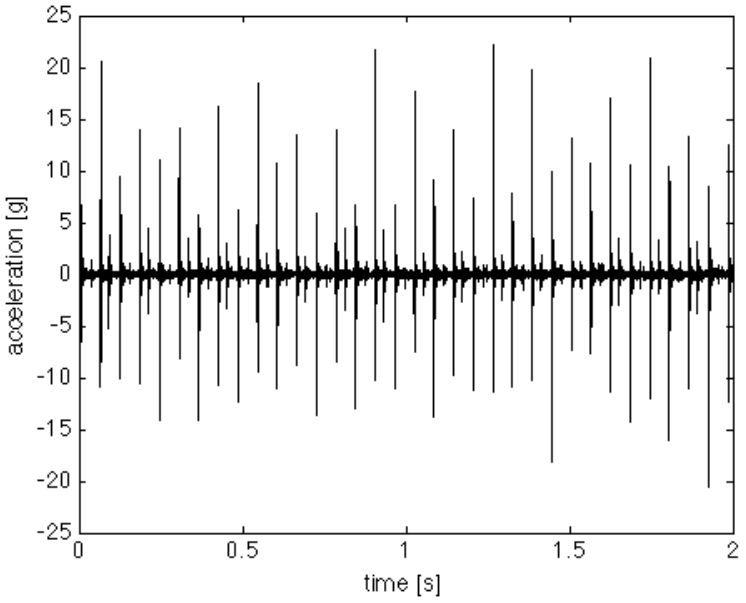

Figure 3.7: Inverted piston: time signal

nal is synchronously resampled. The information about the rotational position of the engine is generated using signal peaked up by a crank sensor with 360 *pulse/rev*. The synchronous average is shown in Figure 3.8 (a), whilst Figure 3.8 (b) plots the comparison among RMS and Peak vibration values both in sound and faulty conditions, where the RMS and Peak values in sound condition are obtained from Tables 3.1 and 3.2.

The vibration signal synchronous average is evaluated over two crankshaft rotations because, as a matter of fact that, the periodicity of a 4-stroke engine is of two crankshaft rotations. This synchronous average completely depicts the nature of the signal. In fact, one can see that the signal period is mainly composed by four impulse response, that are linked to the engine working cycle.

The comparison showed in Figure 3.8 (b) highlights the presence of a defect. In fact, both RMS and Peak signal values are greater than the sound ones. These results are plenty for a "*pass/fail*" decision procedure. The plot of Figure 3.8 (a) is

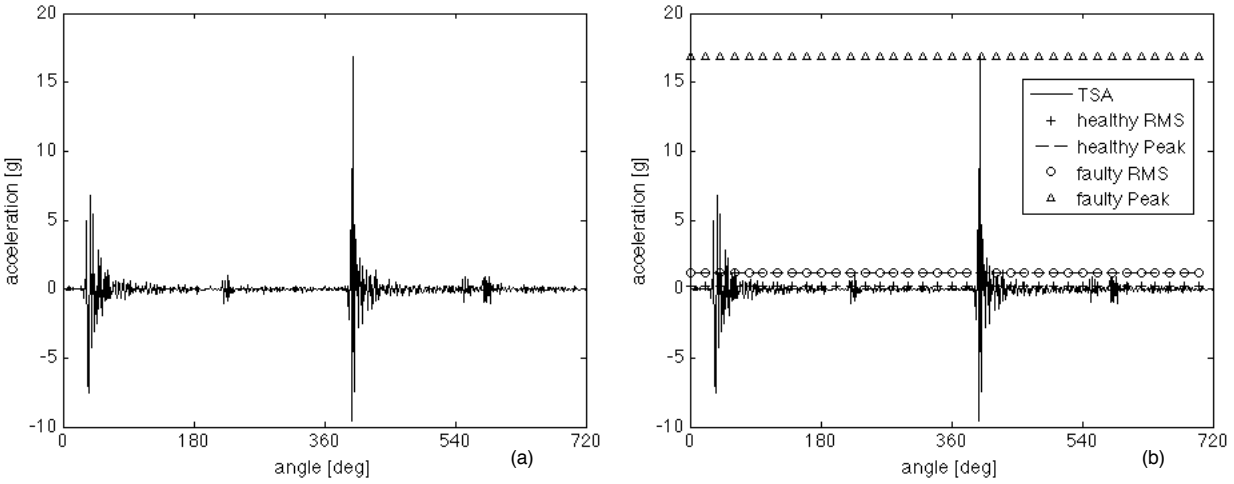

Figure 3.8: Inverted piston: time-synchronous average, faulty and healthy RMS values, faulty and healthy peak values

superabounded by two marked 360° spaced peaks. In order to better understand this result, one needs to associate at the synchronous average the engine event diagram (Figure 3.9). By this comparison one can notes that the pivotal variations in the synchronous average are related to the pressurization of cylinder 1 and to the opening of the intake valve 1. De facto, as previously said the intake valve site area is larger than the intake valve site one, so the intake valves hit the exhaust valve site areas. This phenomenon occurs two time per engine cycle. The first hit arise whet the piston 1 is on the top dead point (TDP) because, in diesel engine the combustion chamber volume is narrow, in order to achieve high compression ratio, so the intake valves hit the exhaust valve site areas on the piston. The second hit arise just before the TDP of piston 1 while the intake valves are opened. In order to confirm the presence and the location of the defect second order signal processing techniques are applied to this vibration signal.

Figure 3.10 plots the mean instantaneous power of the synchronous average (see Appendix A), highlighting the Peak value in the case of sound and faulty conditions,

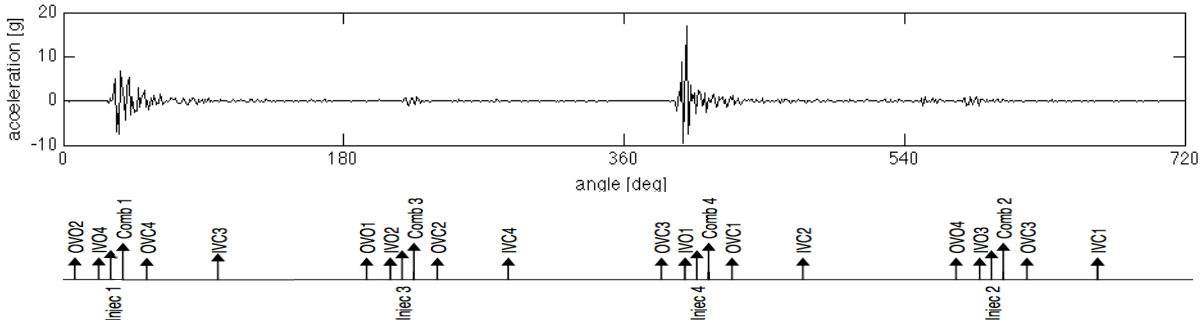

Figure 3.9: Inverted piston: time-synchronous average and engine event diagram

while in Figure 3.11 the mean instantaneous power is associated to the engine event diagram. Figure 3.10 clearly confirm the presence of a defect, by the comparison

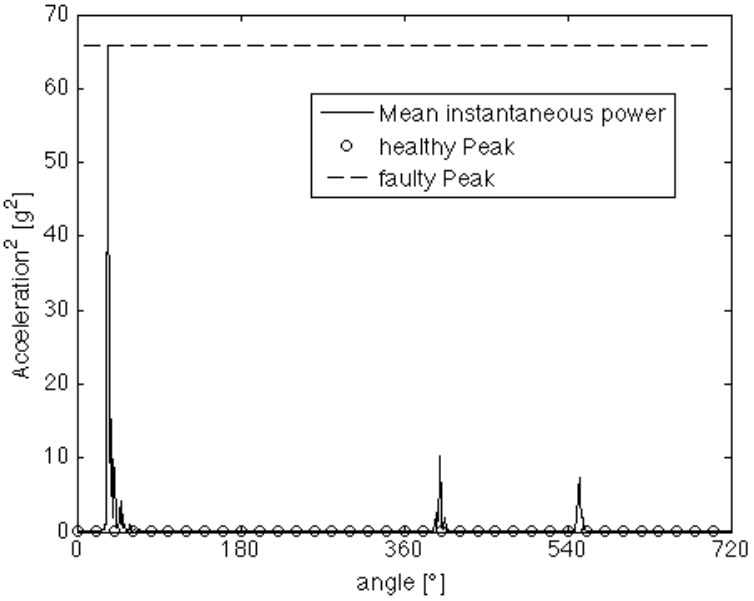

Figure 3.10: Inverted piston: mean instantaneous power, faulty and healthy peak values

of the Peak values and the average of the mean instantaneous power Peak values of sound motors. Moreover, by looking the event diagram one can notice that the largest energy amount is localized at the pressurization of the first cylinder, which confirm that the fault is located in the first cylinder.

Subsequently, the Wigner-Ville distribution (WVD) is evaluated on the synchronous averaged signal and on the residual signal. As previously said, the residual signal is obtained by subtracting the synchronous average from the time signal, highlighting

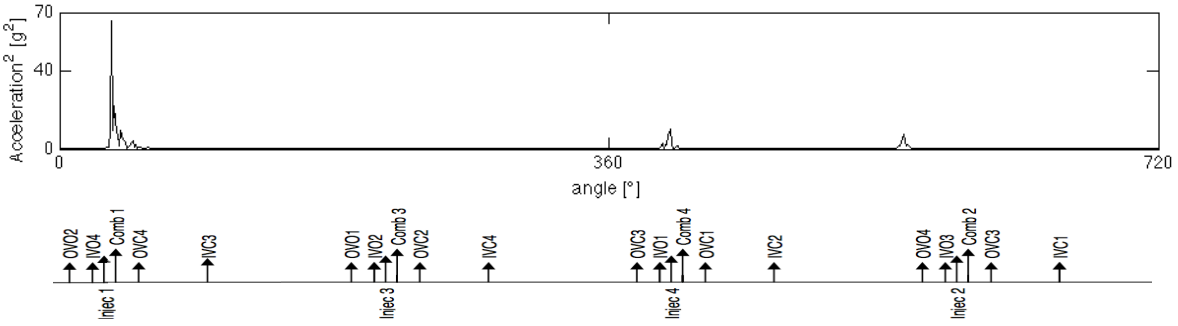

Figure 3.11: Inverted piston: mean instantaneous power and engine event diagram

so the cyclostationary signal content. The goal of this analysis is twofold: firstly the WVD can express the frequency content and location of the fault at the same time; secondly the WVD of the residual signal is clearer than the synchronous average one, because the deterministic part of the signal is zeroed and so largest energy content is localized at the fault position. At the end the WVD is compared with the continuos wavelet transform (CWT), in order to emphasize the differences of these techniques in vibration based condition monitoring. Figure 3.12 (a) plots the WVD of the syn-

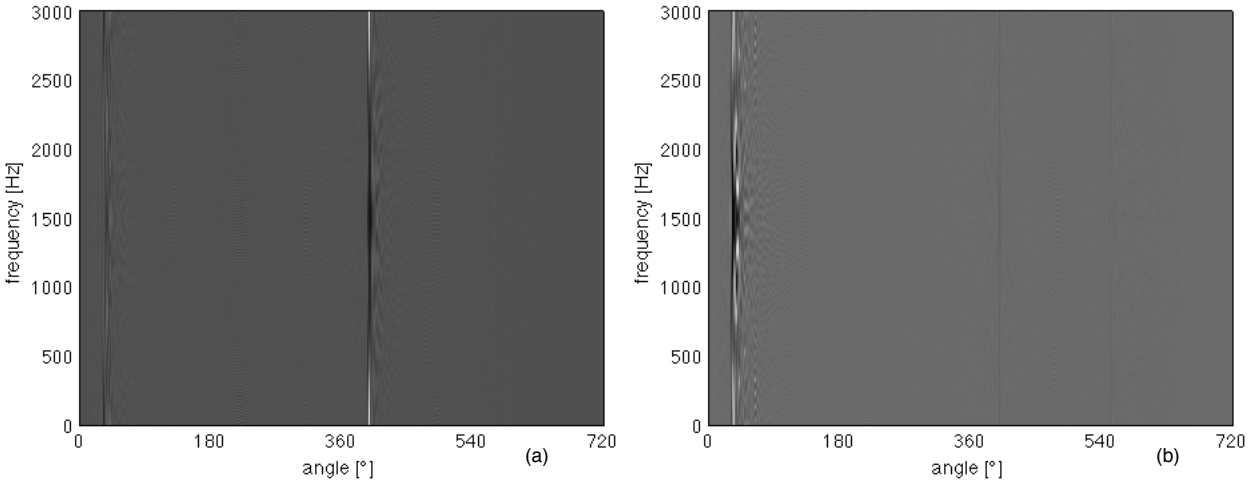

Figure 3.12: Inverted piston: Wigner-Ville distribution of the time-syncrhronous average, Wigner-Ville distribution of the residual signal

chronous average, on which the energy content is localized in two marked 360° spaced vertical lines. As previously said these are the energy contents due to the impacts at the first cylinder pressurization and at the closures of the first cylinder intake valves. Moreover, the fault location and its frequency content is well established from the

WVD of the residual signal, Figure 3.12 (b). As one can see, both WVD shown the presence and the location of the fault, however the WVD of the residual signal clearly evinces the fault frequency content.

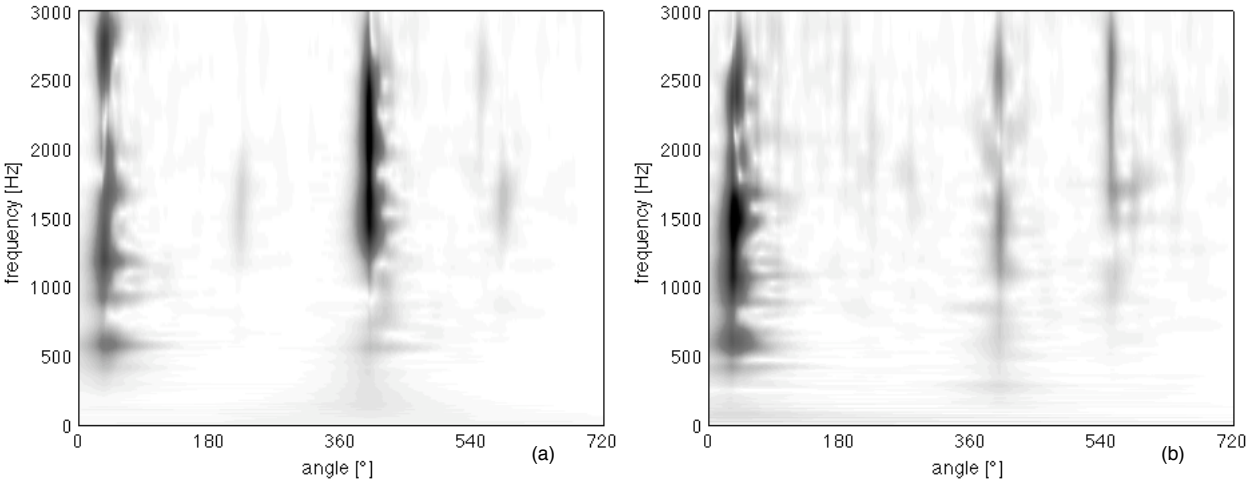

Figure 3.13: Inverted piston: CWT of the time-syncrhronous average, CWT of the residual signal

The CWT (impulse mother wavelt is used) of both synchronous average and residual signal are computed (Figures 3.13 (a) and (b)). The CWT detects the fault location even if, the frequency content is further spread in angle than the WVD. In spite of this one can clearly see that the CWT map is more clear than the WVD map due to the low level of the other frequency components (there are not cross-terms), yielding the fault detection straightforwardly. Moreover, the CWT map of the residual signal shows different engine events. In fact, the straight vertical line at about $553°$ can be related to the pressurization of the cylinder two, while the slightly visible vertical lines at about $188°$ and $225°$ can be related to the opening of the output valve and to the pressurization of the third cylinder respectively.

Therefore, both WVD and CWT are able to detect the assembly fault location and its frequency content. In addition CWT map of the residual signal is shown to be more sensitive that the WVD in engine event locations.

Finely, as proposed by Antoni at al. in [6], the Wigner-Ville spectrum (WVS) of the residual signal is computed and the results are shown in Figure 3.14. As defined by

Antoni the Wigner-Ville spectrum is the expected value of the WVD. As previously

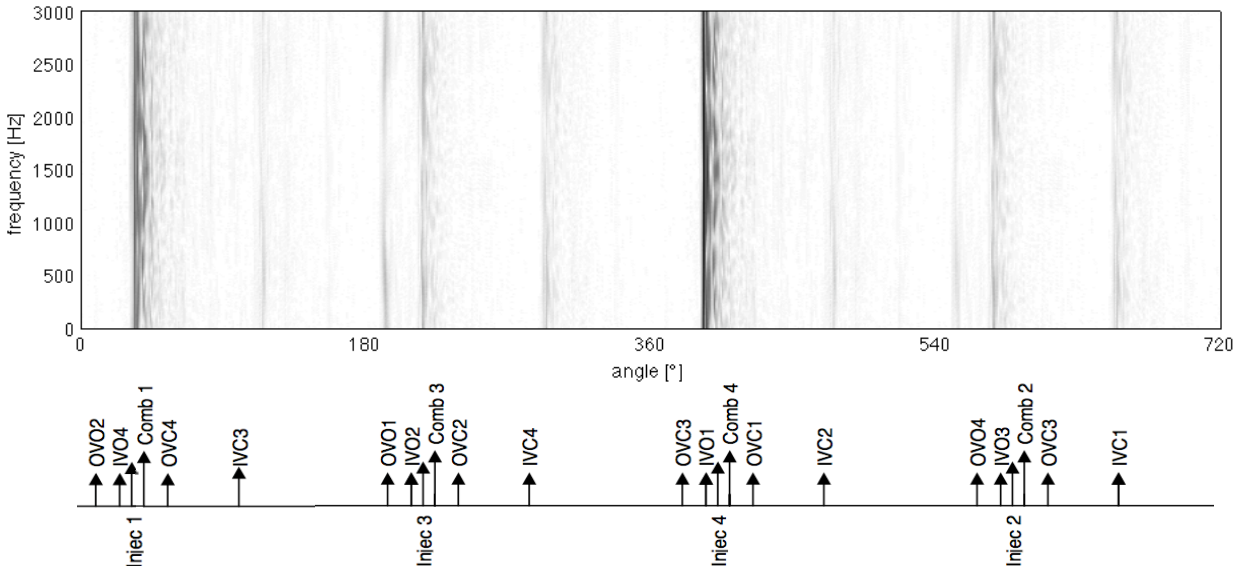

Figure 3.14: Inverted piston: Wigner-Ville spectrum

explained, the two clearly vertical lines concerning the pressurization of the first cylinder and the opening of the first cylinder intake valve are related to the mechanical fault. In addition further engine events are shown in the WVS. In particular the vertical lines at about $115°$, $294°$, $475°$ and $654°$ are related to the closure of the intake valves of the cylinders 3, 4, 2 and 1 respectively.

The two vertical lines around $193°$ and $216°$ are related to the opening of the first cylinder output valve and to the pressurization of the third cylinder, while the vertical lines at about 552 and 576 degrees correspond to the opening of the fourth cylinder output valve and to the pressurization of the second cylinder.

The small angular shift that occurs among the vertical lines of the WVS and the corresponding intake valve closure arrows in the event diagram is due to ordinary delay time of valve closure, which take place in practice.

3.4 Pre-loaded rod: data analysis

Figure 3.15 plots the vibration time signal acquired form the engine block. In this case one of the four engine rods is only pre-loaded and not completely tights. The time

signal present further acceleration peaks spread in the signal, just at the opposite of the foregoing case. As previously achieved the signal is synchronously resampled and

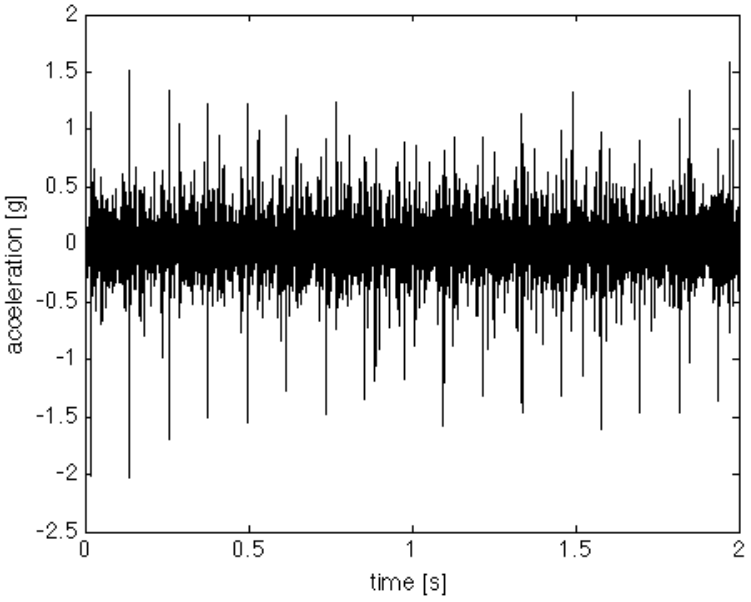

Figure 3.15: Connecting rod tight with a pre-load of only $3\,kgm$: time signal

the synchronous average is computed over two crankshaft rotations (Figure 3.16 (a)) and a comparison among sound and faulty RMS and Peak values is pointed out (Figure 3.16 (b)). In this case, the comparison among sound and faulty RMS and Peak

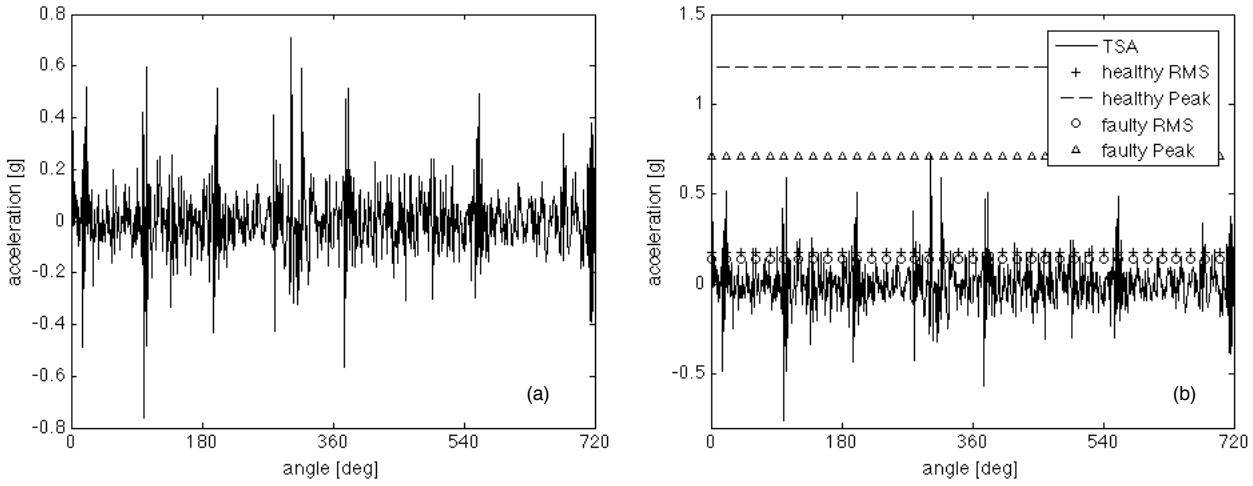

Figure 3.16: Connecting rod tight with a pre-load of only $3\,kgm$: (a) time-synchronous average, (b) faulty and healthy RMS values, faulty and healthy peak values

values (see Figure 3.16 (b)) does not reveal the presence of any defect. As it happens both healthy RMS and Peak signal values are under the sound one. Nevertheless, the acceleration peaks of the synchronous average can be physically explained by inspecting the engine event diagram (Figure 3.17). As shown in Figure 3.17, accel-

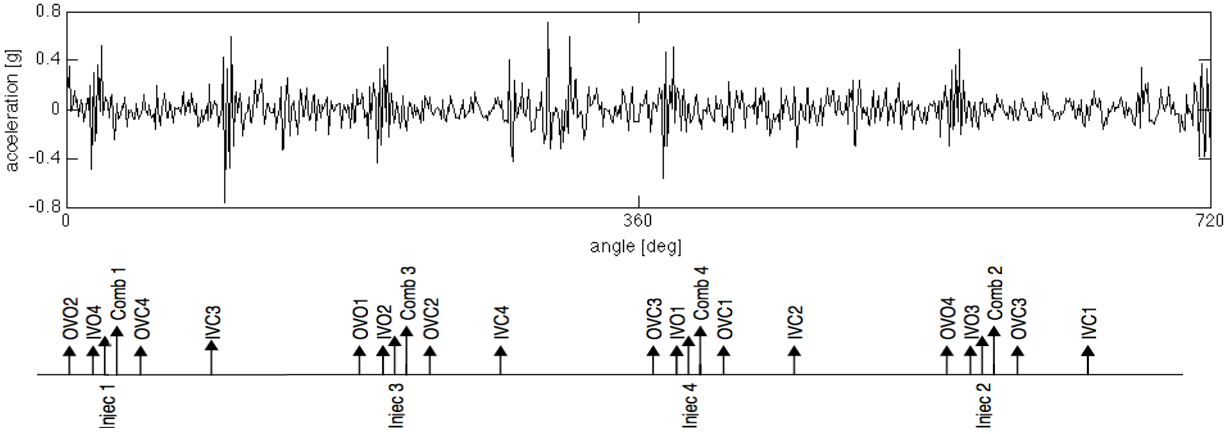

Figure 3.17: Connecting rod tight with a pre-load of only $3\,kgm$: time-synchronous average and engine event diagram

eration peaks are present on the pressurization of each cylinder. Moreover other acceleration peaks appear at the closure of the intake valves. In fact, due to the low tight of the rod screws, there are wide clearances between rod and crankshaft. These clearances are abruptly retrieved whereas there is a change in the resultant force acting on rod. The angular mismatch in the acceleration peaks and the closure of the intake valves of cylinders 3 and 4, are due to the ordinarily delay on the closure of the intake valves, which take place in practice.

Therefore, this type of analysis is inadequate to predict the presence and position of the fault. For that reason, a second order analysis is performed on the time-synchronous average. The mean instantaneous power of the synchronous average is evaluated and plotted in Figure 3.18, which also displays the healthy Peak value compared with the sound one. As one can clearly see, the presence of the defect is confirmed by the differences in the Peak values, the Peak value of the synchronous average mean instantaneous power is approximately ten times the sound one. Moreover, by the comparison with the engine event diagram (Figure 3.19), one can notice

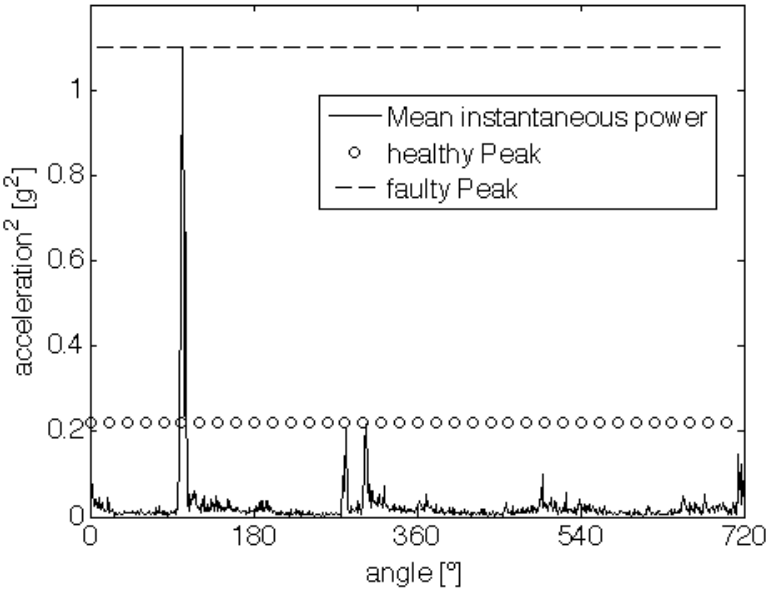

Figure 3.18: Connecting rod tight with a pre-load of only $3\,kgm$: mean instantaneous power, faulty and healthy peak values

that the largest energy amount is related to the closure of the third cylinder intake valves, which point out the defect location. So, the analysis of the mean instantaneous power makes know that the not correctly tight rod is located in the third cylinder.

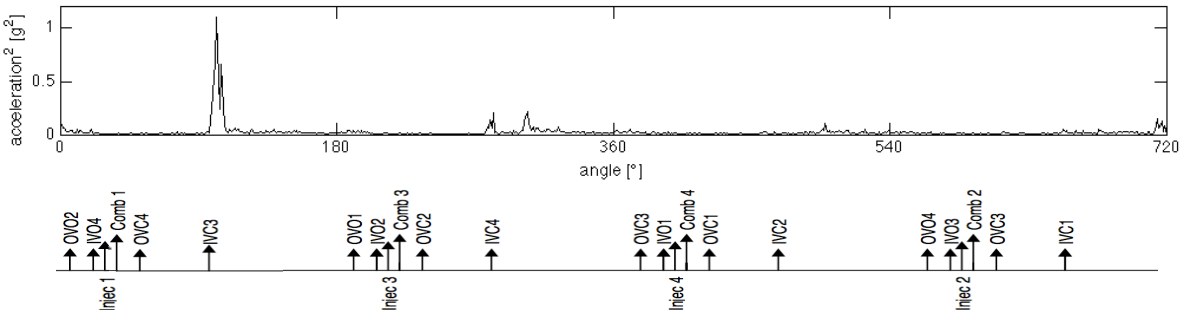

Figure 3.19: Connecting rod tight with a pre-load of only $3\,kgm$: mean instantaneous power and engine event diagram

As in the previous section the WVD of the synchronous average and the residual signal are computed and compared with the CW transforms respectively.

Figures 3.20 (*a*) and (*b*) plot the WV distributions of the synchronous average and residual signal respectively. The WVD of the synchronous average is of difficult inter-

pretation. De facto, according to Figure 3.16 (*a*), vertical lines appear at the pressurization of each cylinder and at the closure of the intake valves. Unfortunately, because of the acceleration amplitude associated to the engine events are about two times the background noise (see Figure 3.19), the vertical lines associated to the engine events are not clearly visible in the WVD, and in addition several cross-terms of relevant amplitude arise in the distribution. Therefore, the fault presence and its location con not be established from Figure 3.20 (*a*). For that reason the WVD of the residual

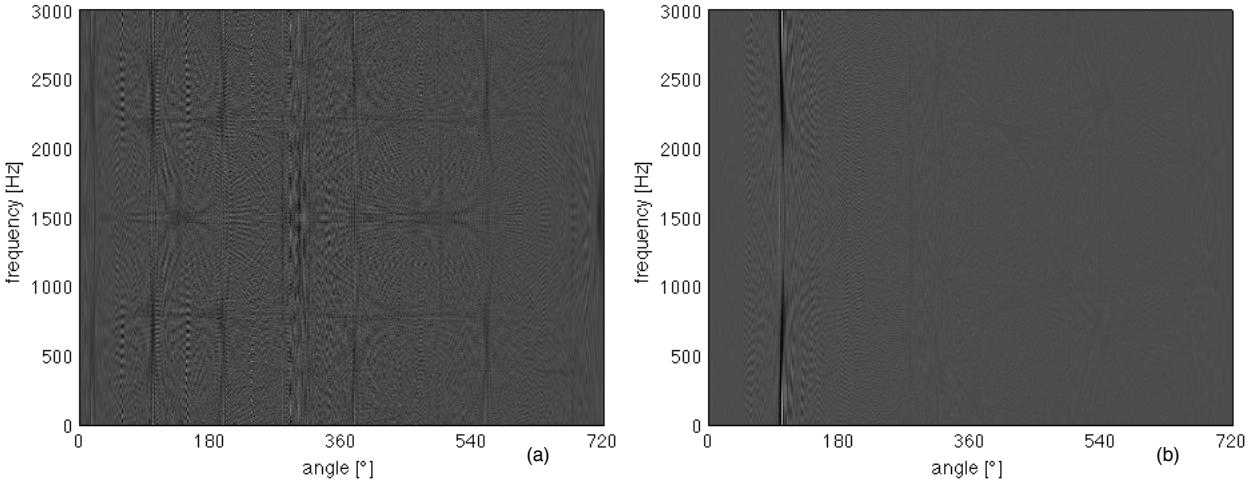

Figure 3.20: Connecting rod tight with a pre-load of only $3\,kgm$: Wigner-Ville distribution of the time-syncrhronous average, Wigner-Ville distribution of the residual signal

signal is computed (see Figure 3.20 (*b*)). As previously said, the residual signal take into account the cyclostationary content of the signal, and so by computing the WVD of this signal one can obtain a distribution in which the energy content is mainly restricted at the fault location. In fact, Figure 3.20 (*b*) have only a vertical line at the closure of the intake valves of the third cylinder where the rod is only pre-loaded. The CWT (impulse mother wavelt is used) of both synchronous average and residual signal are computed (Figures 3.21 (*a*) and (*b*)). As it happens before, the CWT map is more clear than the WVD. In particular the CWT map of the synchronous average (Figure 3.21 (*a*)) detects the four cylinder pressurization and the intake valve closure of the third cylinder, Figure 3.22. Even if a remarkable vertical line corresponding to the IVC3 is present in the CWT map of the synchronous average (Figure 3.22), it

is not enough in order to assure the presence of a mechanical fault. Therefore, the CWT of the residual signal is an expected step for the mechanical fault localization. As depicted in Figure 3.21 (*b*) the presence of the pre-loaded rod is highlighted by the marked vertical line at about $100°$.

Hence, as previously observed in WVD analysis, the fault location can by only achieved by the analysis of the residual signal.

Finally, the last proof of the mechanical fault presence can be obtained by the WVS of the residual signal. De facto, Figure 3.23 shows only a vertical line corresponding to the IVC3 highlighting so the fault location.

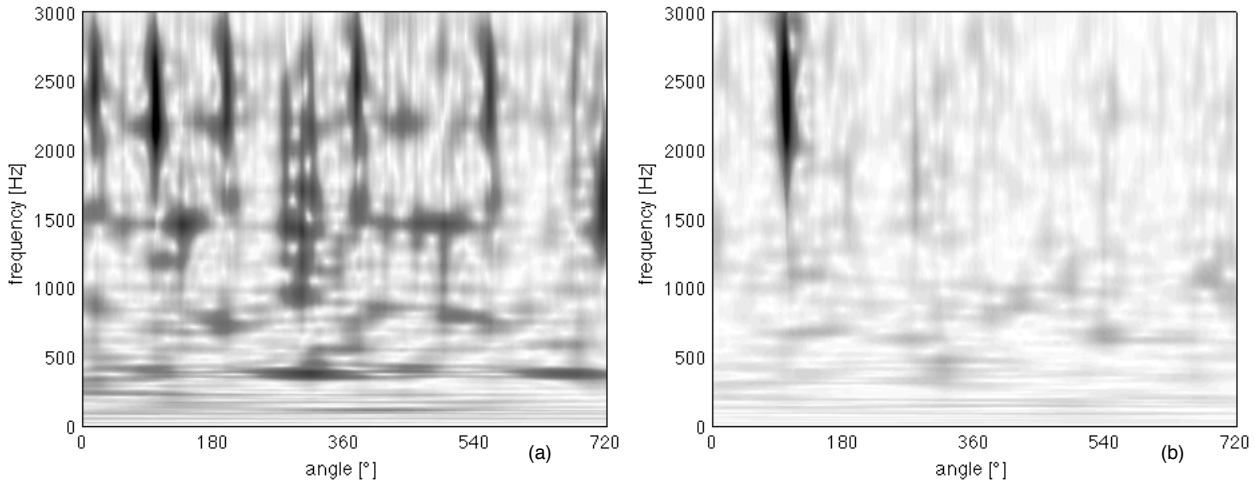

Figure 3.21: Connecting rod tight with a pre-load of only $3\,kgm$: CWT of the time-syncrhronous average, CWT of the residual signal

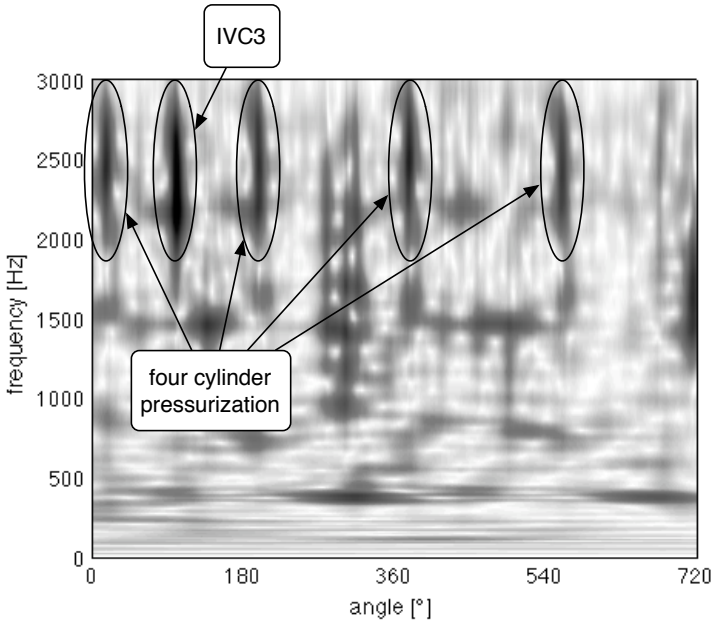

Figure 3.22: Connecting rod tight with a pre-load of only $3\,kgm$: CWT of the time-syncrhronous average

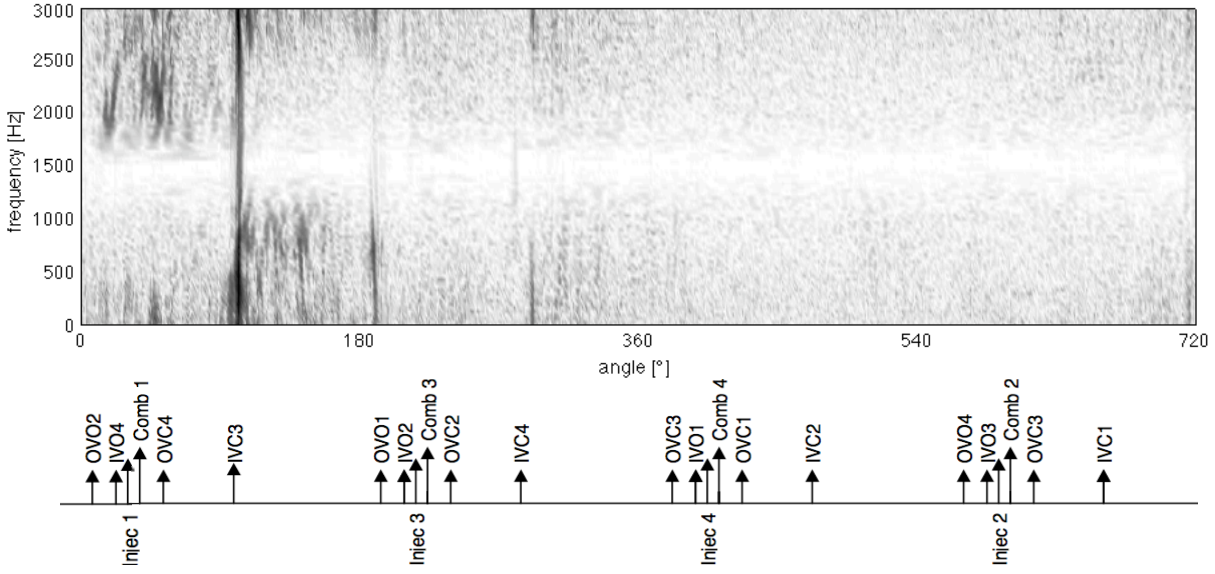

Figure 3.23: Connecting rod tight with a pre-load of only $3\,kgm$: Wigner-Ville spectrum

Chapter 4

Gear fault diagnositcs

Life is too short to spend writing do loops

Moler, 1993

The goal of this chapter is the analysis and diagnosis of gear faults. On this work two different types of faults are take into account. The first one is a fatigue crack at the tooth root and the other one are tooth spalls of different sizes. As previously said, only the test campaign concerning the tooth spalls is carried out in this work, whilst the data concerning the fatigue crack are obtained from a previous work of Dalpiaz et al. [42].

In the work carried out by Dalpiaz et al., tests were performed on a power circulating gear testing machine composed of two identical single-stage gear units mounted back to back, with a locked-in torque. Each gear unit contains a spur gear pair composed by a 28 teeth (pinion) and by a 55 teeth (wheel). Further data about gears and testing machine can be found in [42, 43]. A real fatigue crack is introduced in one of the wheel teeth mounted in one gear unit. The whole tooth flank is affected by the crack, which is extended between the two wheel faces. The experimental data concerning this work deal with two crack lengths, corresponding to about 20% (small crack) and 45% (large crack) of whole fracture surface after breakage, and are relative to a nominal pinion torque of $385 Nm$ and nominal pinion speed of $1000 rpm$; thus the meshing frequency is $466.67 Hz$.

The test campaign carried out in this work concerns the tooth spalls in helical gear.

The tooth spalls are mechanically introduced on the gear via a drilling process. In order to compare the sensitivity of different signal processing techniques to faults detection, different spall sizes were mechanically introduced along the gear tooth face. The spall position on the tooth face is chosen in such a way that, during the faulted gear tooth engagement, the tooth spall is crossed by the line of contact. In more detail, five different spall lengths are taken into account in this work, four of these are located at the mean point of the gear tooth face, whilst the last one is located nearby the beginning of the tooth face in such a way that, the smack affects only the beginning of the teeth contact during the gear meshing period. The spall dimensions are given with respect to the tooth length and are listed in Table 4.1, whilst some of these spalls are shown in Figure 4.1. A clamp device is build up in order to the well

Table 4.1: Dimensions of gear tooth spalls

ID	Fault description
Smack	2 *mm* along the tooth profile, 0.6 *mm* depth, 0.8 *mm* at the beginning of the tooth face
Sp12.5%	2 *mm* along the tooth profile, 0.6 *mm* depth, 2*mm* across the tooth face (12.5% of the tooth face width)
Sp25%	2 *mm* along the tooth profile, 0.6 *mm* depth, 4 *mm* across the tooth face (25% of the tooth face width)
Sp50%	2 *mm* along the tooth profile, 0.6 *mm* depth, 7.8 *mm* across the tooth face (50% of the tooth face width)
Sp100%	2 *mm* along the tooth profile, 0.6 *mm* depth, 15.5 *mm* across the tooth face (100% of the tooth face width)

positioning of pieces in the CNC drilling machine. Figure 4.2 (*a*) shows the drilling process, whilst Figure 4.2 (*b*) plots the clamp device. The correct position of gears during the drilling process is a pivotal goal for the process repeatability. As a matter of fact that the spall position with respect the gear tooth face have to be the same for all the tested gears. In order to achieve that, a gear tooth is built-up on the clamp device surface, which assures, by the engagement with the gear, the relative position of the gear tooth face with respect to the drill.

After the drilling process, the faulted gears are mounted in the first stage of a gear unit, which contains two spur gear pairs mounted back to back. The experimental apparatus is subsequently described in section 4.3.

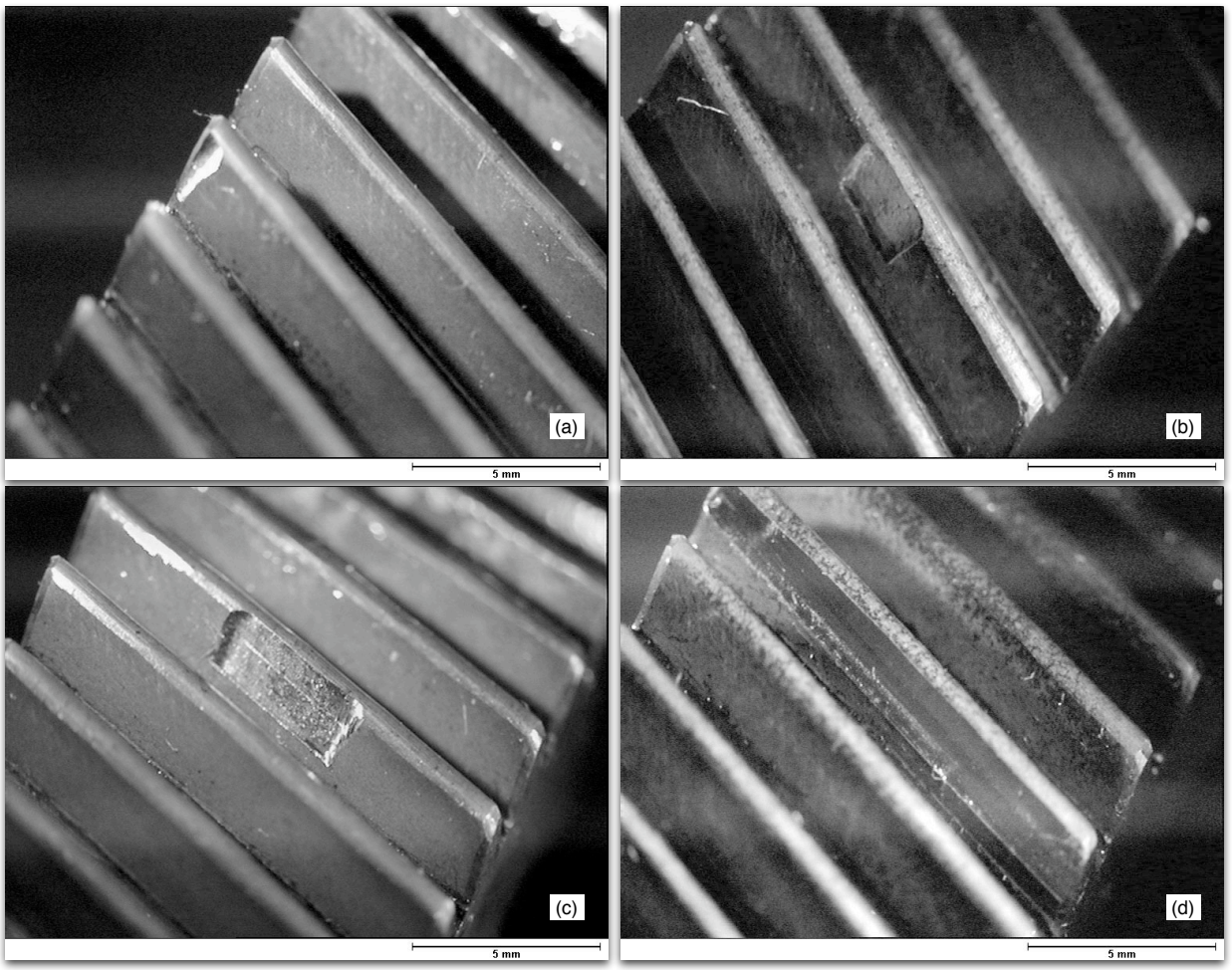

Figure 4.1: Gear tooth spall: (a) Smack, (b) Sp12.5%, (c) Sp25%, (d) Sp100%

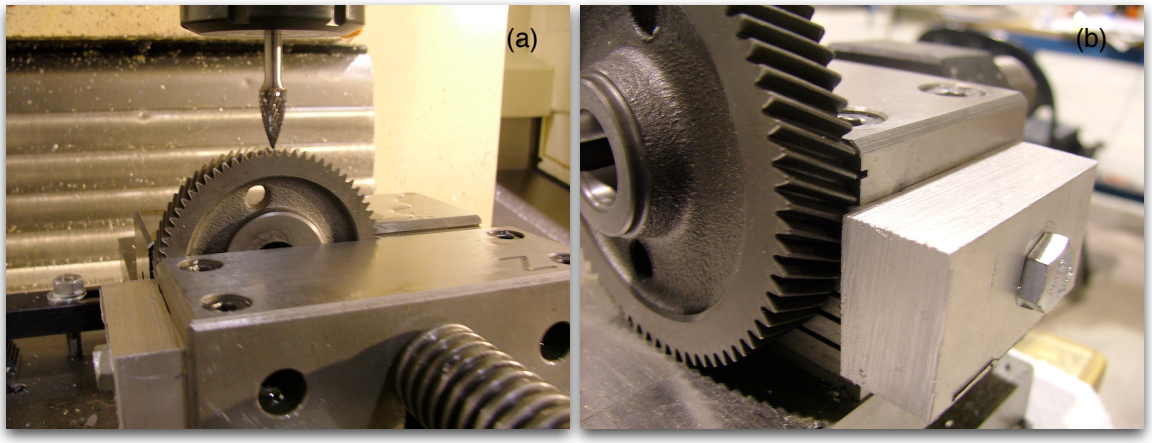

Figure 4.2: Gear tooth spall: (a) drilling process, (b) clamp device

The structure of the chapter is the follows: first of all the data concerning fatigue crack in gear tooth are analyzed, a vibration signal model for this type of fault is presented in section 4.1, whilst the analysis results are described in section 4.2; finally tooth spalls are taken into account, section 4.3 concerns the description of the "experimental model" used in order to carry out tests on faulty gears, while sections 4.4 and 4.5 describe respectively the vibration signal model and the analysis results for this type of fault.

4.1 Fatigue cracks: vibration signal model

In this section a mathematical explanation of the vibration produced by a spur gear pair affected by the presence of a fatigue crack in a tooth gear is presented. Several investigators focused their attention in this vibration signal model, such as [2, 42, 44, 45].

The principal source of vibratory excitation of a pair of involute gears is relative to the meshing forces. For a pair of gears that mesh under a constant load and speed, one of which has z teeth and is rotating with frequency of f_r *Hz*, the fundamental meshing vibration is given by $f_m = zf_r$ *Hz*. The meshing vibration $x(t)$ may than be expressed as a sum of N harmonics, each of amplitude X_n:

$$x(t) = \sum_{n=0}^{N} X_n cos(2\pi n f_m t + \phi_n) \tag{4.1}$$

where ϕ_n is the phase angle of the n^{th} meshing harmonic. Assuming that the gear as a local defect such as a tooth fatigue crack, which effects the stiffness of the tooth and so produces changes in the vibration as the affected tooth meshes. These changes in vibration signal are defined by the amplitude and phase modulations [2]. Therefore the modulated gear meshing vibration $y(t)$ is given by:

$$y(t) = \sum_{n=0}^{N} X_n [1 + a_n(t)] cos[2\pi n f_m t + \phi_n + b_n(t)] \tag{4.2}$$

where $a_n(t)$ and $b_n(t)$ are the amplitude and phase modulations, respectively. As the

modulation functions are periodic with the gear shaft rotation, they may be expanded in Fourier series:

$$a_n(t) = \sum_{m=0}^{M} A_{nm} cos(2\pi m f_r t + \alpha_{nm}) \tag{4.3a}$$

$$b_m(t) = \sum_{m=0}^{M} B_{nm} cos(2\pi m f_r t + \beta_{nm}) \tag{4.3b}$$

The spectrum of $y(t)$ is composed by the fundamental frequency f_m and its harmonics surrounded by modulation sidebands. Both amplitude and phase modulation sidebands are spaced at intervals of the modulating function frequencies (e.g. f_r).

If there is a single frequency modulating function, such as the frequency rotation, amplitude modulation produces a single pair of sidebands, on the contrary, phase modulation produces a family of sidebands. Usually, in gears systems, there are both amplitude and phase modulation. Even though amplitude and phase modulation produce symmetrical families of sidebands when acting alone, the phase relationships on either side of the carrier frequency are different and the combination of the two families of sidebands can either reinforce or cancel. So, this results in an asymmetrical family of sidebands.

In order to better understand this phenomenon, the foregoing signal model is herein implemented in Matlab code. Three examples are subsequently show, which concerns a signal with only the fundamental frequency f_m with: amplitude modulation at frequency f_r (e.g. 1), phase modulation at frequency f_r (e.g. 2) and both amplitude and phase modulation at frequency f_r (e.g. 3). Data are listed in table 4.2.

Table 4.2: Vibration signal model of tooth fatigue crack: Matlab code data

	e.g. 1 Amplitude Modulation	e.g. 2 Phase Modulation	e.g. 3 Amplidute and Phase Modulations
$f_m[Hz]$	466.66	466.66	466.66
$f_r[Hz]$	8.4848	8.4848	8.4848
X_1	1	1	1
A_{11}	0.5	0	0.5
α_{11}	0	0	0
B_{11}	0	0.5	0.5
β_{11}	0	0	0

Examples one and two consist on amplitude and phase modulation respectively, only the first term of the right end side of equations (4.3a) and (4.3b) is considered. On second thought in the third example both amplitude and phase modulation are considered.

Figure 4.3 (a) and (b) show the time signal in case of amplitude and phase modulation respectively, whilst Figure 4.4 (a) and (b) plot the own spectrums. These figures highlight as previously said, which state that for an amplitude modulation only a pair of sidebands arise instead of a sideband family in case of phase modulation. In case of both amplitude and phase modulations, Figure 4.5, these sidebands are combined and they result in an asymmetrical family of sidebands.

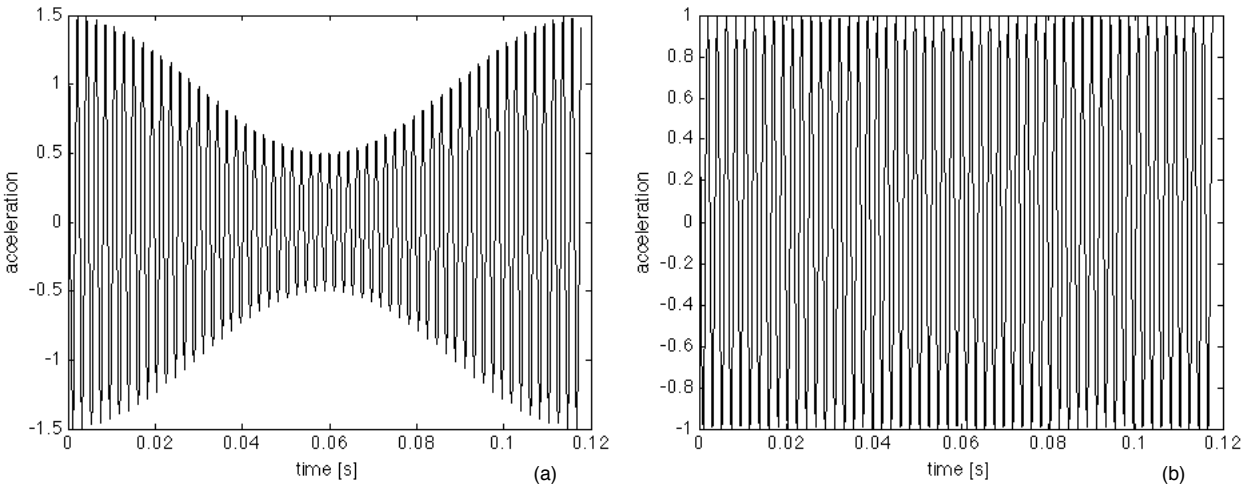

Figure 4.3: Signal model for a fatigue crack in gear tooth, time signal: (a) amplitude modulation and (b) phase modulation

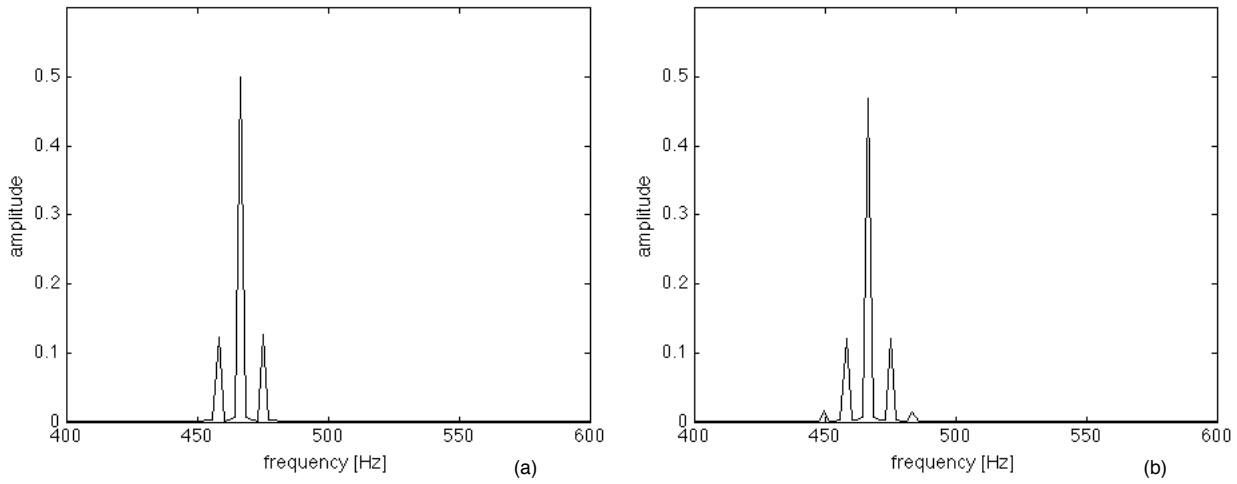

Figure 4.4: Signal model for a fatigue crack in gear tooth, FFT of time signal: (a) amplitude modulation and (b) phase modulation

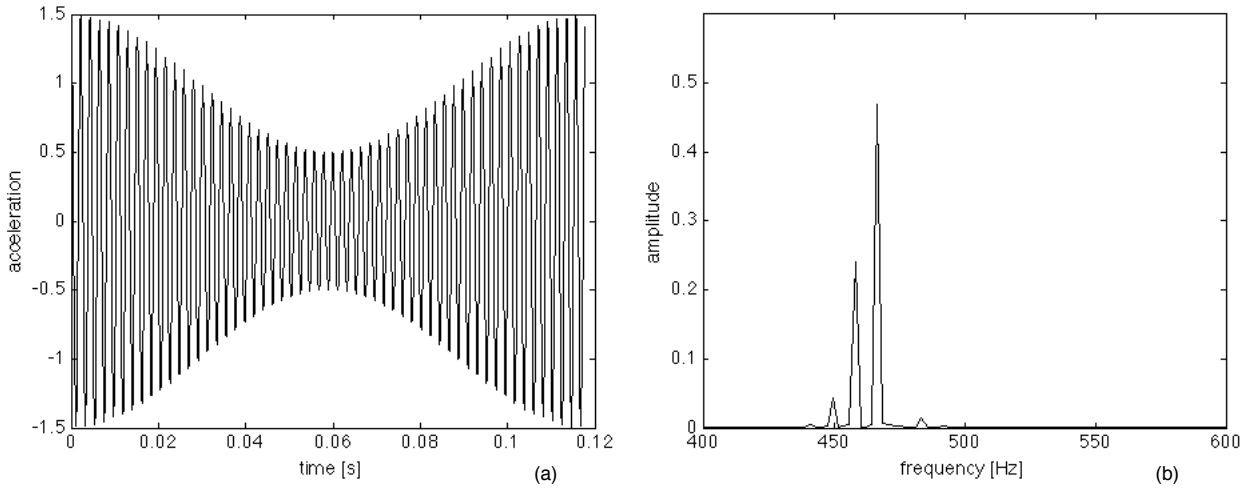

Figure 4.5: Signal model for a fatigue crack in gear tooth: (a) time signal with amplitude and phase modulations, (b) FFT of time signal with amplitude and phase modulations

4.2 Fatigue cracks: data analysis

The goal of this section is the analysis of fatigue crack in gear tooth. The former vibration signal processing techniques described in Chapter 2, i.e. continuous wavelet transform, Wigner-Ville distribution as well as techniques based on a cyclostationary signal model are applied to the gearbox vibration signals.

Two vibration velocity signals are take into account in this work. These signals are obtained via integration of the vibration acceleration signals measured form the casing of the damaged gearbox unit, by means of tho Brüel & Kjær 4369 piezoelectric accelerometers, more details on the acquisition data procedure can be found in [42]. The two accelerometers were mounted one, with the sensitivity axis parallel to the shaft axis ("axial" accelerometer), and the other close to the wheel bearing in a radial direction ("radial" accelerometer). In addition one-per-wheel revolution tachometer signal was taken using an inductive proximity probe.

Figure 4.6 shows the time-synchronous averages (TSA) of the four velocity vibration signals under consideration, namely the axial and radial vibration velocity for both crack lengths, which are computed over 28 wheel rotation (cracked gear). As one can see small alterations in vibration pattern can be noted in some of the experimental data, but this indication is not very clear, in addition no visible variations can be observed by comparing the small crack with the large one, for both axial and radial vibration velocities. The corresponding amplitude spectra are plotted in Figure 4.7 with a large-amplitude scale in order to better show sidebands. The analysis is limited to the wheel order range 0-500, which includes the most meaningful meshing harmonics. As expected, the fundamental and harmonic of the tooth meshing frequency dominate the spectra, moreover the family of the wheel sidebands appear very clearly in the spectra. Due to the strong influence of transfer function within meshing gear teeth and accelerometer positions, a different relative amplitude between harmonics for axial and radial vibrations can be noted.

The presence of sidebands at meshing harmonics is a consequence of a wheel tooth fault, but this type of analysis is insensitive to the damage severity. Therefore further

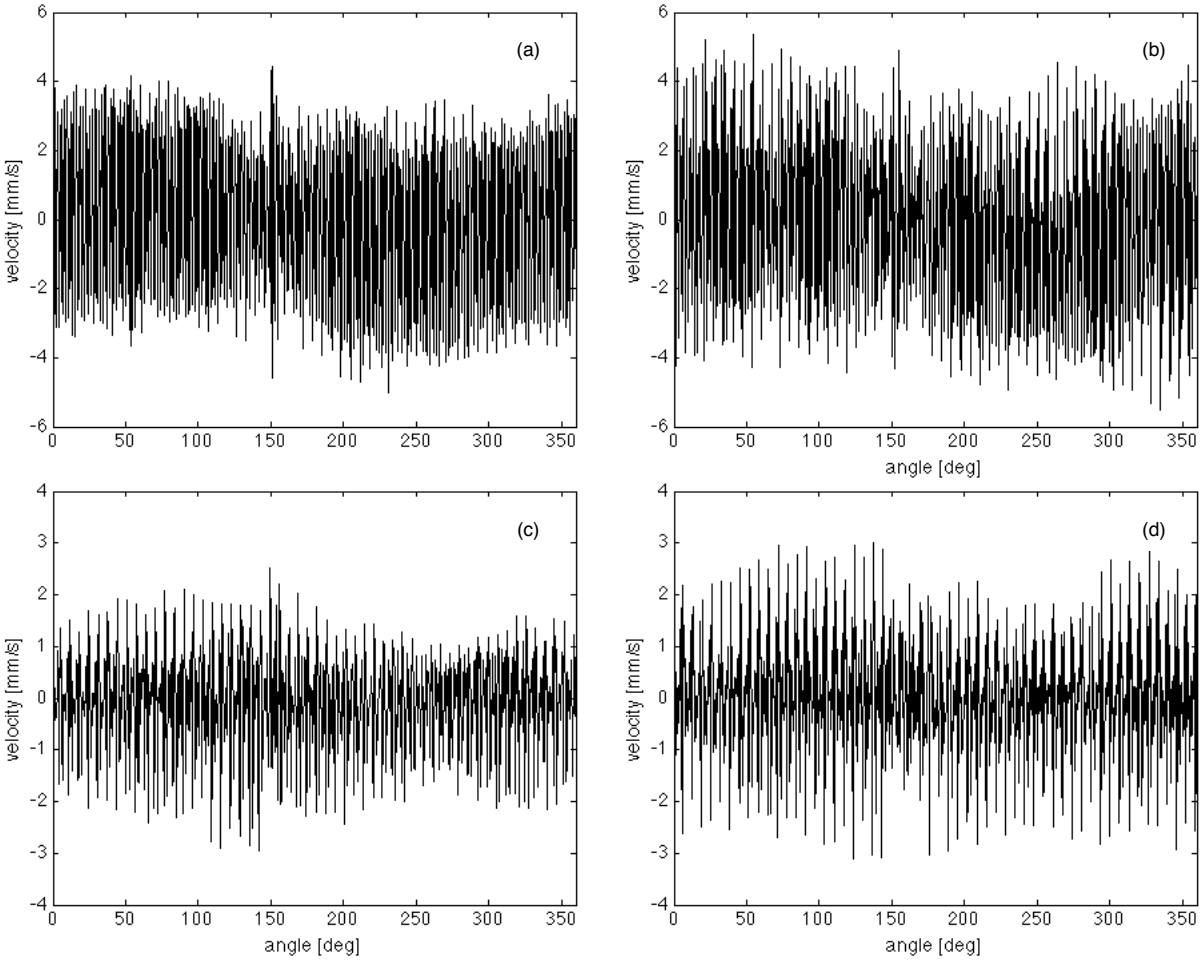

Figure 4.6: Time-synchronous average of the velocity signals. Axial vibration velocity: (a) small and (b) large cracks. Radial vibration velocity: (c) small and (d) large cracks

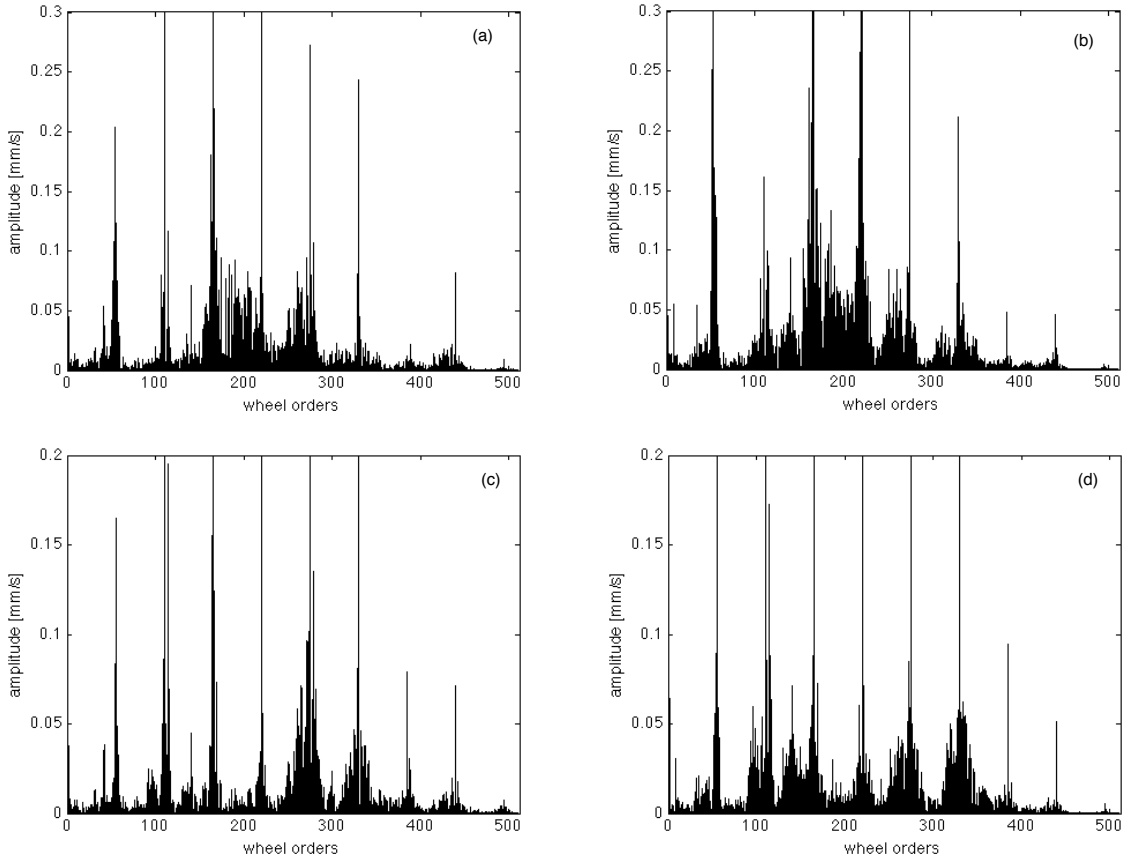

Figure 4.7: Amplitude spectrum of the time-synchronous average evaluated on one wheel rotations. Axial vibration velocity: (a) small and (b) large cracks. Radial vibration velocity: (c) small and (d) large cracks

investigation is needed.

In the following, time-frequency techniques, such as continuous wavelet transform (CWT) and Wigner-Ville distribution (WVD) are applied to the synchronized signals. The use of time-frequency techniques are suggested by the signal nature. As a matter of fact that the presence of local faults, such as a crack in one of the gear teeth, introduces short-duration changes in the vibration signal. Therefore the non-stationary signal characteristic can be well detected by time-frequency techniques.

In order to investigate the sensitivity of the method, the CWT was applied to the radial vibration signal in the case of small crack, because, as highlighted in [42] this signal seems to be scarcely affected by the fault.

Two types of mother wavelet are taken into account in this work, the Morlet and the Impulse mother wavelets. The reason of this choice is related to the nature of the signal. De facto, as previously said, the presence of local faults, such as a crack in one of the gear teeth, introduces short-duration changes in the vibration signal and so, the Impulse wavelet can be more sensitive to the fault localization whit respect to the Morelt one. Morlet wavelet is chosen as comparison parameter, because of the large use in literature of this type mother wavelet for gear fault diagnosis procedures [46, 47].

The changes in the vibration signal due to the cracked tooth take-over, causes an increment of the CWT amplitude of short-duration over a wide frequency range. Therefore, the fault location can be pointed out by an abrupt time-change in the CWT amplitude map.

The CWT of the TSA is computed using both Morlet and Impulse mother wavelets and the nalysis is carried out in a 50-400 wheel order band, which includes the most important meshing harmonics. Figure 4.8 (a) and (b) shows the results of this analysis. A slightly change in the CWT map can be noted for Morlet mother wavelet (Figure 4.8 (a)), at about 150° nearby the 270^{th} wheel order, whilst this transition becomes evident in case of Impulse mother wavelet (Figure 4.8 (b)). Moreover the Impulse mother wavelet is able to show the fundamental meshing frequency and its harmonics, at 55^{th}, 110^{th} and 165^{th} wheel orders.

As explained in [42], the presence and the location of the faulted tooth can be obtained by a careful inspection of the CWT cross-section. As plotted in Figures 4.9 and 4.10, it is possible to clearly distinguish the transient effects introduced by the cracked tooth, at about $150°$.

Therefore, the foreign analysis shows that the choice of the analyzing mother wavelet plays a pivotal role in the detection of transient faults. In particular, by the use of an Impulse mother wavelet, local faults that introduce small transient events in the vibration signal, can be well detected. Moreover the analysis of the CWT cross-section is helpful in the vibration based diagnostic procedures.

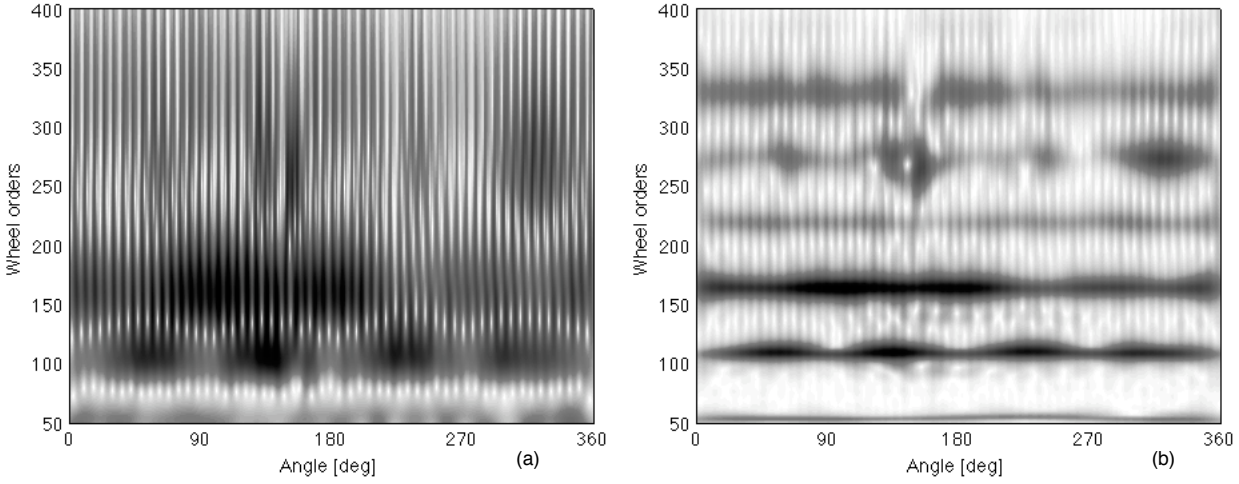

Figure 4.8: Continuous wavelet transform of the time-synchronous-averaged radial vibration velocity in the case of small crack: (a) Morlet mother wavelet, (b) Impulse mother wavelet

The CWT map is followed compared to the Wigner-Ville distribution of the time-shynchronous average, Figure 4.11.

Several horizontal dashed lines are present in the WVD, some of them are related to the harmonics of the fundamental meshing frequency, i.e. 110^{th}, 165^{th}, 220^{th} and 255^{th} wheel order, the others are cross-terms that are due to the non-linear behavior of the transformation. Moreover this energy distribution does not clearly reveal the presence of the defect.

As explained in Chapter 2, these cross-terms can be removed by the combination of the WV with the Fourier-Bessel (FB) series expansion, which decomposes the multi-

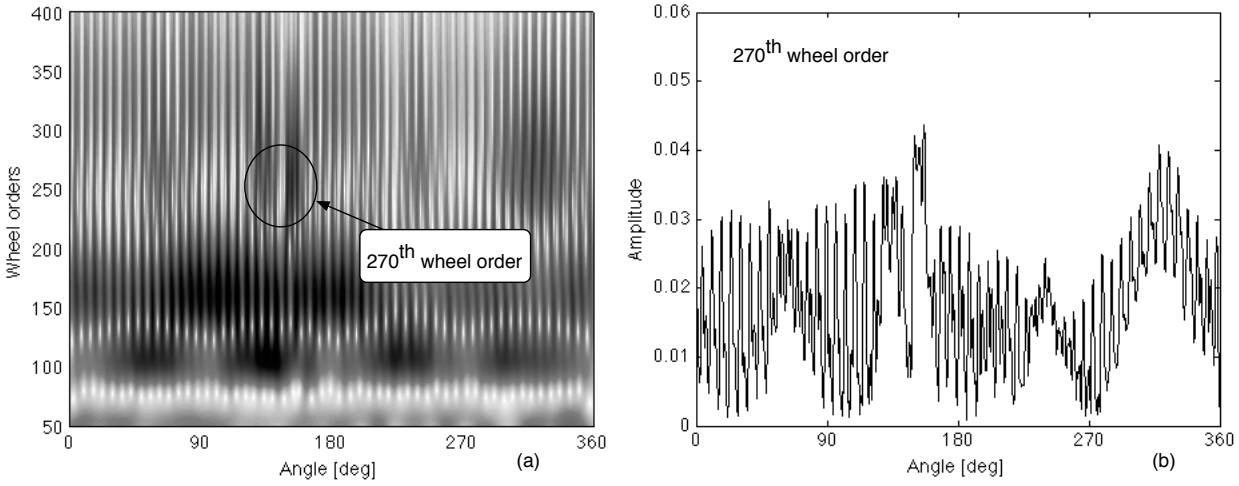

Figure 4.9: Continuous wavelet transform of the time-synchronous-averaged radial vibration velocity in the case of small crack: (a) Morlet mother wavelet, (b) corresponding cross section at 270^{th} wheel order

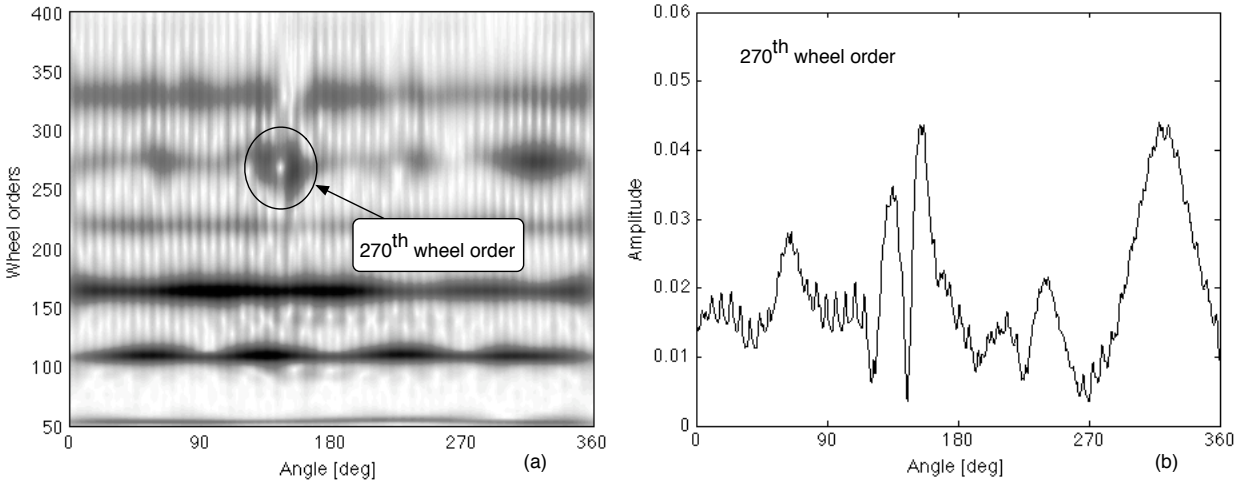

Figure 4.10: Continuous wavelet transform of the time-synchronous-averaged radial vibration velocity in the case of small crack: (a) Impulse mother wavelet, (b) corresponding cross section at 270^{th} wheel order

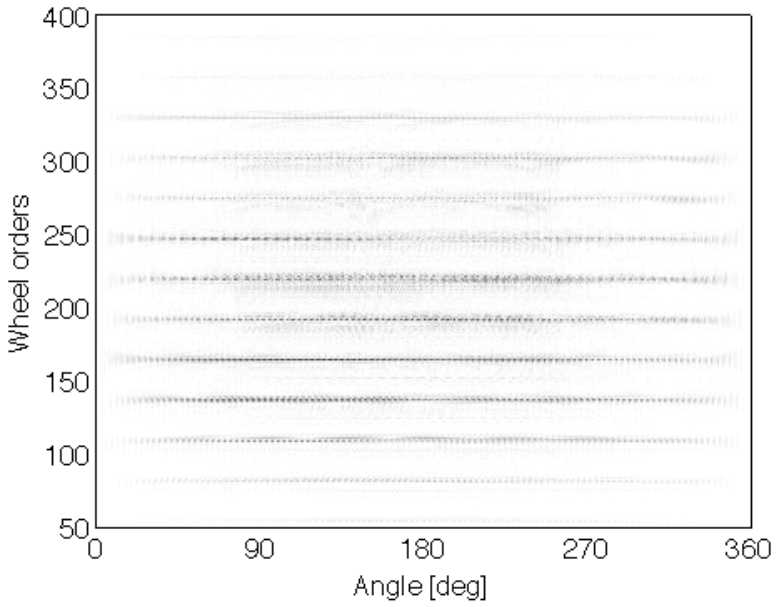

Figure 4.11: Wigner-Ville distribution of the time-synchronous-averaged radial vibration velocity in the case of small crack

component input signal into its constituents.

The signal is firstly decomposed in its fundamental components and than the WVD of each component is evaluated and the total WVD is obtained by the summation of the partial WVD.

Figure 4.12 depicts the Fourier-Bessel series coefficient. By this plot one can see the meshing frequency and its fundamental harmonics, which are depicted by the seven clusters in the FB coefficient plot. In addition this plot confirm the presence of the tooth fault, in fact each of this clusters is composed by a distinct oscillation surrounded by several neighboring components. Each of these seven main oscillation is a sinusoidal component, which are the fundamental meshing frequency and its harmonics respectively. The other neighbouring components composing the clusters are due to the amplitude and phase modulations.

Figure 4.13 plots the WVD of the signal decomposed into Fourier-Bessel series expansion. As one can see, this energy distribution is unaffected by cross-terms. Moreover the meshing frequency harmonics are clearly depicted, and a localized increment of the WVD amplitude is visible at the 275^{th} wheel order, at about 150 degrees.

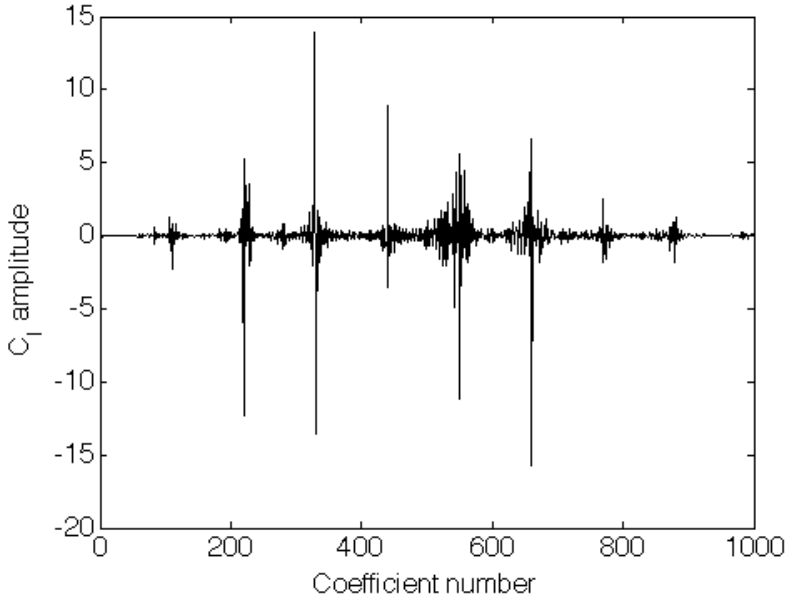

Figure 4.12: Fourier-Bessel of the time-synchronous-averaged radial vibration velocity

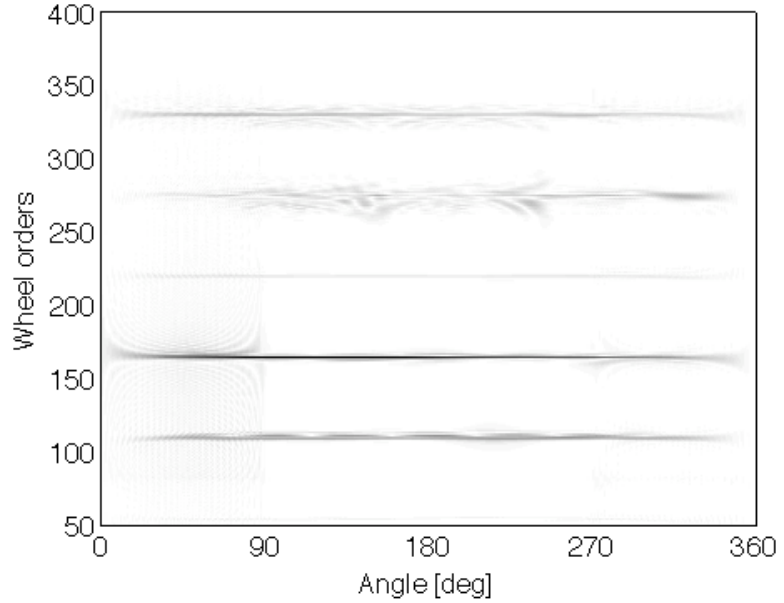

Figure 4.13: Wigner-Ville distribution of the time-synchronous-averaged radial vibration velocity after the Fourier-Bessel signal decomposition

However the transient event occurring in the WVD amplitude at the 5^{th} meshing harmonic is not enough for the complete fault detection. So, in order to look for local alterations, one can observe the fundamental signal component obtained from the FB series decompositions, which contains informations about the amplitude alteration in the reconstructed WVD. As described in [42], by analyzing the phase modulation

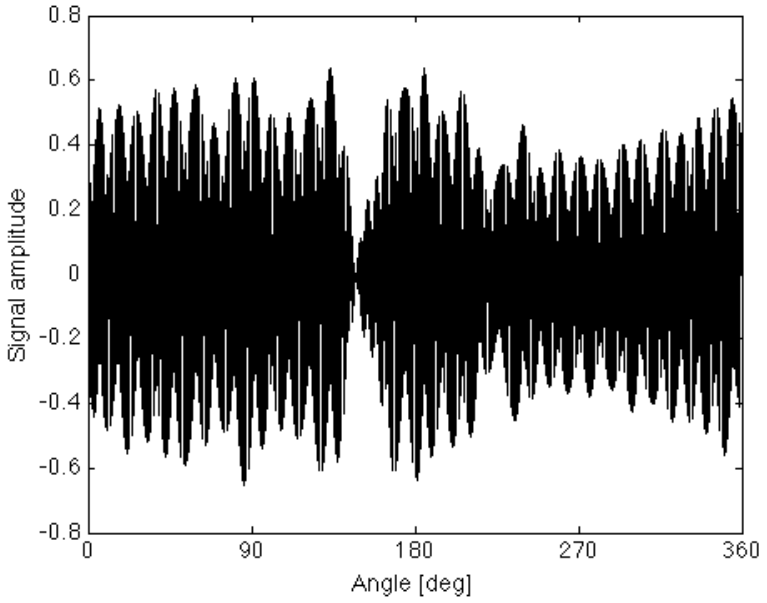

Figure 4.14: 5^{th} meshing harmonic reconstructed from Fourier-Bessel series expansion of the time-synchronous-averaged radial vibration velocity

of the time-synchronous-averaged radial vibration velocity, the 5^{th} meshing harmonic was the most sensitive to the local defect. In fact (see Figure 4.14), the 5^{th} meshing harmonic extracted from the time-synchronous-averaged radial vibration velocity, via FB decomposition, give rise to an abrupt fall at about 150 degrees, which correspond to the cracked tooth engagement.

Therefore, the WVD is inadequate for the fault localization in vibration signal composed of several strong harmonic components, due to the cross-terms that limit the usefulness of the representation. However, this difficulty can be overcome by the FB decomposition of the input signal.

Finally, the Spectral Correlation Density (SCD) function is considered. As a first measure of the existence of cyclostationary components in a signal, the degree of cy-

clostationarity (DCS) function of the signal can be used, which shows the degree of cyclostationarity of a given frequency α. A further advantage of the DCS function raises from the fact that it presents a non-dimensional quantity, which can be used more effectively for fault trend analysis, especially in case of bearing fault diagnosis [5]. Figures 4.15 and 4.16 plot the DCS for axial and radial vibration velocities for both small and large cracks, which are characterized by the presence of a number of non-zero cycle frequencies. In particular the DCS functions over the $0 \div 150$ frequency band show several non-zero cycle frequencies corresponding to the wheel rotation frequency and its harmonics for both axial and radial vibration velocities (Figures 4.15 and 4.16 (*a*) and (*b*)). This provides a first indication that a modulation effect is present in the signals. Moreover, by looking the DCS function in a wide frequency band, i.e. $0 \div 4000$ *Hz*, several non-zero cycle frequency arise at the meshing frequency harmonics, as well as at cycle frequencies relating to the correlation among them (Figures 4.15 and 4.16 (*c*) and (*d*)). The SCD functions of both small and large cracks are computed over the synchronously resampled signals, in order to eliminate speed irregularities. In this analysis the SCD function is evaluated via Fourier series expansion of the WVD. In order to reduce noisy components in the SCD plot, the signal is synchronously averaged. The time synchronous average is performed over four wheel rotations in order to obtain a cycle frequency resolution of 2.12 *Hz*. Figures 4.17 and 4.18 plot the SCD magnitude of the bifrequency plane (*f*, α), using a three-dimensional diagram, in which only the positive quadrant of the diagram is considered. In depth, for axial vibration velocities the relationships among the third meshing harmonic and its first upper modulating sidebands relative to both the pinion and the wheel are investigated, whilst for radial vibration velocities the links among the fifth meshing frequency harmonic and its lower modulating sidebands relative to both the pinion and the wheel are taken into account. Whereupon, the SCD

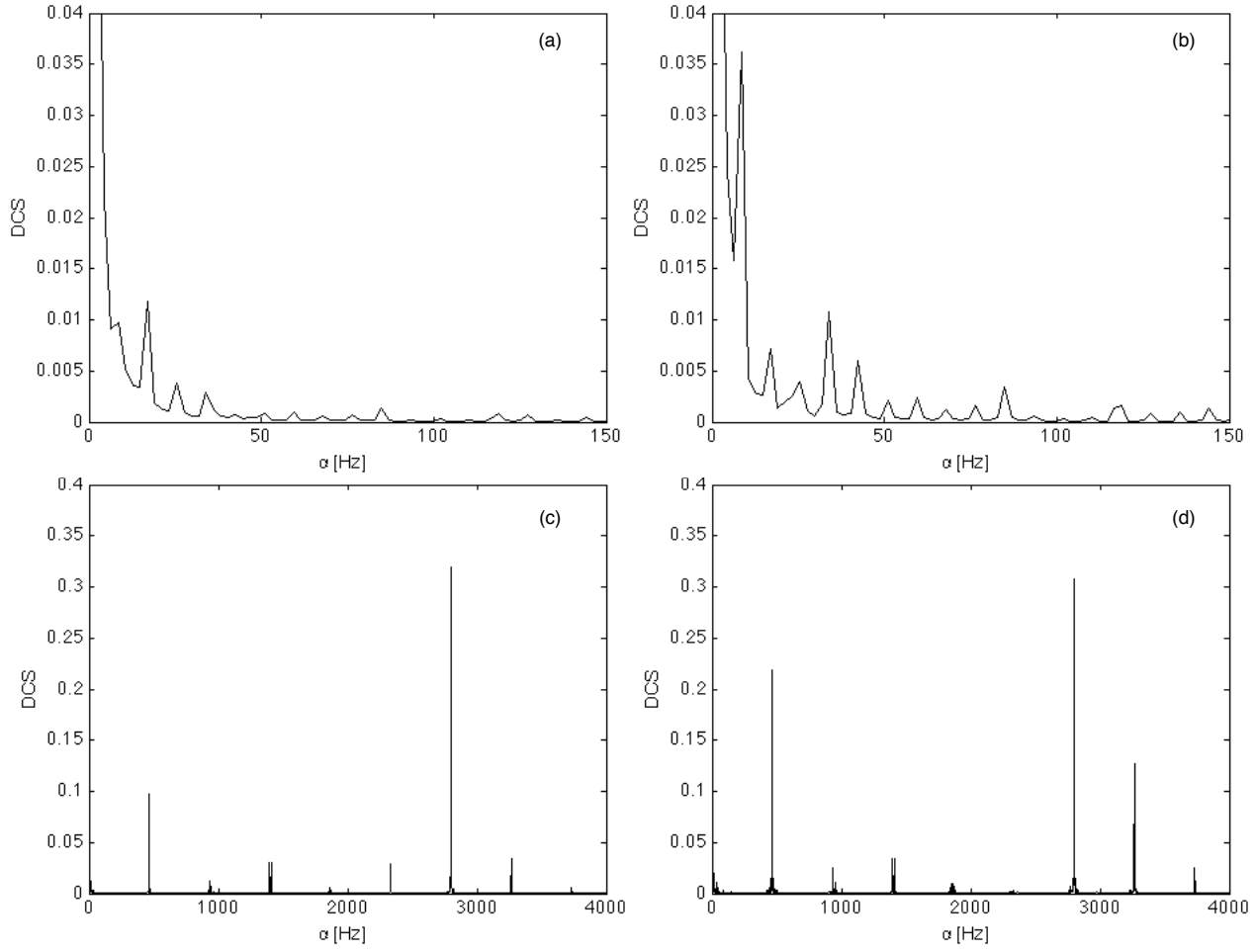

Figure 4.15: Axial vibration velocity: DCS in the $0 \div 150$ frequency band for (a) small and (b) large cracks; DCS in the $0 \div 4000$ frequency band for (c) small and (d) large cracks

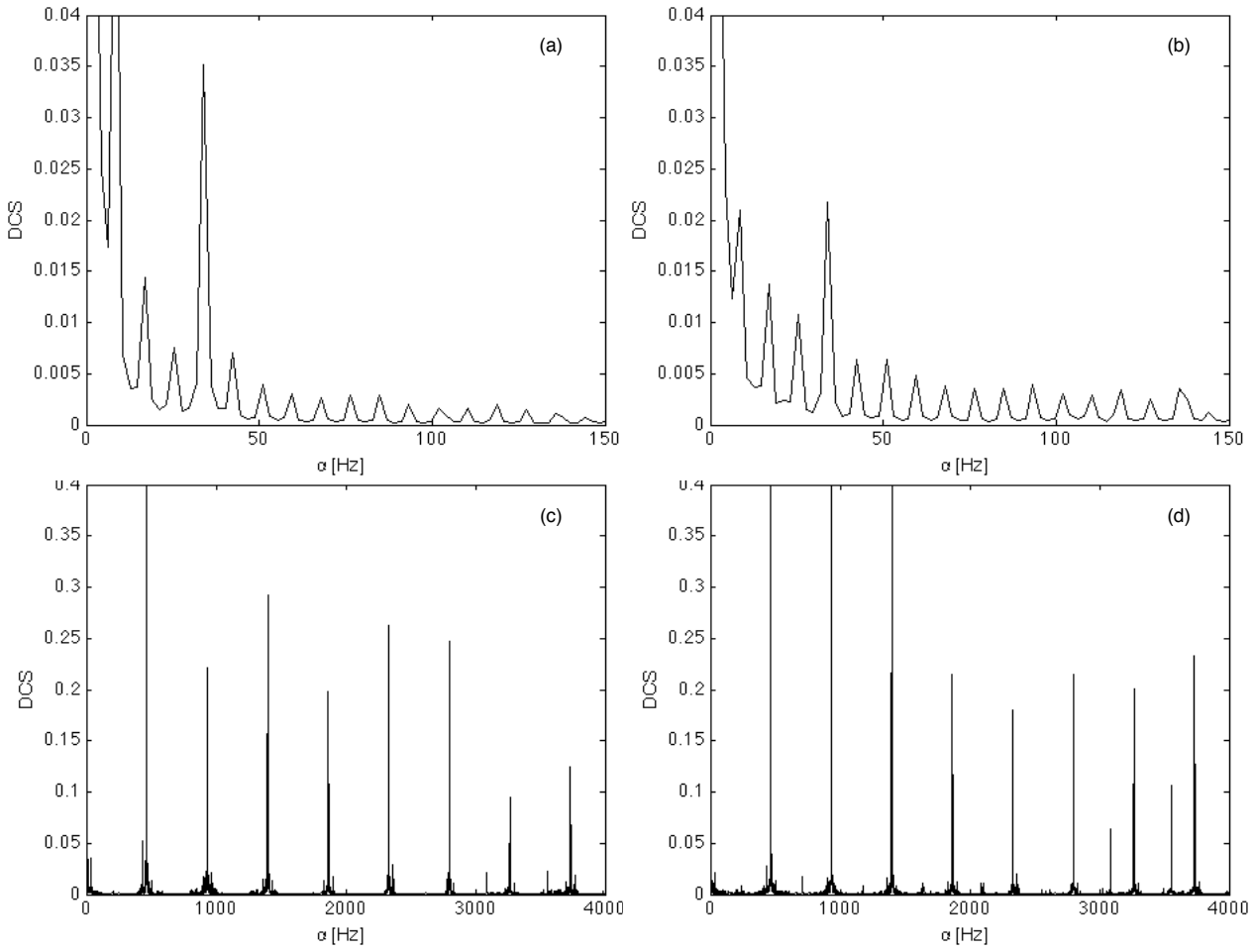

Figure 4.16: Radial vibration velocity: DCS in the $0 \div 150$ frequency band for (a) small and (b) large cracks; DCS in the $0 \div 4000$ frequency band for (c) small and (d) large cracks

components (f,α) considered in this analysis are the follows:

Axial vibration velocities

$$\left.\begin{array}{ll} \text{third meshing frequency harmonic} & 1400Hz \\ \text{first upper modulating sidebands relative to the wheel} & 1408.4Hz \end{array}\right\} \Rightarrow (1404.2, 8.4)$$

$$\left.\begin{array}{ll} \text{third meshing frequency harmonic} & 1400Hz \\ \text{first upper modulating sidebands relative to the pinion} & 1417Hz \end{array}\right\} \Rightarrow (1408.4, 16.8)$$

Radial vibration velocities

$$\left.\begin{array}{ll} \text{fifth meshing frequency harmonic} & 2333Hz \\ \text{first lower modulating sidebands relative to the wheel} & 2342Hz \end{array}\right\} \Rightarrow (2329.8, 8.4)$$

$$\left.\begin{array}{ll} \text{fifth meshing frequency harmonic} & 2333Hz \\ \text{first upper modulating sidebands relative to the pinion} & 2348.8Hz \end{array}\right\} \Rightarrow (2341, 16.8)$$

Data cursors depict the amplitude and the location in the bifrequency plane of the foreign components.

As one can see from Figures 4.17 and 4.18 peaks that correspond to the wheel shows an increment with the crack severity, whilst the pinion correlation peak only exhibits slight changes. These changes are related to the different tests conditions

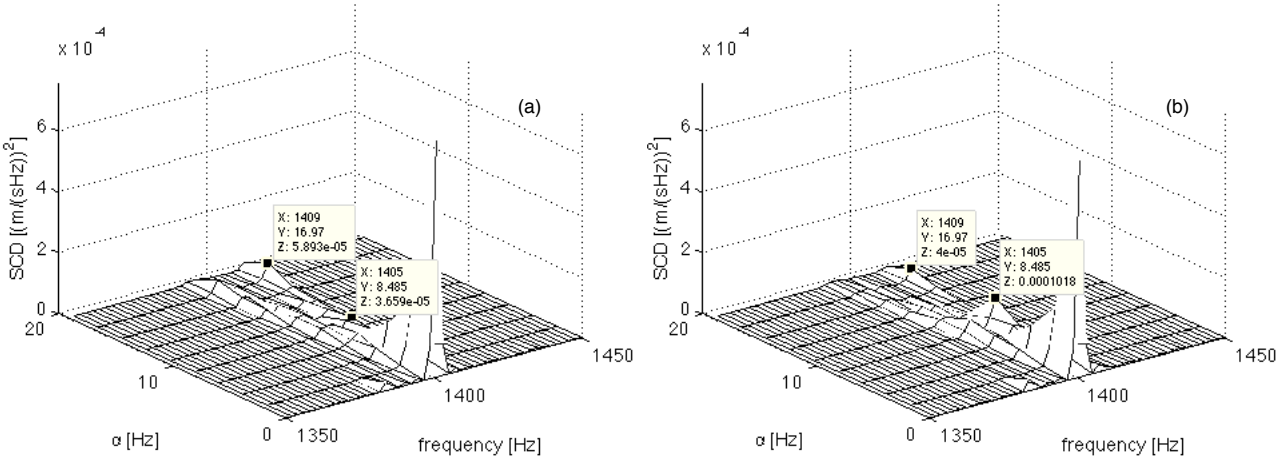

Figure 4.17: Spectral correlation density function among the third meshing harmonic and its sidebands. Axial vibration velocity: (a) small and (b) large cracks

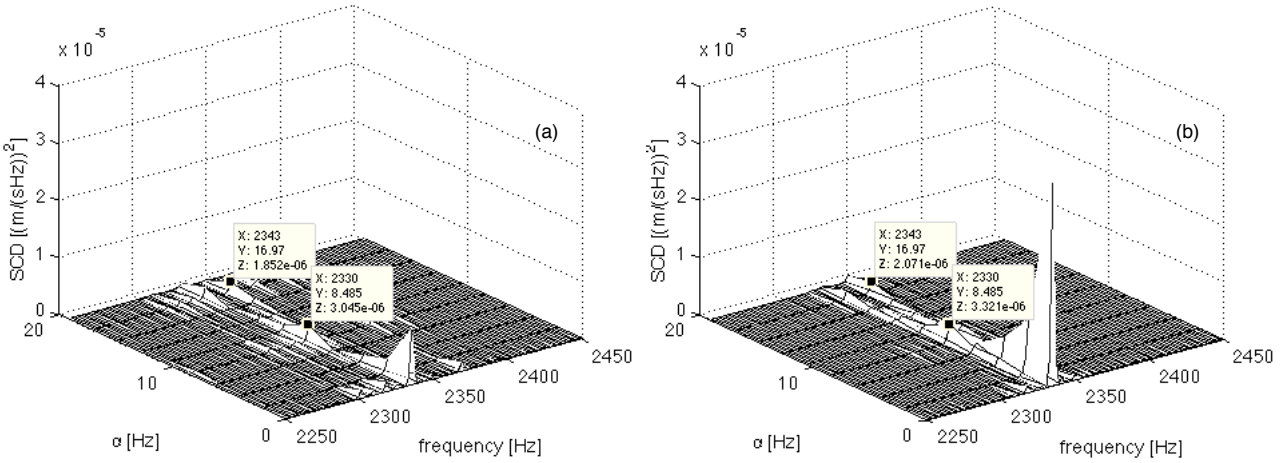

Figure 4.18: Spectral correlation density function among the fifth meshing harmonic and its sidebands. Radial vibration velocity: (a) small and (b) large cracks

4.3 Tooth spalls: experimental apparatus

The effects of tooth spalls on gear vibrations are investigated with an “experimental model” designed and build up at the Engineering Department of the Univerity of Ferrara. This test bench was developed as a tool for the experimental analysis of the vibro-acoustical behaviour of rotating machineries and the investigation of the vibration effects both in sound and faulty conditions, further details about the test bench can be found in [48].

The test bench consists of a base, including an induction driving motor controlled by inverter, and three different rotor kits. These kits are designed in order to carry out a great number of experiments concerning the vibrations produced by gears and rolling bearings in sound conditions and with different types of faults, as well as misalignments between shafts, static and dynamic unbalance and critical speeds.

In this work only the first kit is taken into account, and it deals with two induction motors controlled by inverters and a gear unit (Figure 4.19). The layout of the kit is depicted in Figure 4.20. In more detail, the driving induction motor BN80C2 is controlled in a feedback speed loop by the inverter ACT400-014; its speed is evaluated by an encoder with 360 pulses per revolution. The induction motor BN132MB4 is used to apply the load and is controlled in a feedback torque loop by the inverter ACT400-040, while the speed is evaluated by an encoder with 3600 pulses per revolution. Table 4.3 lists the data of the induction motors. The gear unit C312 contains two spur gear pairs, one having 18 and 71 teeth, the other one 12 and 55 teeth, for a global speed reduction ratio of 18.1. The connection among the induction motor shafts and the gear unit shafts is performed by Giflex elastic joints, allowing parallel and angular misalignments between shafts. In addition an auxiliary fan is mounted on the load motor in order to avoid the overheating condition due to its work at low speed and high torque.

As explained before gear tooth spalls are mechanically introduced on the first stage wheel (71 teeth) of the gearbox, via a drilling process.

During tests the vibration signal is acquired by means of a PCB piezoelectric ac-

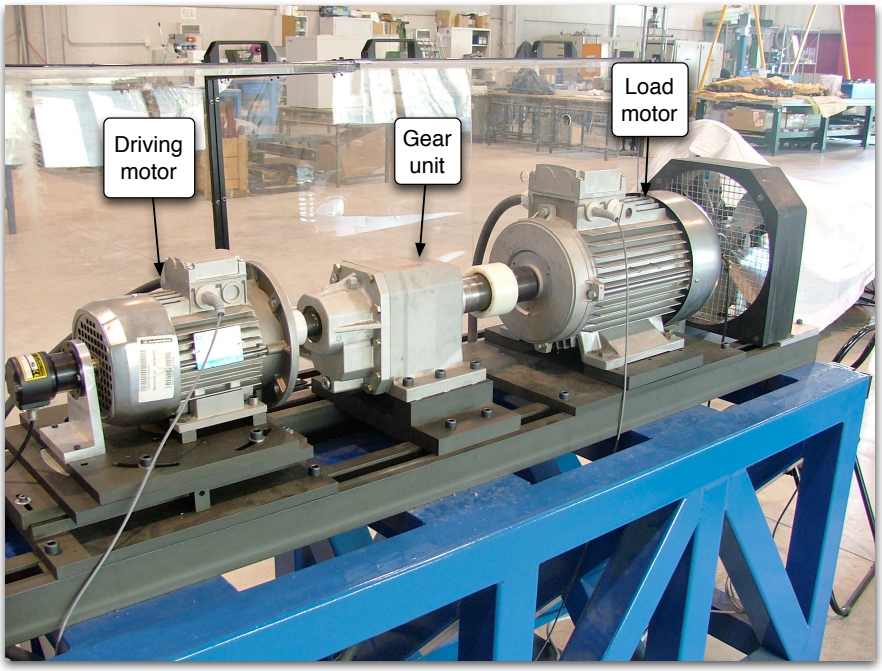

Figure 4.19: Test bench for gear tooth spall experiments

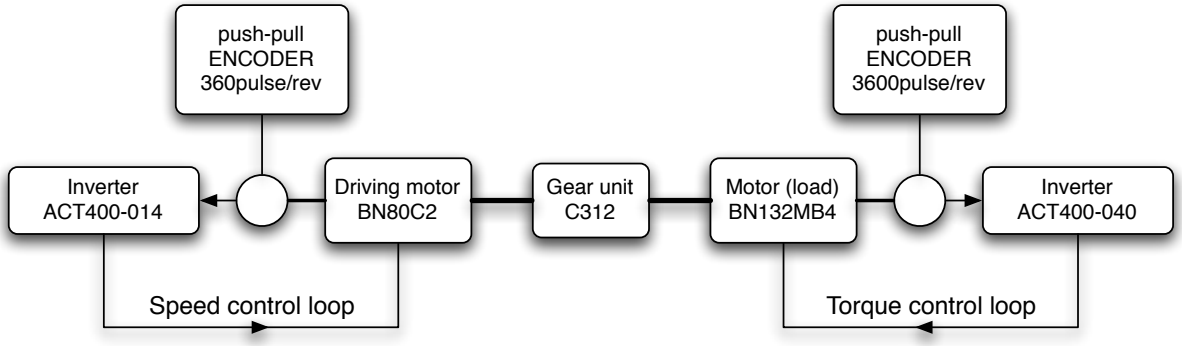

Figure 4.20: Kit for tests on gear tooth spall vibrations: layout

Table 4.3: Induction motor date

	BN80C2	BN132MB4
Nominal power $[kW]$	1.5	9.2
Nominal torque $[Nm]$	5.1	61
Nominal speed $[rpm]$	2800	1440
Number of poles per phase winding	2	4

celerometer mounted in radial direction nearby bearing support of the first stage pinion. The results presented in this work are relative to a nominal driving motor speed of 3600 *rpm* (60 *Hz*) and nominal torque of 48.8 *Nm*, with a sample frequency of 104.2 *KHz* to an extent of 50 *s*.

The signals were acquired using LMS SCADAS 310 front-end and controlled by the software LMS Test.Lab.

4.4 Tooth spalls: vibration signal model

This section concerns the explanation of the main vibration phenomena in gear system due to the presence of a spall in a gear tooth. One can think that, this vibration signal model is likely the same as the previous one. However this assumption is not completely true. In fact, as explained by Randall in [49], this type of fault give rise to components over a wide frequency range. Components are due to amplitude and frequency modulation which cause sidebands at the gear meshing frequency and in addition additive impulses, which arise one time per revolution and can excite gearbox resonances. Therefore the vibration signal can be described as a sum of N harmonic components such as:

$$y(t) = \sum_{n=0}^{N} \left[X_n[1 + a_n(t)]cos[2\pi n f_m t + \phi_n + b_n(t)] + e^{-t_n/\sigma_{imp}} X_{imp} cos(2\pi f_{imp} t) \right] \quad (4.4)$$

where X_n is the amplitude of each harmonic, X_{imp}, σ_{imp} and f_{imp} are respectively the amplitude, damping coefficient and carrier frequency of the impulse response, whilst $a_n(t)$ and $b_n(t)$ are respectively the amplitude and phase modulating functions:

$$a(t) = Ae^{-\frac{(t-t_0)^2}{\sigma^2}} \quad (4.5a)$$

$$b(t) = Be^{-\frac{(t-t_0)^2}{\sigma^2}} \quad (4.5b)$$

These functions describe the local change of the meshing vibration due to the engagement of the faulted tooth. The parameter σ is related to the width of the Gaussian shape windows. Moreover, going deeply through the phenomena that arise during

the engagement of the faulted tooth, one can notice that for narrow spall sizes only a small portion of the contact is affected by the fault presence. Whereas, the contact is entirely affects by the fault, in the case of broad spall sizes, Figure 4.21. These differences change the impulsive contents of the vibration signal. In fact, for the smallest spall sizes a strong impulsive component arises which give up to an higher frequency content, due to the excitation of gearbox natural frequencies. On the contrary, for the wider spall sizes, the impulsive signal content is smoothed. This behavior can be well described by the SCD function.

In order to better understand this phenomenon, the foregoing signal model is herein implemented in Matlab code. Two examples are subsequently show, which concerns two signal with: fundamental frequency f_m, amplitude and frequency modulation at frequency f_r, high damped impulse response (e.g. 1.) and low damped impulse response (e.g.2). Data are listed in table 4.4.

Table 4.4: Vibration signal model of tooth spall: Matlab code data

	e.g.1	e.g.2
f_m [Hz]	534.5	534.5
f_r [Hz]	8.4848	8.4848
f_{imp} [Hz]	3800	3800
A	0.2	0.2
B	0.2	0.2
σ	10	10
σ_{imp}	10	40

Figure 4.22 shows the amplitude signal for a portion of the shaft rotation. In particular is highlighted the effect on the vibration signal due to the engagement of the faulted tooth. It possible to notice that a local alteration in the vibration signal is obtained by the uses of equations 4.5a and 4.5b, moreover an impulsive component is added during the meshing of the faulted tooth. Figure 4.23 plots the SCD in the positive region of the bifrequency plane in case of: (a) large spall size and (b) narrow spall size. In Figure 4.23 (b) it is possible to notice the comparison of an higher frequency content due to the low damped impulse response.

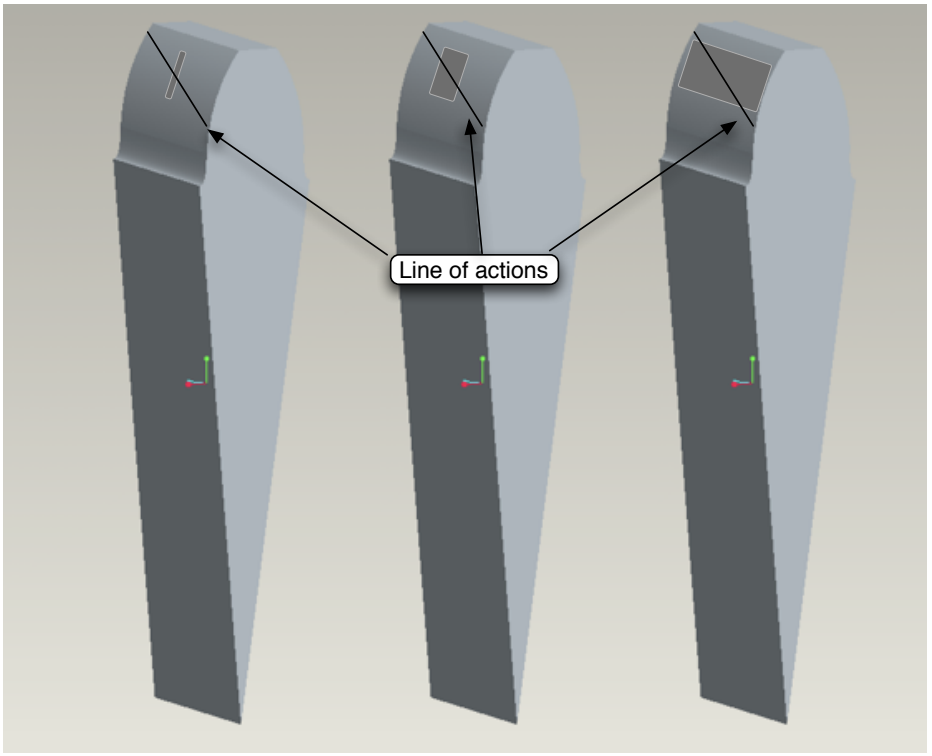

Figure 4.21: Gear tooth spalls: comparison among differt spall sizes and contact line

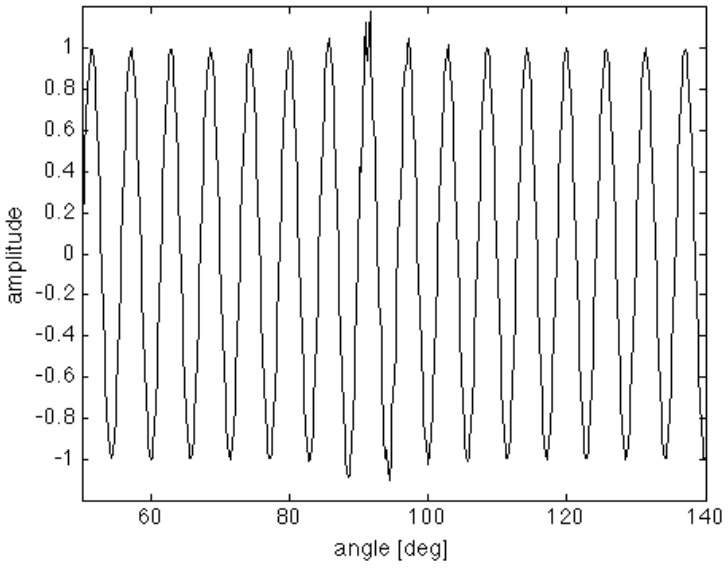

Figure 4.22: Vibration signal model for gear tooth spall: time signal

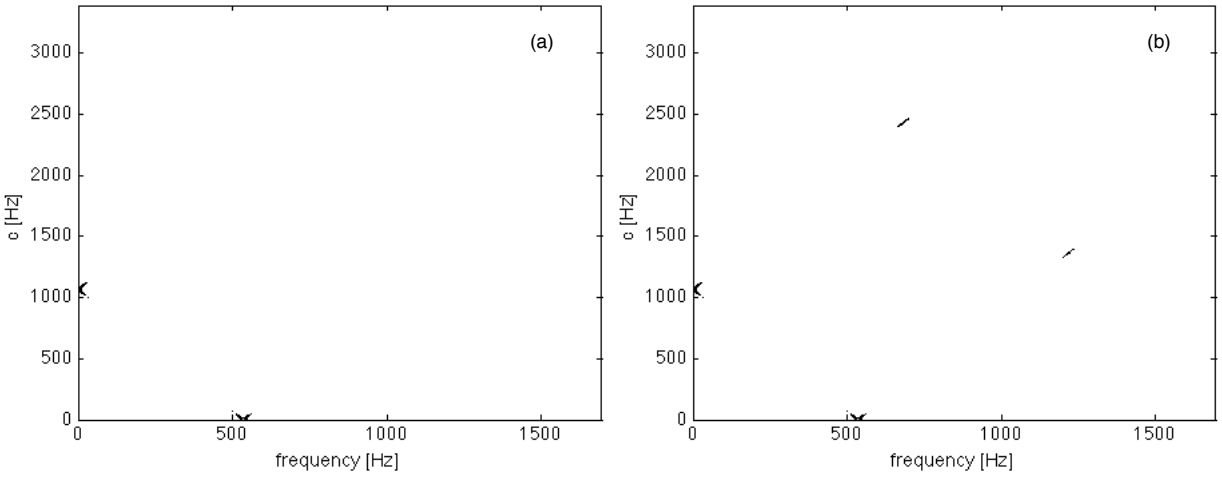

Figure 4.23: Vibration signal model for gear tooth spall, SCD contour plot: (*a*) large spall size and (*b*) narrow spall size

4.5 Tooth spalls: data analysis

The aim of this section is the analysis of spalls in gear tooth. As previously said, in this work different spall sizes are investigated, which are listed in table 4.1.

First of all, the acceleration signal acquired from the gearbox is synchronously re-sampled, with 1024 points per wheel revolution, and the time-synchronous average is computed over 200 wheel revolutions. The results are plotted in Figure 4.24. No evident alteration in the vibration patterns can be noted for the smallest spall sizes, whilst for the Sp50% and Sp100% an high-amplitude transient vibration can be noted during the engagement of the faulted tooth. In fact, the vibration signatures seem to be bounded in the range $-4 \div 4\, m/s^2$, whilst the engagement of faulted tooth yields a transient vibration pattern up to $-7 \div 7\, m/s^2$ (see Figure 4.24 (e) and (f)). By the comparison between Figure 4.24 (e) and (f) it is possible to notice that, this transient vibration occurs at a different angle position. This is due to the different angular position of the faulted tooth with respect the one-per-wheel revolution tachometer reference. The corresponding amplitude spectra are plotted in Figure 4.25, in the 50-250 wheel order band, which include the most important meshing harmonics. In particular, the gear meshing frequency (71^{th} order) dominates the spectra. In all cases

the fundamental meshing frequency is the highest one. Several wheel sidebands appear in the spectra. De facto these sidebands are not only generated by spalls, but also from misalignments arise during the gearbox reassembly operations. Nevertheless, by looking through a frequency band around the gear meshing frequency, which is depicted in Figure 4.26, it can be noted that the amplitude of the first upper sidebands of the meshing frequency increase with the spall dimensions, while the amplitude of the first lower sidebands of the meshing frequency do not shown any clear-cut course. Therefore, this behavior can be described by relating the first upper sidebands to spalls and the lower sidebends to misalignments. In fact, due to the gearbox reassembly operations, the wheel misalignments are different for every tooth spall dimensions. Ergo, in this case, the FFT analysis seems to be practically ineffective for spalls detection and so further investigations are needed.

Consequently the demodulation technique is applied to synchronized signals of Figure 4.24, via filtering around the fundamental meshing frequency (71^{th} order), which seems to show the strongest modulation sidebands. In more detail 72 sidebands around the meshing frequency are considered in the analysis. The amplitude modulation (AM) of the vibration signals are shown in Figure 4.27. As one can see, the amplitude modulation can localize the damaged tooth only in the cases of Sp50% and Sp100%, whose engagement is characterized by a maximum value of the AM function. Whilst for the smaller spall sizes, the AM seems to be insensitive to fault detections. As shown in [42], the AM technique is strongly influenced by the processed frequency band. Therefore, different bands are taken into account in order to improve the technique sensitivity.

Figure 4.28 shows the AM concerning 31 upper sideband around the meshing frequency, for Sp12.5% and Sp25%, which seem to be related to the tooth spalls. In fact lower sidebands could be related to the wheel misalignments and so can cause poor results. Unfortunately the faulted tooth still non-localized, because of significant changes in he AM functions of Figure 4.28 are not detected. So, this analysis confirm the insensitiveness of AM technique to fault detections in the case of small spall sizes. Concluding, the demodulation technique gives good results only in the case of large

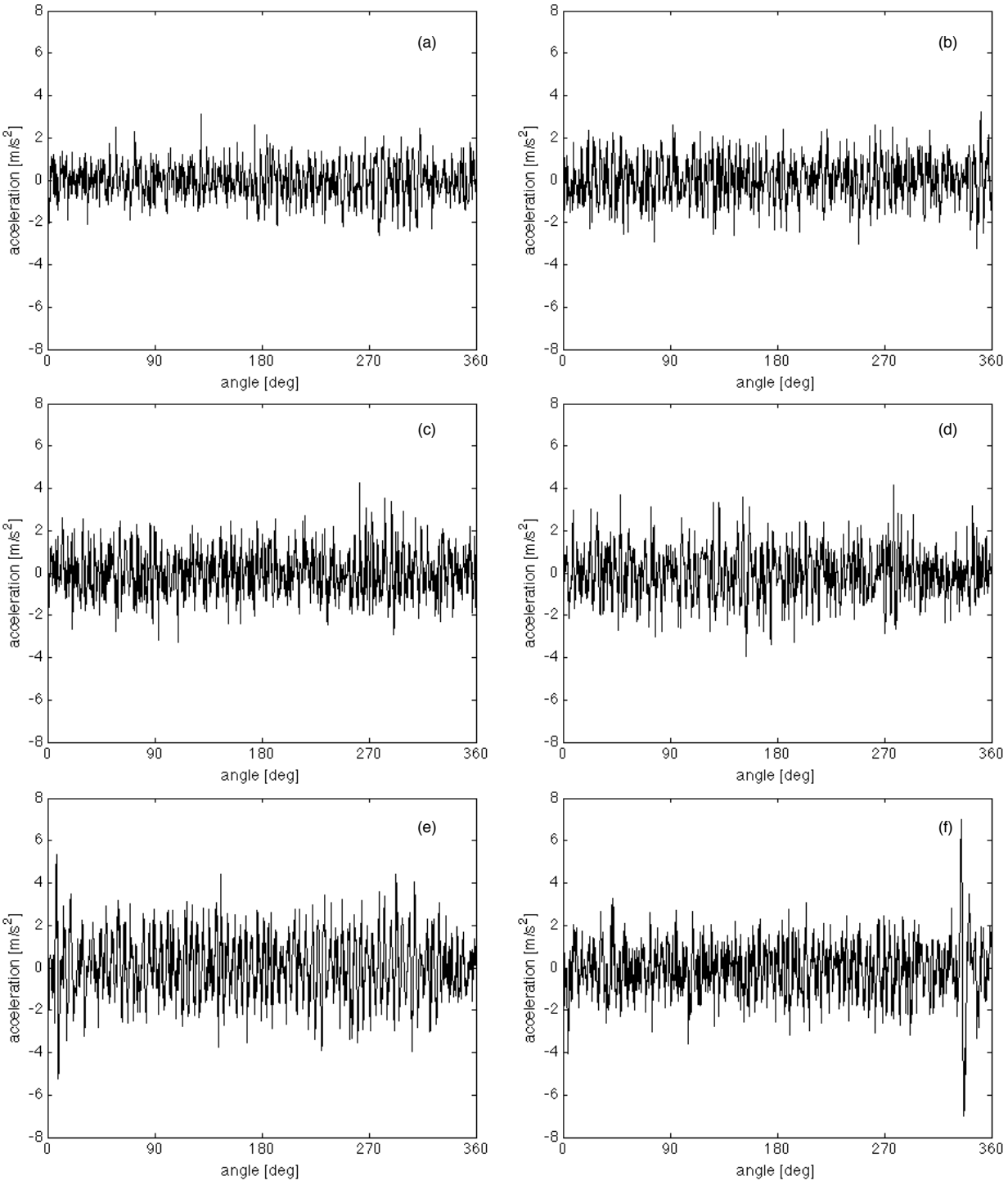

Figure 4.24: Time-synchronous average of the acceleration signals: (a) sound gear, (b) Smack, (c) Sp12.5%, (d) Sp25%, (e) Sp50%, (f) Sp100%

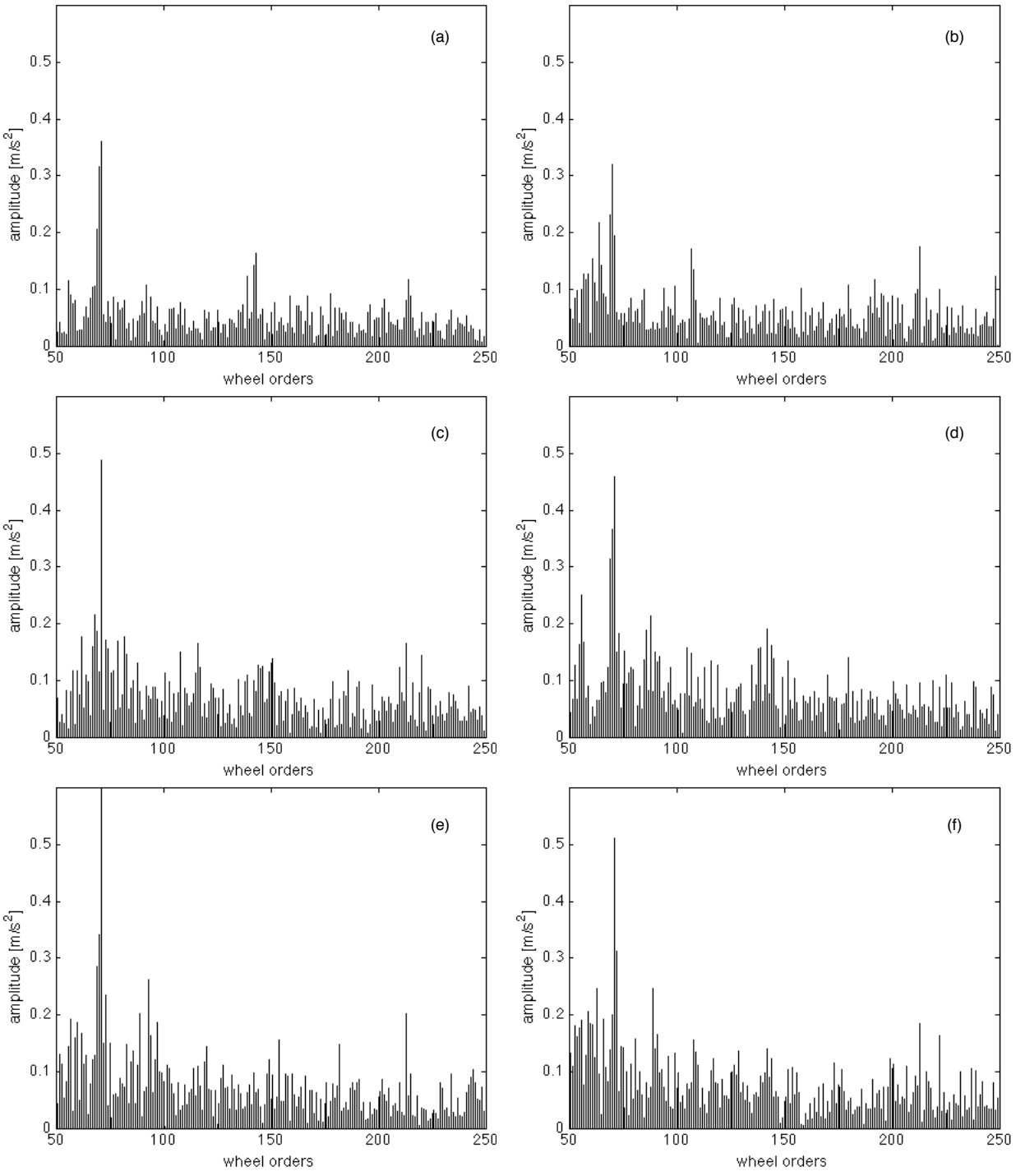

Figure 4.25: FFT of the time-synchronous average of the acceleration signals: (a) sound gear, (b) Smack, (c) Sp12.5%, (d) Sp25%, (e) Sp50%, (f) Sp100%

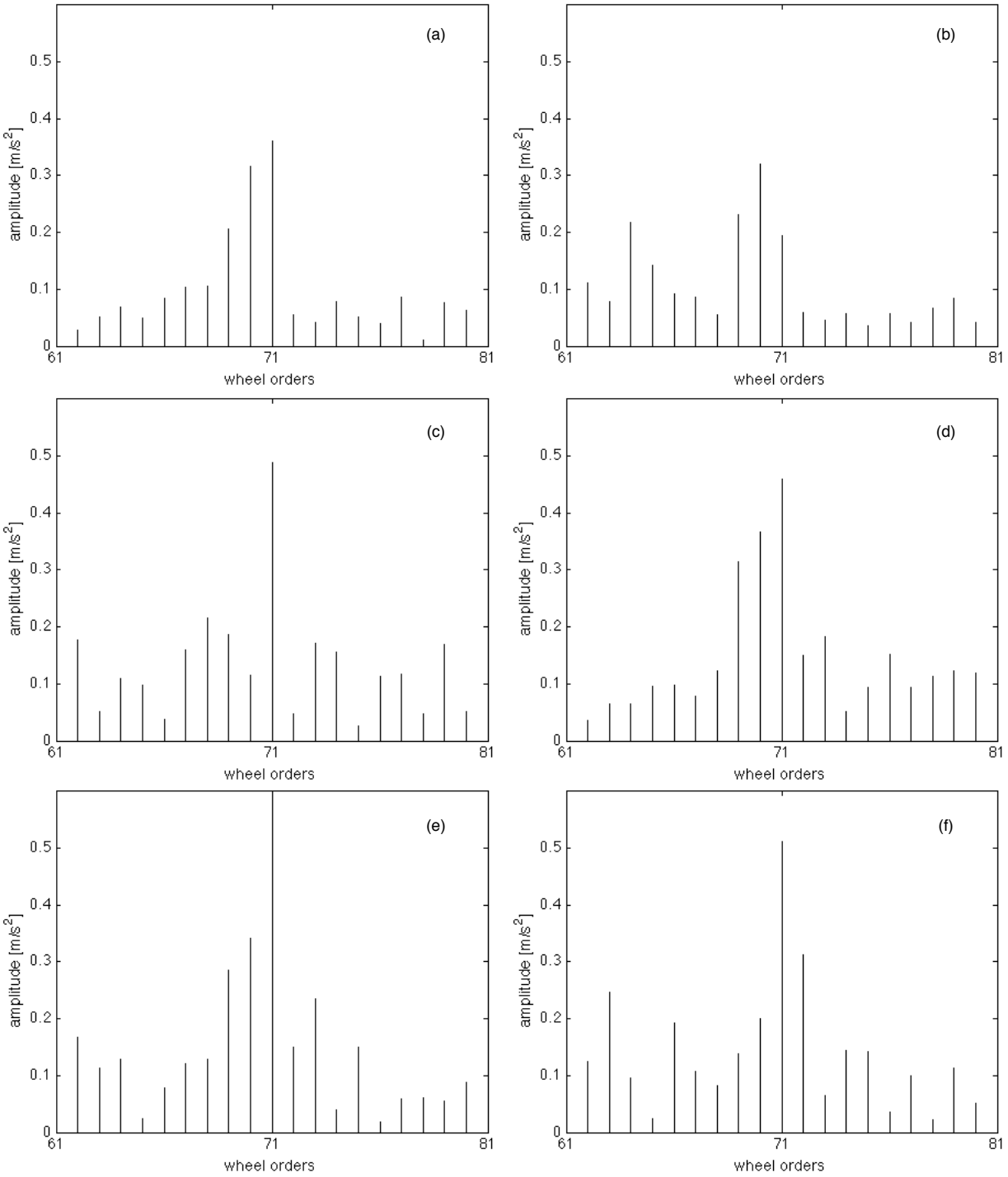

Figure 4.26: FFT of the time-synchronous average of the acceleration signals in the 61-81 wheel order band: (a) sound gear, (b) Smack, (c) Sp12.5%, (d) Sp25%, (e) Sp50%, (f) Sp100%

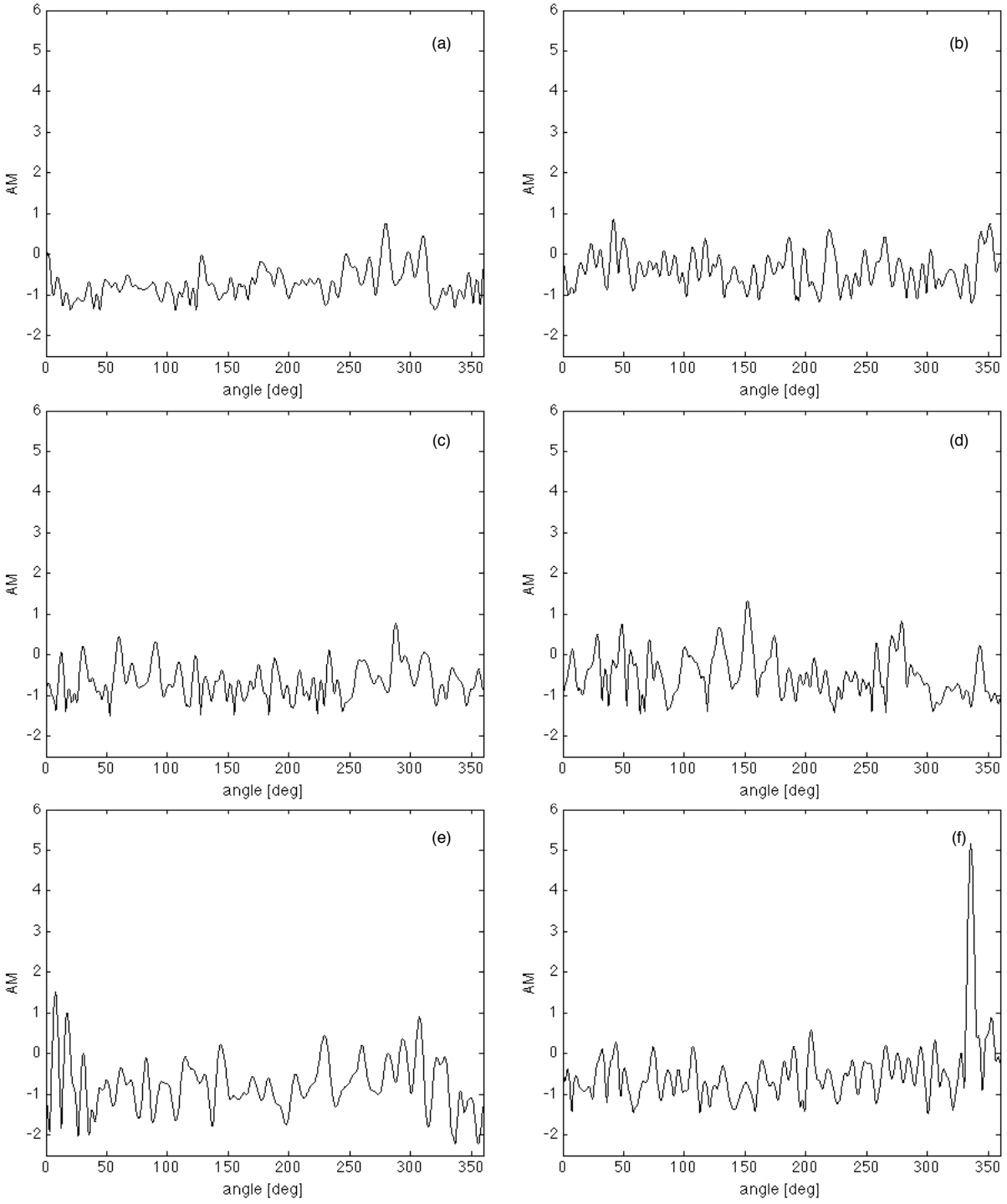

Figure 4.27: Amplitude modulation in the 35-107 order band: (a) sound gear, (b) Smack, (c) Sp12.5%, (d) Sp25%, (e) Sp50%, (f) Sp100%

spall sizes, and its seems to be insensitive to fault presence for the smallest ones, thus the AM technique can not gives any information about fault severities.

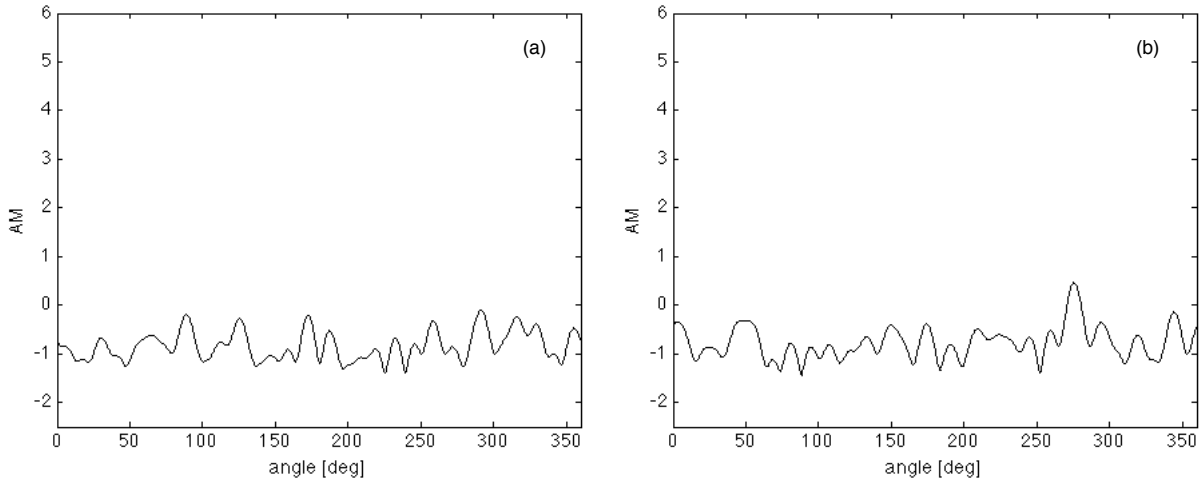

Figure 4.28: Amplitude modulation in the 71-101 wheel order band: (a) Sp12.5%, (b) Sp25%

As done before, the CWT and WVD techniques are now applied to vibration signal, in order to detect the non-stationary signal characteristic produced by the faulted tooth. Both WVD and CWT are evaluated in 50-400 wheel order band, which include the main meshing harmonics as shown before in the FFT plots. Figure 4.29 depicts the WVD for the spall vibration signals. For the sound gear (Figure 4.29 (a)), one can see the meshing frequency and its second and third harmonics at 71^{th}, 142^{th} and 213^{th} order respectively, whilst the other horizontal lines are due to the wide frequency components that are depicted in the FFT spectrum of Figure 4.25 (*a*). In addition, for each couple of spectrum components a cross term arise and so, the distributions is of difficult interpretation. In particular, this behavior can be noted in Figures 4.29 (*b*), (*c*) and (*d*). However, the presence of the faulted tooth can be detected in Figures 4.29 (*e*) and (*f*), which are relative to Sp50% and Sp100% respectively. De facto, the location of the faulted tooth is highlighted by the changes in the WVD around 20 degrees in the 50-100 wheel order band for Sp50%, while for Sp100% around 340 degrees for the same order band. Therefore, the Fourier-Bessel expansion of the synchronous averages are needed in order to obtain a WVD suitable for fault detection.

Figure 4.30 shows the results of the foreign operation. Firstly the distribution becomes of clear interpretation, de facto, the gear meshing frequency remains the strongest (horizontal dark line at 71^{th} order), but it is now possible to distinguish several modulation sidebands around this component. The presence of the sidebands is depicted by the dashed horizontal lines occurring around the 71^{th} order in Figures 4.30 (*b*), (*d*), (*e*) and (*f*). In particular, by analyzing Figure 4.30 (*d*), the location of the faulted tooth can be detected by the amplitude change of the dashed horizontal line around 150 degrees. Unfortunately this is not enough for a sure fault detection, therefore other investigations are needed.

The CWT of the TSA is computed using Impulse mother wavelet and the analysis is carried out in a 50-400 wheel order band such as WVD. The results are plotted in Figure 4.31. As it happens before, the meshing frequency dominate the maps. A localize change in the CWT maps can be seen in the cases of Sp50% and Sp100%, Figures 4.31 (*e*) and (*f*) respectively. These changes confirm the location of the defect as it happens before for WVD. More in details, comparing Figure 4.31 (*d*) whit Figure 4.29 (*d*), it is possible to highlight the presence of the faulted tooth for Sp25%. De facto, the analysis of the single Figure 4.31 (*d*) is not sufficient for a clear fault localization, in fact the change of the CWT map around 150 degrees is not strong enough for a confident fault detection, but from the correlation of this map with it corresponding WVD yields to an higher confidence, and the faulted tooth engagement can be detected.

Finally, the cyclostationary analysis of tooth spalls is performed. As done before, the SCD function is evaluated via Fourier series expansion of the WVD. In order to reduce noisy components in the SCD plot, the signal is synchronously averaged. The time synchronous average is performed over four wheel rotations in order to obtain a cycle frequency resolution of $3,80$ *Hz*. As a first indication of cyclostationary signal content, the DCS function is evaluated and the results are plotted in Figure 4.32, over the 0-100 frequency band. The DCS functions show several non-zero cycle frequencies corresponding to the wheel ration frequency and its harmonics for all spall sizes. As a matter of fact that, this provides a first indication of a modulation effect, which is present in the signals, but this effect can not be related to the faulted tooth take-over.

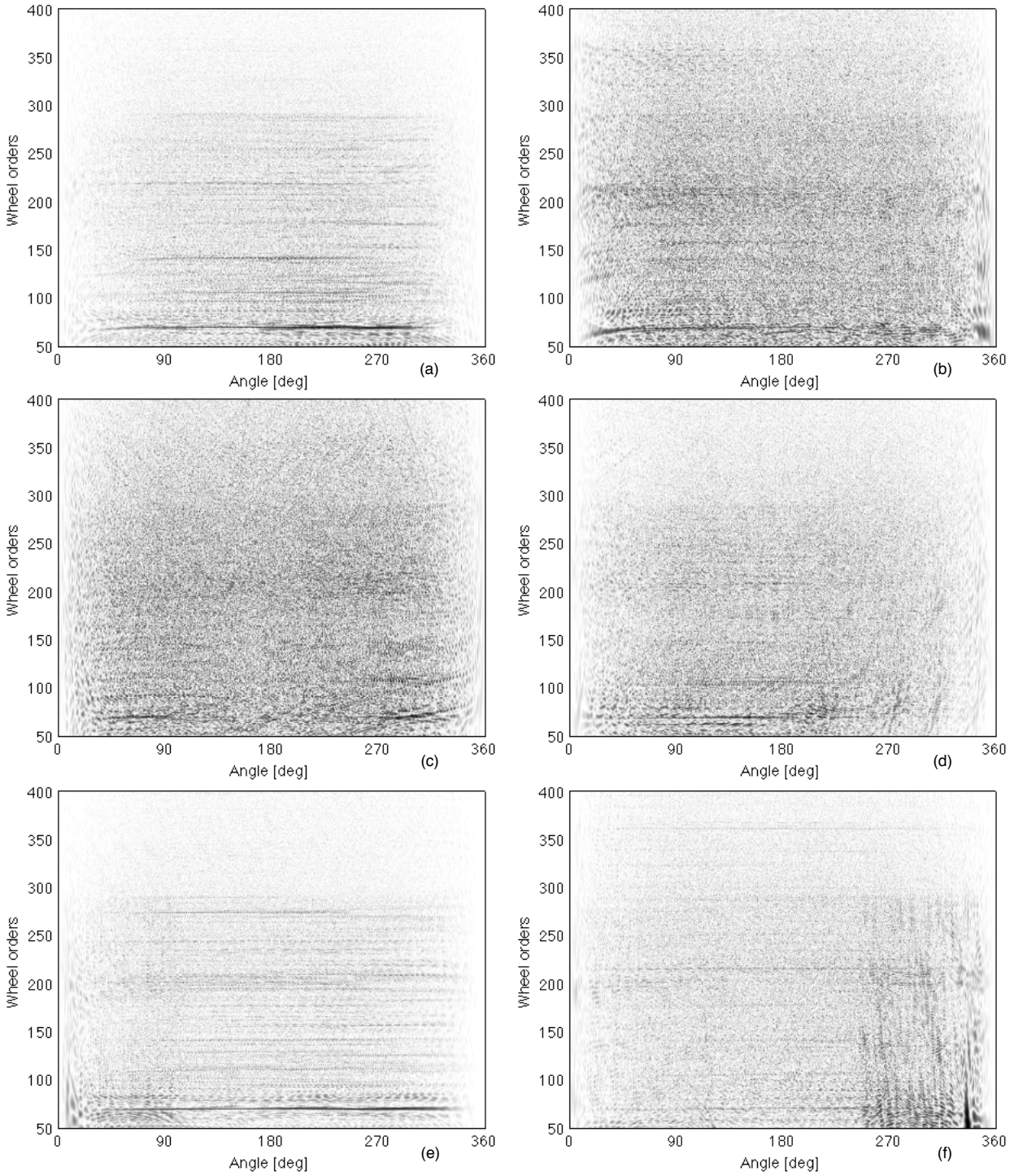

Figure 4.29: WVD of the time-synchronous average of the acceleration signals: (a) sound gear, (b) Smack, (c) Sp12.5%, (d) Sp25%, (e) Sp50%, (f) Sp100%

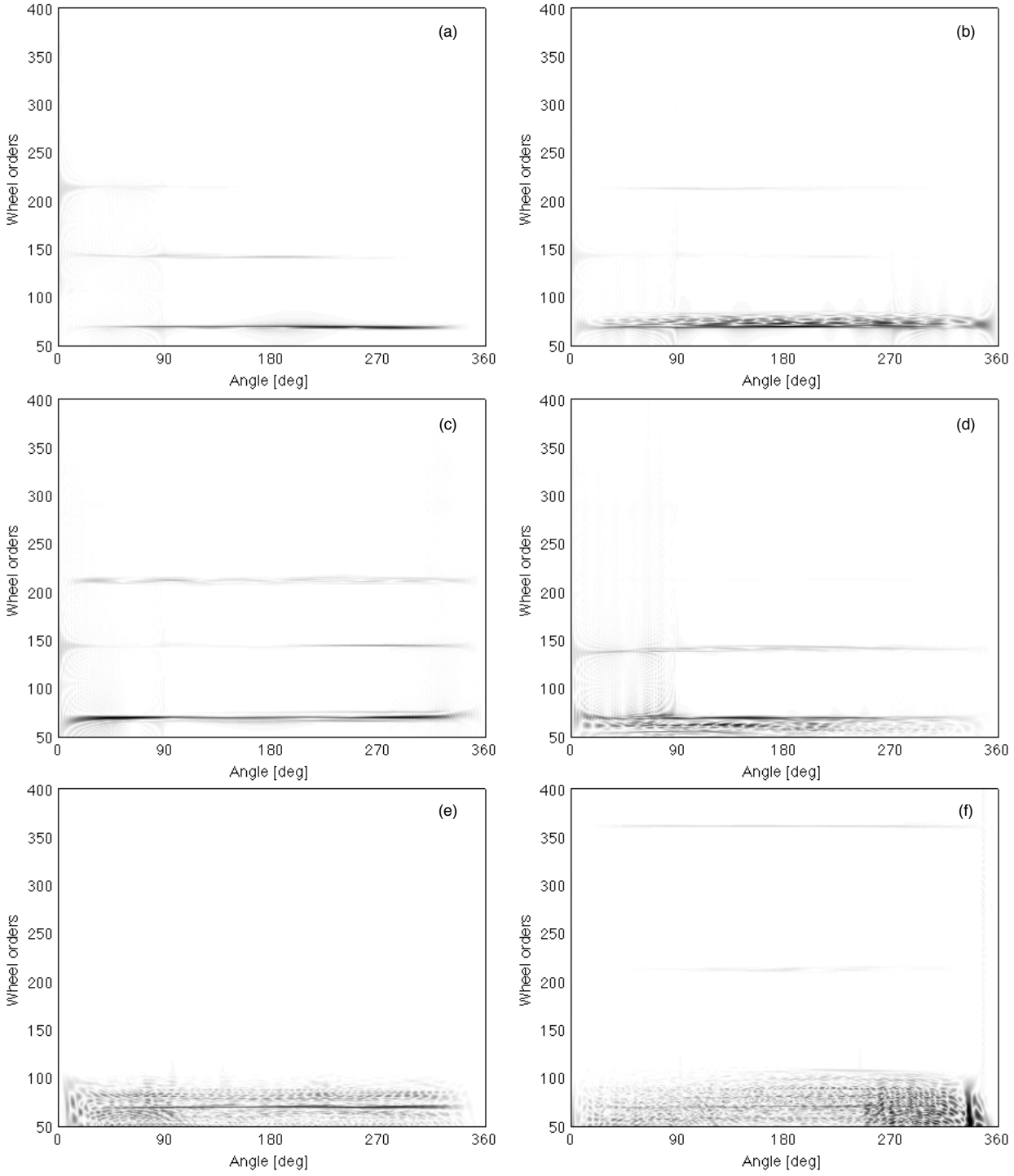

Figure 4.30: WVD of the time-synchronous average of the acceleration signals: (a) sound gear, (b) Smack, (c) Sp12.5%, (d) Sp25%, (e) Sp50%, (f) Sp100%

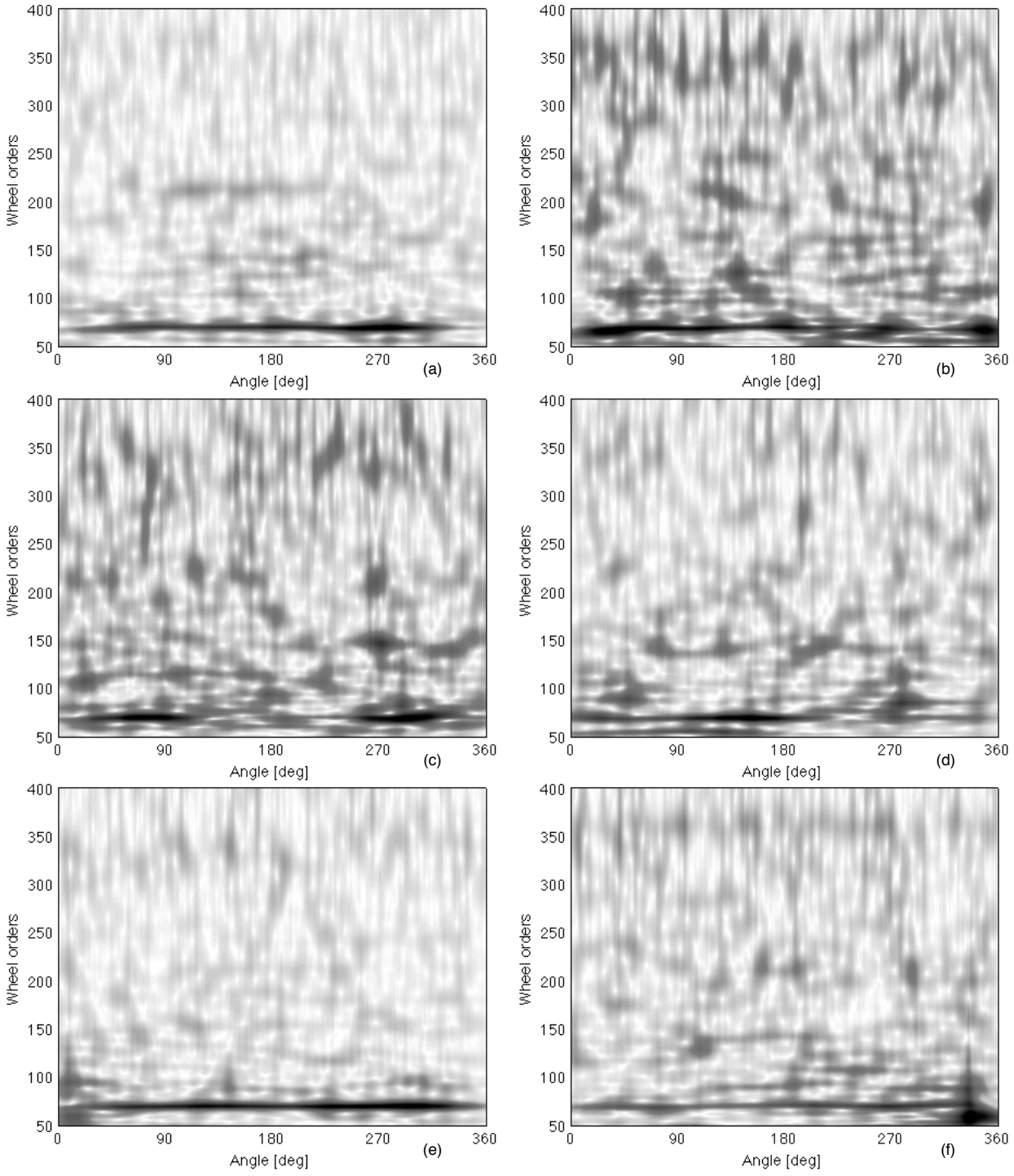

Figure 4.31: CWT of the time-synchronous average of the acceleration signals: (a) sound gear, (b) Smack, (c) Sp12.5%, (d) Sp25%, (e) Sp50%, (f) Sp100%

In fact, as previously explained, modulations are related to both misalignments and fault, therefore the DCS function can be used, in this case, in order to assure the presence of a cyclostationry content. Notwithstanding this information is not a proof of a possible tooth spall.

Figure 4.33 plots the SCD magnitude of the bifrequency plane (f,α), using a three-dimensional diagram, in which only a frequency range around the gear meshing frequency is considered. In depth, because of the first modulating sidebands seems related to the tooth spall, the relationships between the gear meshing frequency (1080 *Hz*) and its first upper modulating sidebands (1095.21 *Hz*), relative to the wheel, is investigated. Therefore the SCD component considered in this analysis is the follows:

$$\left.\begin{array}{ll} \text{gear meshing frequency} & 1080\,Hz \\ \text{first upper modulating sidebands relative to the wheel} & 1095.21\,Hz \end{array}\right\} \Rightarrow (1087.6, 15.21)$$

Data cursors depict the amplitude ant the location in the bifrequency plane of the foreign component. As one can see from Figure 4.33 peak that corresponds to the correlation between the gear meshing frequency and its upper modulating sidebands shows an increment with the spall sizes. In other words, going through the sound gear to the Sp100% the SCD component concerning the faulted tooth rise. This results confirm that the rise of the upper sidebands shown in Figure 4.26 is related to the tooth spall sizes.

In addition the SCD can well describe the physical nature of this type of fault, in fact as depicted in the contour plots of Figure 4.34 the effects of the impulsive components, which arise during the faulted tooth engagement, are described.

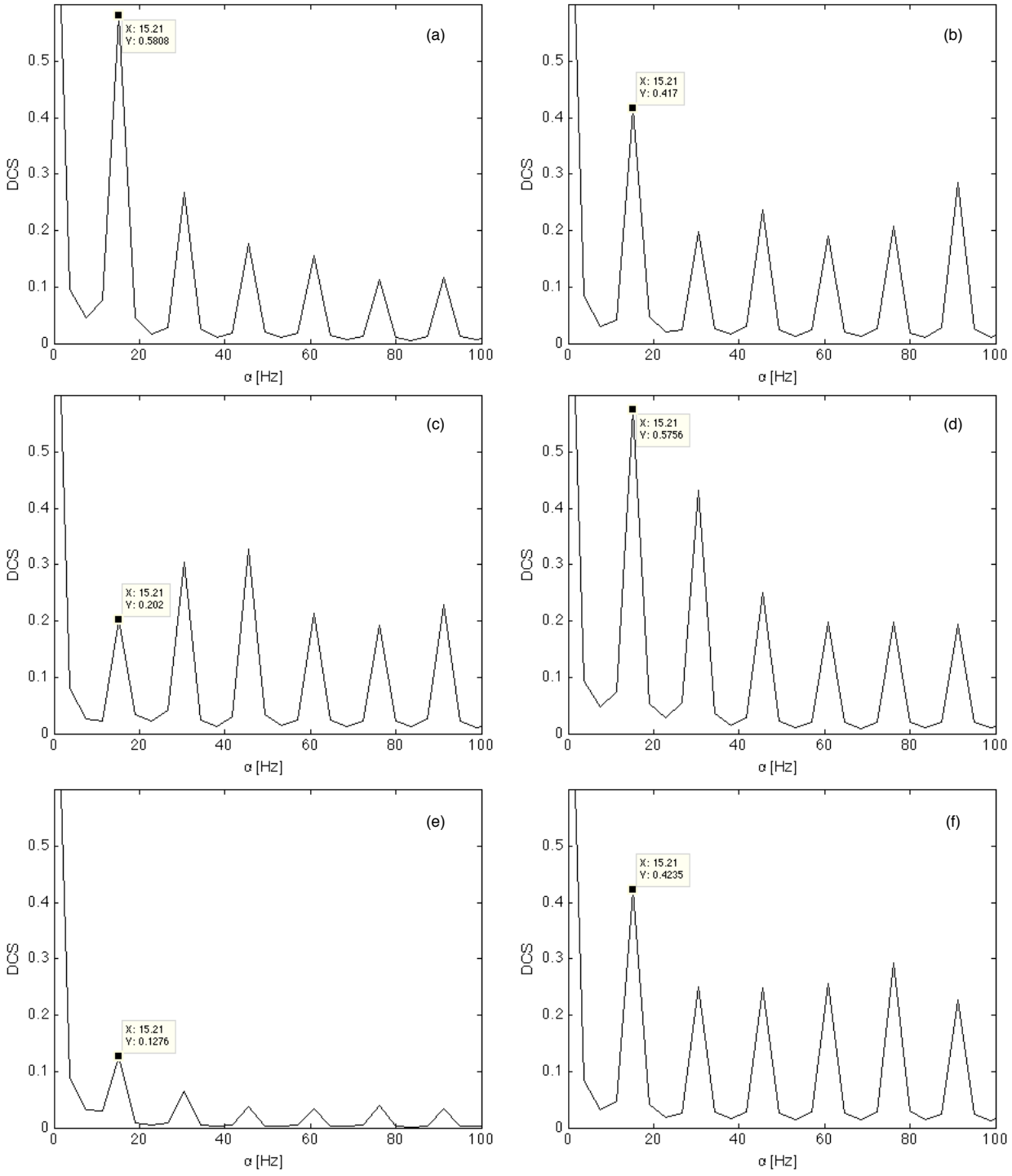

Figure 4.32: Degrees of cyclostationary of the acceleration signals: (a) sound gear, (b) Smack, (c) Sp12.5%, (d) Sp25%, (e) Sp50%, (f) Sp100%

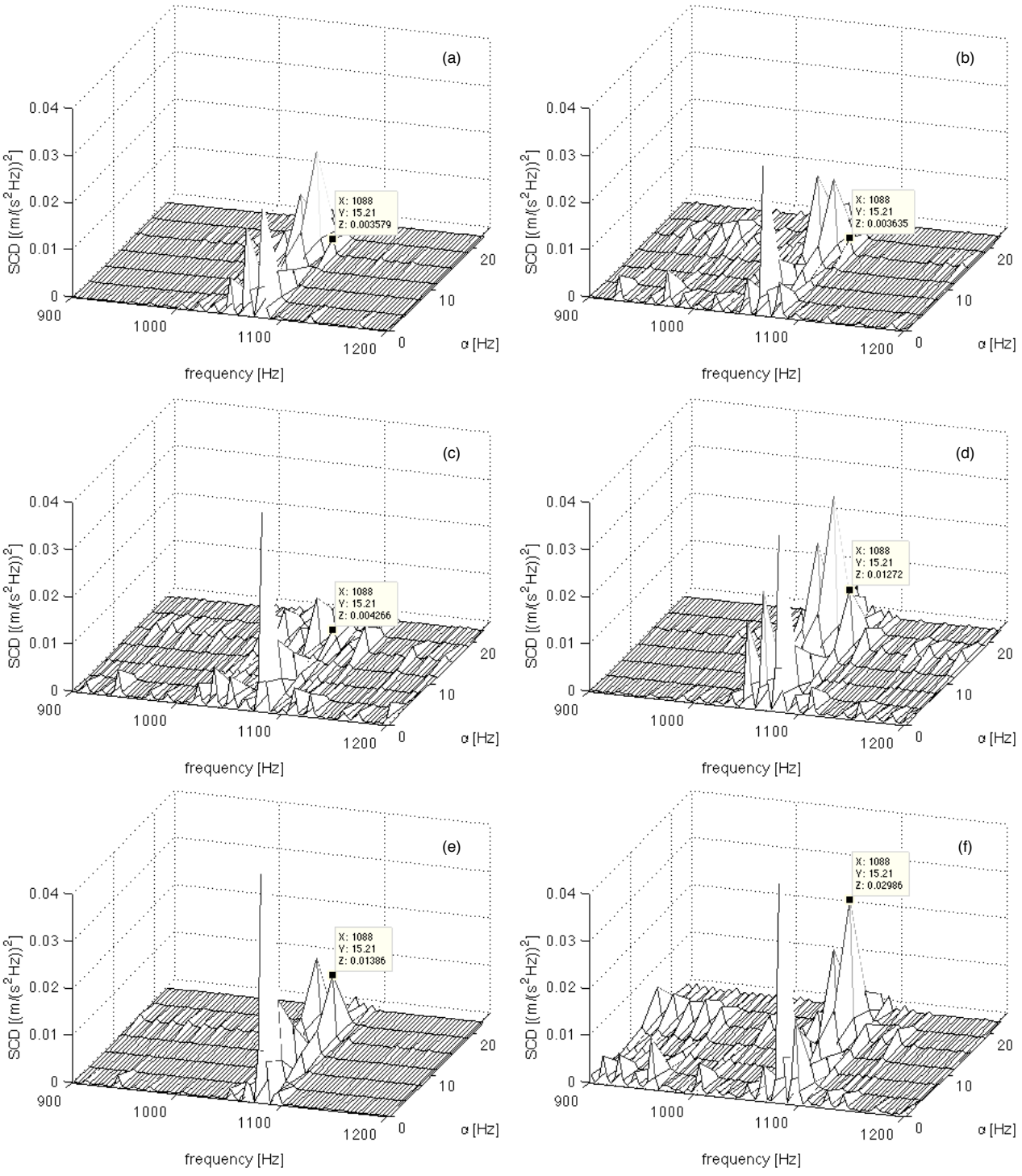

Figure 4.33: WVD of the time-synchronous average of the acceleration signals: (a) sound gear, (b) Smack, (c) Sp12.5%, (d) Sp25%, (e) Sp50%, (f) Sp100%

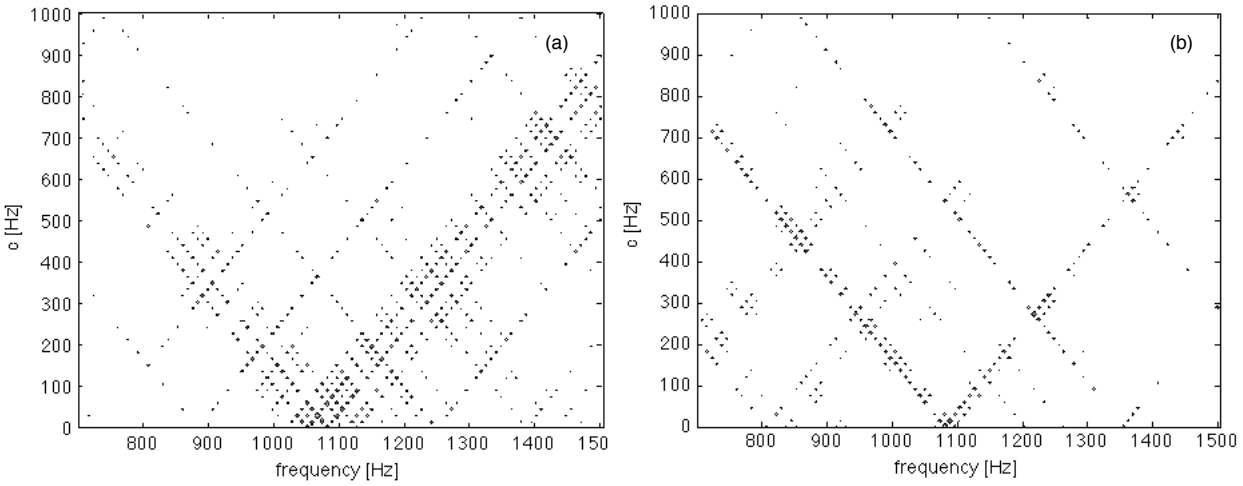

Figure 4.34: Contour plots of the SCD in range concerning the meshing frequency: (a) Sp12.5%, (b) Sp100%

Chapter 5

Conclusions

Tanto ch'i vidi de le cose belle
che porta'l ciel, per un pertugio tondo;
e quindi uscimmo a riveder le stelle.
Dante Alighieri XXXIV Inferno vv.137-139

This thesis addresses the application of several signal processing techniques for the diagnostics of mechanical faults in rotating machines. In particular the sensitivity and effectiveness of non-stationary signal processing techniques are compared.

The numerical implementation of these techniques is investigated. In particular highlighting pro and contra of different spectral correlation algorithms and reviewing the use of the Wigner-Ville distribution of the time synchronous average for the evaluation of the spectral correlation density. As shown in Chapter 2, the combined use of the time synchronous average and WVD for the evaluation of the SCD function gives rise to an efficient algorithm that allows a faster SCD estimation. However, the result are strongly influenced by the number of synchronous averages performed on the time signal. In fact, the component amplitude of the resulting function strongly depends on the average number, therefore the effectiveness of this technique to fault localization can be widely affected.

The advantages and the limitations of a new method that combines the Fourier-Bessel series expansion and the Wigner-Ville distribution are investigated, by means of the results of different mechanical fault analysis. As shown in Chapter 2 this

method gives coarse results, if the vibration signal contains impulsive components with the same carrier frequency. In fact, as shown in Figure 2.10 the single impulse signal component cannot be extracted. Hence cross-terms cannot be removed form the WVD. Notwithstanding, the FB decomposition can be an useful tool in vibration based diagnostics, in fact as shown in Chapter 3, the amplitude and frequency modulations due to the cracked tooth engagement, are well extracted from the vibration signal and, the reconstructed meshing harmonic gives rise to an abrupt fall corresponding to the cracked tooth engagement (Figure 4.14).

Moreover, an experimental characterization of the vibrational behaviour of spalls in gear tooth is presented in this work. In more detail, time and time-frequency analysis of this type of fault is performed showing pro and contra of Wigner-Ville distribution and Continuous Wavelet transform. As depicted in Figures 4.29 and 4.31 these techniques can localize the engagement of the faulted tooth only in the cases of large spall sizes Sp50% and Sp100%. However, no information about the fault severity can be obtained from these techniques. A vibration signal processing technique that overcomes this problem is the SCD function. In fact, cyclostationary analysis of the gear tooth faults highlight the sensitivity and the effectiveness of this technique to fault severity. De facto, as plotted in Figures 4.17, 4.18 and 4.33 the SCD component concerning the link between the meshing frequency and its upper modulating sidebands increase with the fault severity. In particular, the SCD results concerning tooth spalls confirm the results obtained by the FFT analysis of the TSA. In fact, as shown in Figure 4.26, the upper modulating sidebands of the gear meshing frequency can be related to the faulted tooth engagement.

Finally, a mathematical model concerning tooth spalls is produced. The mathematical model is composed by a sum of N harmonics. Local amplitude and phase modulation functions as well as additive impulses are introduced in order to taken into account the main physical phenomena that arise during the engagement of the faulted tooth. By comparing model and experimental results, Figures 4.23 and 4.34, it is possible to explain the vibration effects of different spall sizes.

From the analysis of experimental data, it is found that no one technique alone pro-

vides a reliable diagnosis, but that all the methods could be included in the diagnostic procedure.

Bibliography

[1] P. D. McFadden. Examination of a technique for the early detection of failure in gears by signal processing of the time domain average of the meshing vibration. *Mechanical Systems and Signal Processing*, 1:173–183, 1987.

[2] P. D. McFadden. Detecting fatigue cracks in gears by amplitude and phase demodulation of the meshing vibration. *Journal of Vibration, Acoustics, Stress, and Reliability in Design*, 108:165–170, 1986.

[3] R. B. Randall. *Frequency analysis*. K. Larsen & Søn, 1987.

[4] Z. K. Peng and F. L. Chu. Application of the wavelet transform in machine condition monitoring and fault diagnostics: a review whit bibliography. *Mechanical Systems and Signal Processing*, 18:199–221, 2004.

[5] I. Antoniadis and G. Glossiotis. Cyclostationary analysis of rolling-element bearing vibration signals. *Journal of Sound and Vibration*, 248(5):829–845, 2001.

[6] J. Antoni, J. Daniere, and F. Guillet. Effective vibration analysis of ic engine using cyclostationarity. part i - a methodology for condition monitoring. *Journal of Sound and Vibration*, 257:815–837, 2002.

[7] J. Antoni, F. Bonnardot, A. Raad, and M. El Badaoui. Cyclostationary modelling of rotating machine vibration signals. *Mechanical Systems and Signal Processing*, 18:1285–1314, 2004.

[8] R. B. Randall, J. Antoni, and S. Chobsaard. The relatioship between spectral correlation and envelope analysis in the diagnostics of bearing faults and other cyclostationary machine signals. *Mechanical Systems and Signal Processing*, 15 (5):945–962, 2001.

[9] Z. K. Zhu, Z. H. Feng, and F. R. Kong. Cyclostationarity analysis for gearbox condition monitoring: Approaches and effectiveness. *Mechanical Systems and Signal Processing*, 19:467–482, 2005.

[10] C. Capdessus, M. Sidahmed, and J. L. Lacoume. Cyclostationary processes: Application in gear faults early diagnosis. *Mechanical Systems and Signal Processing*, 14(3):371–385, 2000.

[11] R. B. Pachori and P. Sircar. A new technique to reduce cross terms in the wigner distribution. *Digital Signal Procssing*, 17:466–474, 2007.

[12] Dimitris G. Manolakis, Vinary K. Ingle, and Stephen M. Kogon. *Statistical and Adaptive Signal Processing*. Artech House, 2005.

[13] S. Mallat. *A Wavelet tour of signal processing*. Academic Press, 1999.

[14] O. Rioul and M. Vetterli. Wavelets and signal processing. *IEEE SP Magazine*, pages 14–38, 1991.

[15] T. A. C. M . Claasen and W. F. G. Mecklenbräuker. The wigner distribution - a tool for time-frequency signal analysis. part I: Continuous-time signals. *Philips J. Res.*, 35:217–250, 1980.

[16] T. A. C. M . Claasen and W. F. G. Mecklenbräuker. The wigner distribution - a tool for time-frequency signal analysis. part II: Discrete-time signals. *Philips J. Res.*, 35:276–300, 1980.

[17] T. A. C. M . Claasen and W. F. G. Mecklenbräuker. The wigner distribution - a tool for time-frequency signal analysis. part III: Relations with other time-frequency signal transformations. *Philips J. Res.*, 35:372–389, 1980.

[18] Wolfgang Martin and Patrick Flandrin. Wigner - ville spectral analysis of non-stationary process. *IEEE Transactions on Acoustics, Speech, and Signal Processing*, ASSP-33(6):1461–1470, 1985.

[19] D. Gabor. Theory of communication. *Journal of IEEE*, 93:429–457, 1946.

[20] E. L. Schukin, R. U. Zamaraev, and L. I. Schukin. The optimisation of wavelet transform for the impulse analysis in vibration signals. *Mechanical Systems and Signal Processing*, 18:1315–1333, 2004.

[21] W. J. Wang and P. D. McFadden. Application of wavelets to gearbox vibration signals for fault detection. *Journal of Sound and Vibration*, 192:927–939, 1996.

[22] W. J. Staszewski, K. Worden, and G. R. Tomlinson. Time-frequency analysis in gearbox fault detection using the wigner-ville distribution and pattern recognition. *Mechanical Systems and Signal Processing*, 11(5):673–692, 1997.

[23] P.D. McFadden and W. Wang. Time-frequency domain analysis of vibration signals ofr machinery diagnostics (II) the weighted wigner-ville distribution. Technical Report OUEL 1891/91, University of Oxford, Department of Engineering Science, 1991.

[24] F. Sattar and G. Salomonsson. The use of a filter bank and the wigner–ville distribution for time-frequency representation. *IEEE Transactions on Signal Processing*, 47:1776–1783, 1999.

[25] S. V. Narasimhan and Malini. B. Nayak. Improved wigner-ville distribution performance by signal decomposition and modified group delay. *Signal Processing*, 83:2523–2538, 2003.

[26] H. F. Davis. *Fourier series and ortogonal functions*. Dover, New York, 1963.

[27] G. Arfken. *Mathematical methods for physicists*. Accademic Press, New York and London, 1966.

[28] P. D. McFadden and W. Wang. Time-frequency domain analysis of vibration signals ofr machinery diagnostics (I) introduction to the wigner-ville distribution. Technical Report OUEL 1859/90, University of Oxford, Department of Engineering Science, 1991.

[29] W. A. Gardner. The spectral correlation theory of cyclostationary time-series. *Signal Processing*, 11:13–36, 1986.

[30] W. A. Gardner. Spectral correlation of modulated signals: Part I - analog modulation. *IEEE Transactions on Communications*, COM-35:584–594, June 1987.

[31] W. A. Gardner, W. A. Brown, and C. Chen. Spectral correlation of modulated signals: Part II - digital modulation. *IEEE Transactions on Communications*, COM-35:595–601, June 1987.

[32] W. A. Gardner. Exploitation of spectral redundancy in cyclostationary signals. *IEEE SP Magazine*, pages 14–36, April 1991.

[33] W. A. Gardner. *Cyclostationarity in Communications and Signal Processing*. IEEE Press, 1994.

[34] W. A. Gardner and C. M. Spooner. The cumulant theory of cyclostationary timeseris, part I: Fundation. *IEEE Transactions on Signal Processing*, 42:3387–3408, 1994.

[35] C. M. Spooner and W. A. Gardner. The cumulant theory of cyclostationary timeseris, part II: Development and applications. *IEEE Transactions on Signal Processing*, 42:3409–3429, 1994.

[36] R. S. Roberts, W. A. Brown, and JR. H. H. Loomis. Computationally efficient algorithms for cyclic spectral analysis. *IEEE SP Magazine*, pages 38–49, April 1991.

[37] W. A. Brown and JR. H. H. Loomis. Digital implementations of spectral correlation analyzers. *IEEE Transactions on Signal Processing*, 41:703–720, February 1993.

[38] Dorde Č. Simić and Jasmina R. Simić. The strip sectral correlation algorithm for spectral correlation stimation fo digitally modulated signals. In *TELSINKS*, 13-15 October, Niš, Yugoslavia 1999.

[39] J. Antoni. Cyclic spctral analysis in practic. *Mechanical Systems and Signal Processing*, 21:597–630, 2007.

[40] S. Delvecchio, G. Dalpiaz, O. Niculita, and A. Rivola. Condition monitoring in diesel engines for cold test applications. part i: Vibration analysis for pass/fail decision. In *COMADEM*, 13-14 June, Faro, Portugal 2007.

[41] S. Delvecchio, G. Dalpiaz, O. Niculita, and A. Rivola. Condition monitoring in diesel engines for cold test applications. part ii: Comparison of vibration analysis techniques. In *COMADEM*, 13-14 June, Faro, Portugal 2007.

[42] G. Dalpiaz, A. Rivola, and R. Rubini. Effectiveness and sensitivity of vibration processing techniques for local fault detection in gears. *Mechanical Systems and Signal Processing*, 14(3):387–412, 2000.

[43] G. Dalpiaz. Early detection of fatigue cracks in gears by vibration analysis techniques. *ÖGsterreichische Ingenieur- und Architekten-Zeitschrift (ÖGIAZ)*, 135: 312–317, 1990.

[44] M. J. Brennan, M. H. Chen, and A. G. Reynolds. Use of vibration measurements to detect local tooth defects in gears. *Sound and Vibration*, pages 12–17, November 1997.

[45] J. Ma and C. J. Li. Gear defect detection through model-based widband demodulation of vibrations. *Mechanical Systems and Signal Processing*, 10(5):653–665, 1996.

[46] N. Baydar and A. Ball. Detection of gear failures via vibration and acoustic signals using wavelet transform. *Mechanical Systems and Signal Processing*, 17:787–804, 2003.

[47] P. W. Tse, W. Yang, and H. Y. Tam. Machine fault diagnosis through an effective exact wavelet analysis. *Journal of Sound and Vibration*, 277:1005–1024, 2004.

[48] G. Dalpiaz, G. D'Elia, and S. Delvecchio. Design of a test bench for the vibro-acoustical analysis and diagnostics of rotating machines. In *WCEAM-CM2007*, 11-14 June, Harrogate, United Kingdom 2007.

[49] R. B. Randall. A new method of modeling gear faults. *Journal of Mechanical Design*, 104:259–267, April 1982.

Appendix A

As expalined by Antoni et al. in [6, 7], several statistical tools can be derived form the WVD, and used in diagnosis of IC engine. In this work the mean instantaneous power is taken into account, which can be estimated by the first spectral moment of the autocorrelation function.

As explained in [12] the moments of a random variable are defined as:

$$r_x^{(m)} = \int_{-\infty}^{+\infty} x^m f_x(x) dx \tag{A.1}$$

where $f_x(x)$ is the probability density function of the random variable and r_x^m is the m^{th}-order moment of the considered random variable.

Spectral moments can also be obtained from the moment generating function, which is defined by:

$$\Phi_x(s) = \mathrm{E}\{e^{sx}\} = \int_{-\infty}^{+\infty} f_x(x) e^{sx} dx \tag{A.2}$$

where s is a complex variable and E is the expectation. Equation (A.2) can be interpreted as the Laplace transform of $f_x(x)$ with sign reversal. Expanding e^{sx} of the left-end side of equation (A.2) in a Taylor series at $s = 0$, one obtain:

$$\begin{aligned} \Phi_x(s) = \mathrm{E}\{e^{sx}\} &= \mathrm{E}\Big\{1 + sx + \frac{(sx)^2}{2!} + \cdots + \frac{(sx)^m}{m!} + \cdots \Big\} \\ &= 1 + s\mu_x + \frac{s^2}{2!} r_x^{(2)} + \cdots + \frac{(sx)^m}{m!} r_x^{(m)} + \cdots \end{aligned} \tag{A.3}$$

Therefore the m^{th}-order moment can be obtained by differentiating equation (A.3)

with respect to s:

$$r_x^{(m)} = \frac{d^m(\Phi_x(s))}{(ds)^m}\Big|_{s=0} \tag{A.4}$$

The mean instantaneous power was introduced by Antoni at al. in [6], by pointing out the similarities between the WV spectrum (WVS) and the probability density function. Where the Wigner-Ville spectrum is the expected value of the Wigner-Ville distribution. In order to link the WVS to a probability density function, distribution values must be positive. Hence the analytical signal is used during distribution evaluation. Therefore, by viewing the WVS as a probability density function of the frequency variable f conditioned to the angular variable θ, from equation (A.4) the m^{th}-order spectral moment can be defined by using the autocovariance function for moment generating function [6]:

$$r_x^{(m)}(\theta) = (2\pi j)^{-m}\frac{\partial^m \mathrm{R}_{xx}}{(\partial\tau)^m}(\theta, 0) \tag{A.5}$$

where the first moment $r_x^0$is the mean instantaneous power.